DEVELOPMENT OF HIGH RATE PERFORMANCE PHOSPHATE CATHODE MATERIALS FOR LITHIUM-ION BATTERIES

XIAO PENGFEI

(B.Sc.)

A THESIS SUBMITTED

FOR THE DEGREE OF DOCTOR OF PHILOSOPHY

DEPARTMENT OF MECHANICAL ENGINEERING

NATIONAL UNIVERSTIY OF SINGAPORE

2012

Acknowledgements

First, I would like to express my deepest gratitude to my supervisors, Prof. Lu Li and A/Prof. Lai Man On, for their invaluable perspectives, suggestions and careful revisions for this dissertation, and for their generous support, continuous guidance and encouragement through the four years.

I would like to thank my senior Dr. Wang Hailong, who introduced me to this graduate program, guided me into the research filed of lithium-ion batteries and offered precious suggestions to this study. I would like to thank Dr. Wang Shijie, Dr. Xia Hui, Dr. Xiao Wei, Dr. Yan Feng and Dr. Zhang Zhen, who taught me a lot in study, experiment, research and life. I would like to thank Mr. Ye Shukai, Ms. Zhu Jing and Mr. Song Bohang for their support and friendship during the four years' study. I would like to specially thank Dr. Zhang Jixuan, Mr. Ding Bo, Mr. Lin Chunfu and Mr. Sun Linfeng for their kind help in certain experiments in this study.

I would like to acknowledge the following laboratory staffs and technicians: Dr. Maung Aye Thein, Mr. Thomas Tan, Mr. Ng Hongwei, Mr. Khalim and Mr. Juraimi, for providing technical support and an organized laboratory environment.

Finally, I would like to thank my parents, my wife Zhou Xuan and all my family members. I cannot get through and finish this study without their understanding and unconditional support.

Summary

This study mainly focuses on phosphate cathode materials for high power lithium-ion batteries (LIBs), especially for large-scale applications such as electric vehicles (EVs). Phosphate materials of olivine ($LiFePO_4$) and of tavorite ($LiVPO_4F$) crystal structures were selected because of their unique lattice stability and safety features. Olivine $LiFePO_4$ (3.4 V vs. Li^+/Li) has already been regarded as the most promising candidate for EVs. However, these phosphate materials lack high power capabilities due to intrinsically low electronic and ionic conductivities. To overcome the problems of poor electronic and ionic transport, electronic structure and fabrication methodology were tailored with cation doping/substitution, conductive carbon coating and nanostructuring. Furthermore, to develop the next generation high voltage LIBs with higher power output, nanostructured 4 V $LiFe_xMn_{1-x}PO_4$ and $LiVPO_4F$ composites were also developed using similar technologies. Crystal structure, chemical composition, micro-morphology, electrical and electronic conductivities of these synthesized materials were carefully characterized and analyzed. Electrochemical properties, including specific capacity, charge/discharge rate capability, cyclic performance and Li^+ chemical diffusion coefficients, were studied to evaluate the battery performances. The materials developed in this study exhibited amazingly high power performance, fast charge capability and excellent long-term cyclic stability, and thus are very promising for the next generation high power LIBs.

Table of Contents

List of Figures

List of Tables

1 Introduction and Literature Review

Global warming, environmental pollution and energy crisis evoke the use of renewable energies such as wind, solar, tide and nuclear. To wean modern society from dependence of fossil fuels, energy conversion and storage devices of high power and energy density are strongly desired. Rechargeable lithium ion batteries (LIBs) are regarded as the most advanced energy storage devices so far because of their higher operation voltage, higher energy density, lower self-discharge and no memory effects when compared to other battery systems. LIBs were first commercialized in early 1990s [1], and have been ubiquitously used in portable electronic devices such as notebook PCs, mobile phones, tablets and digital cameras. However, it is a big challenge to satisfy the power and energy needs of the emerging market of electric tools, bicycles, motorcycles and cars. Herein, this research work aims to develop and engineer phosphate cathode materials with high performance adequate for the next generation of large-scale applications such as hybrid/electric vehicles (HEVs/EVs). Structural, electrical and electrochemical properties of these phosphate cathode materials will be studied in detail.

This chapter firstly introduces basic concepts of LIBs and then describes the research background of electrode materials. Then, common electrode materials will be reviewed and compared for the purpose of large-scale applications. Finally, the research routes and strategies of this dissertation will be provided.

1.1 Lithium-ion battery

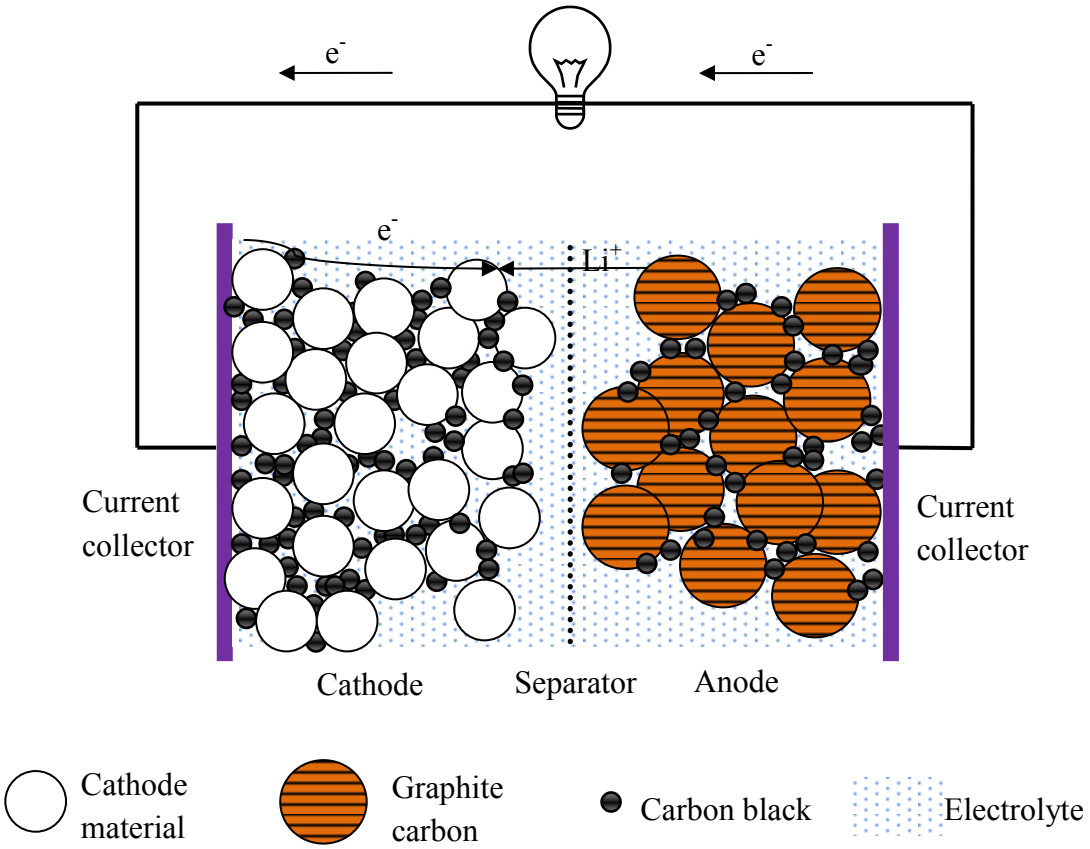

Fig. 1.1 A schematic of rechargeable lithium-ion battery

A cell or battery is an electrochemical device that converts chemical energy into electrical energy and vice versa. A battery comprises of at least an anode, a cathode, electrolyte and sometimes a separator. Fig. 1.1 shows a schematic of a typical $Li_{1-x}CoO_2/Li_xC_6$ full-cell, the most widely used LIB system in portable electronic devices nowadays. In a lithium-ion battery, the cathode is the positive electrode and the source of Li^+ ions, while the anode is the negative electrode and the sink of Li^+ ions. The electrolyte is an electronically insulating organic solution of lithium salts, for example $LiPF_6$. The electrolyte provides Li^+ ionic transport between cathode and anode, but

blocks internal electronic transport. The separator, normally a porous membrane made of polymer or glass fiber, allows circulation of electrolyte but prevents direct electronic contact between cathode and anode.

In a lithium-ion battery, electrochemical reactions take place at both electrodes accompanied with Li^+ insertion and extraction of the lattices of the active materials. In the case of $Li_{1-x}CoO_2/Li_xC_6$ full-cell, the electrode reactions during charge and discharge can be expressed as:

Charge: Anode: $C_6 + xLi^+ + xe^- \rightarrow Li_xC_6$ Cathode: $LiCoO_2 \rightarrow xLi^+ + xe^- + Li_{1-x}CoO_2$

Discharge: Anode: $Li_xC_6 \rightarrow C_6 + xLi^+ + xe^-$ Cathode: $xLi^+ + xe^- + Li_{1-x}CoO_2 \rightarrow LiCoO_2$

During the charge process, Li^+ ions are extracted from the $Li_{1-x}CoO_2$ lattice with oxidation of cobalt from Co^{3+} to higher valance state of Co^{4+}. The Li^+ ions diffuse through the electrolyte to the anode and are then stored in the aromatic hexagonal rings of graphite. Electrical energy therefore is converted to chemical energy and is stored in the crystal lattices. During the discharge process, driven by the potential difference between the delithiated $Li_{1-x}CoO_2$ and lithiated Li_xC_6, electrons flow from anode to cathode through external circuit. Co^{4+} is reduced to a lower electronic state of Co^{3+}, while Li^+ ions are inserted into the $Li_{1-x}CoO_2$ lattice. The stored chemical energy is converted into electrical energy in the external circuit. Generally, the overall voltage of a lithium-ion battery is determined by the difference between the chemical potentials of the electrode reactions [2], while the capacity equals the total charges of Li^+ ions that reversibly waggle between the cathode and the anode. As electrochemical reactions

involve both electrons and Li^+ ions, electronic and Li^+ ionic transports in the electrode and in the lattices of electrode materials are crucial to the electrochemical properties of LIBs.

1.2 Challenges of large-scale applications

As stated above, the performances of a lithium-ion battery rely greatly on the Li^+ extraction/insertion properties of the electrode materials. Indeed, the evolution of LIBs is also a history of exploration and development of electrode materials. Various materials have been proposed as electrode materials for LIBs for four decades. However, the conventional $Li_{1-x}CoO_2/Li_xC_6$ system cannot meet the requirements of EV/HEVs and other large-scale applications due to poor safety features, limited availability and intrinsic toxicity of cobalt.

The principal challenges facing LIBs for large-scale applications are safety, cost, operation voltage, capacity, rate of charge-discharge and durability. Firstly and most importantly, LIB cells should have strict safety features. The battery pack for large-scale applications may be comprised of thousands of single cells, resulting severe challenges of heat dissipation and current/voltage disorder. Furthermore, the battery pack may encounter high-speed impact and penetration in occasions like car accidents, which may leads to disastrous consequences. Therefore, electrode materials should have strong lattice stability and low electrode-electrolyte reactivity at elevated temperature (for example at 60 ºC), in overcharged state and under mechanical impact.

Secondly, electrode materials should be capable of fast extraction and insertion of Li^+ ions so that the LIB cell can deliver sufficient power and can be charged rapidly. Thirdly, electrode materials should sustain long-term cycling with repeated drastic volume change during fast extraction/insertion of Li^+ ions. Finally, the cost of the electrode materials is preferably as low as possible, due to the huge quantity of electrode materials used in large-scale applications. To paint a complete picture of the research background of this work, common electrode materials will be reviewed in detail in the following sections.

1.3 Oxide cathode materials

1.3.1 From sulfides to oxides

Prior to the era of lithium-ion battery, early lithium metal batteries did not receive wide commercial attention as they do today, whereas the lead acid, Ni-Cd and Ni-MH batteries dominated the market of rechargeable batteries. Primary lithium metal batteries of Li/CF_x and Li/MO_2 systems were initially introduced back in 1960s. Rechargeable lithium metal batteries of Li/TaS_2 and Li/TiS_2 systems were first proposed in 1970s, and were then intensively studied. *Exxon* first marketed rechargeable lithium metal battery of Li/TiS_2 system in 1977 but failed to win the market. Since these cathode materials of sulfides and carbon fluorides initially carry no Li^+, expensive and highly flammable metallic lithium or its alloys have to be the counter electrode to provide Li^+. The sulfide cathode materials are also difficult to fabricate. The operation

voltage of the Li/TiS_2 battery is only ~1.9 V, relatively low from today's point of view.

To overcome these drawbacks of sulfides, it is not surprising that researchers naturally veered to the oxides with similar crystal structure, since O^{2-} and S^{2-} have similar chemical bonding properties. V_2O_5 and MoO_3 with layered structure received particular attention at that time [3]. The researches of layered oxides in 1980s led to the remarkable invention of $LiCoO_2$ that actually has isomorph structure of $LiTiS_2$ (lithiated TiS_2). In 1991, Sony for the first time combined $LiCoO_2$ and graphite, and successfully commercialized rechargeable lithium-ion battery. From then on, lithium-ion batteries began to gain great attention not only from scientists but also from industries and consumers. Nowadays, lithium-ion battery has already dominated the market of rechargeable battery for portable electronic devices.

Various oxide materials have been proposed as cathode materials in the last two decades of the 20^{th} century. The most important oxide cathode materials with α-$NaFeO_2$ layered structure and spinel structure will be reviewed in the following Sections 1.3.2 and 1.3.3, respectively.

1.3.2 Cathode materials with layered structure

Cathode materials with α-$NaFeO_2$ layered structure normally have the chemical formula of $LiMO_2$, where M can be Co, Ni, Mn or their solid solution mixture. Among them, $LiCoO_2$ with a high potential > 3.9 V vs. Li^+/Li and a practical capacity of ~130 mAh g^{-1} is now dominating the current LIB market of portable devices because of its superb electrochemical activity. In 1980, Goodenough et al. [4] first recognized that

Li_xCoO_2 ($0< x< 1$) with a similar layered structure of Li_xTiS_2 could reversibly extract and accommodate Li^+. Fig. 1.2 shows a schematic of the typical crystal structure of $LiMO_2$ (M = Co). Oxygen ions are nearly cubic close-packed with both Li^+ and Co^{3+} occupying the octahedral sites in the alternate layers along (001). The oxygen, Co^{3+} and Li^+ layers are stacked in a repeating configuration of Li-O-M-O-Li. This layered crystal structure provides two-dimensional pathways for Li^+ diffusion. Hence, the chemical diffusion coefficient of Li^+ in $LiCoO_2$ is relatively high up to $\sim 10^{-9}$ cm^2 s^{-1} [5, 6]. In the CoO_6 layers, each CoO_6 octahedron is surrounded by six CoO_6 octahedrons through edge sharing with each other. Hopping conduction between transitional metal Co atoms is considerably facile with a relatively high intrinsic electronic conductivity of 10^{-3} S cm^{-1}. Furthermore, $LiCoO_2$ turns into a metallic conductor with conductivity up to 10^{-1} S cm^{-1} after extraction of small amount of Li^+ [7]. Hence, $LiCoO_2$ in micrometer size has desirable electrochemical properties because of its high electronic and ionic conductivities.

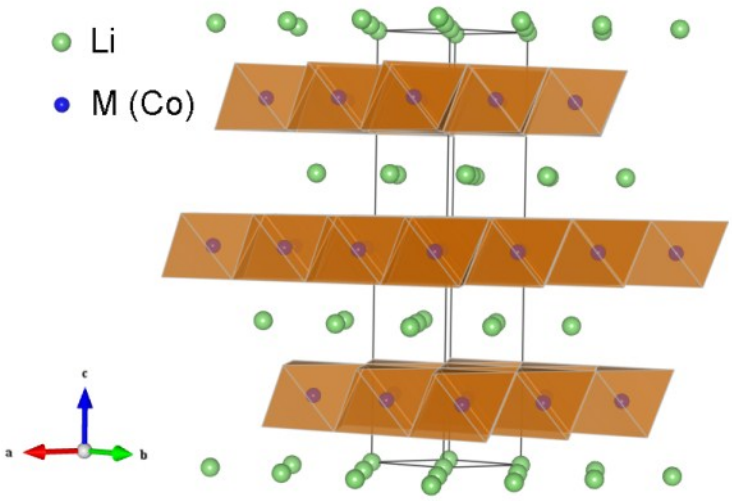

Fig. 1.2 Crystal structure of layered $LiMO_2$ (M= Co, Ni, Mn etc.)

Nevertheless, $LiCoO_2$ is not applicable in large-scale applications due to some intrinsic drawbacks. Firstly, $LiCoO_2$ has a relatively low practical capacity and poor overcharge stability. If all the Li^+ ions are removed from the lattice, $LiCoO_2$ will have a high theoretical capacity up to 274 mAh g^{-1}. However, the theoretical capacity is normally limited to only 130 mAh g^{-1} with only $x \sim 0.5$ Li^+ in Li_xCoO_2 reversibly extracted [2]. Further extraction of Li^+ results in phase transition into unstable structured lithium poor CoO_2, leading to release of oxygen and collapse of lattice structure [8]. Secondly, the charged state $Li_{\sim 0.5}CoO_2$ is not thermal stable with electrolyte at elevated temperature (60 °C). The high reactivity between the further delithiated Co^{4+} and HF in the common $LiPF_6$ electrolyte leads to rapid capacity decay and disastrous safety consequences. Finally, cobalt is highly toxic and very expensive due to limited availability. Therefore, $LiCoO_2$ is not an environmental and economical choice for large-scale applications.

$LiNiO_2$ and $LiMnO_2$ are two isomorphs of $LiCoO_2$. They are more

environmentally friendly and economical, since nickel and manganese are less toxic, more abundant and cheaper than cobalt. However, the charged phases of these two materials are highly unstable, resulting in poor cycle performance. Furthermore, $LiNiO_2$ and $LiMnO_2$ have even worse thermal stability when compared to $LiCoO_2$ [9]. The Li^+-Ni^{2+} displacement and Jahn-Teller distortion of Mn^{3+} are the main causes for the poor lattice stability and poor rate capability of these two materials and their derives such as $LiNi_{1/2}Mn_{1/2}O_2$.

On the other hand, $LiNi_{1/3}Co_{1/3}Mn_{1/3}O_2$ is indeed a promising alternative to $LiCoO_2$ with only one third of the cobalt usage [10]. In the lattice of $LiNi_{1/3}Co_{1/3}Mn_{1/3}O_2$, the transitional metal ions Ni, Co and Mn are in the valence state of +2, +3 and +4 respectively, occupying the octahedral sites randomly. Co^{3+} strongly reduces the cation mixing level, leading to much improved specific capacity and rate capability compared to $LiMO_2$ (M= Ni and/or Mn). $LiNi_{1/3}Co_{1/3}Mn_{1/3}O_2$ can provide a high capacity of 200 mAh g^{-1} when cycled between 2.5 V and 4.6 V [10]. $LiNi_{1/3}Co_{1/3}Mn_{1/3}O_2$ may gradually replace $LiCoO_2$ in small cells for electronic devices because of its relatively low cost and the fabrication similarity with $LiCoO_2$. Nevertheless, the high capacity of $LiNi_{1/3}Co_{1/3}Mn_{1/3}O_2$ is achieved though high potential charge at the expense of safety. Similar to the other layered cathode material, the oxygen loss and subsequent lattice collapse in overcharged state and elevated temperature are still vital problems to durability and safety of the cells in practice.

1.3.3 Cathode materials with spinel structure

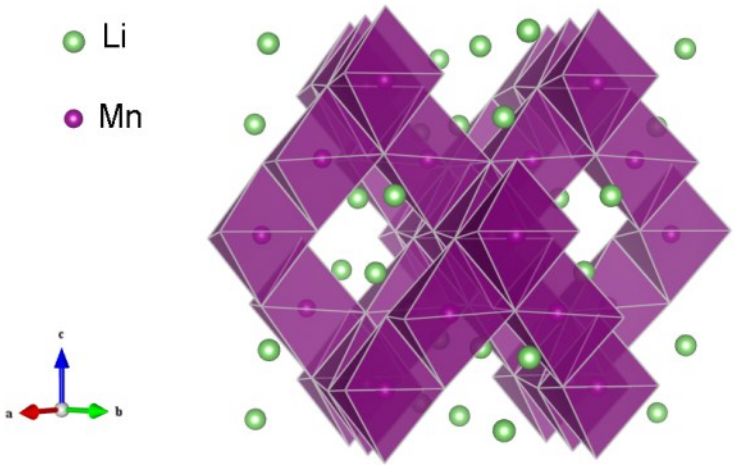

Fig. 1.3 Crystal structure of spinel $LiMn_2O_4$

Spinel compounds such as $LiMn_2O_4$ are promising alternative to $LiCoO_2$ because of low toxicity, low cost and abundant availability. Li^+ insertion and extraction of $LiMn_2O_4$ were first reported by Thackeray et al. in 1983 and 1984 [11, 12]. $LiMn_2O_4$ has an operating potential of 3.9-4.1 V vs. Li^+/Li with a theoretical capacity of 148 mAh g^{-1}. Fig. 1.3 shows a schematic crystal structure of $LiMn_2O_4$. In the cubic close-packed arrangement, oxygen anions occupy 1/8 of the tetrahedral sites, Li^+ ions occupy half of the tetrahedral sites and Mn^{3+} and Mn^{4+} ions occupy the octahedral sites. MnO_6 octahedrons form a 3-d framework through which Li^+ can migrate in 3d tunnels. Because of this 3d migration mechanism, Li^+ diffusion is relatively facile in $LiMn_2O_4$ with a high diffusion coefficients of ~10^{-9} cm^2 s^{-1} [13].

However, the practical capacity (only 120 mAh g^{-1}) and the rate capability of $LiMn_2O_4$ are both poor, due to its low electronic conductivity (10^{-5} S cm^{-1} [14]) when

compared to $LiCoO_2$ (10^{-3} S cm^{-1}). Furthermore, $LiMn_2O_4$ shows very poor storage and cyclic stability, especially at elevated temperature. For example, irreversible capacity loss of $LiMn_2O_4$ is up to 35% after 4 weeks of storage at 55 ºC [15]. One cause for this problem is the strong Jahn-Teller lattice distortion induced by Mn^{3+}. As a result, $LiMn_2O_4$ tends to transform into disordered tetragonal structure in the discharged state [16]. Another cause is the electrolyte degradation on the surface of $LiMn_2O_4$ producing radical and acidic HF in high charged state [17]. Consequently, Mn^{3+} slowly dissolves into the electrolyte, while the highly radical HF corrodes the electrode and other components in the battery.

To overcome the poor lattice stability of $LiMn_2O_4$, two different strategies have been developed: (a) foreign cation doping and (b) surface modification. The principle of foreign cation doping is to reduce Mn^{3+} concentration in the initial electrode and thus lessen the influences of Jahn-Teller distortion. Direct substitution of Mn^{3+} can be achieved using trivalent metal ions such as Al^{3+}, Cr^{3+}, Ga^{3+} and Fe^{3+} [18-23]. Defected $LiM_{\delta/2}Mn_{2-\delta}O_4$ structure has also been developed with divalent Mg^{2+} and Zn^{2+} doping by Thackeray et al. [16]. The cation doping indeed significantly improved the lattice stability and cycleability of $LiMn_2O_4$, however, the practical capacity was reduced and dissolution of Mn^{3+} at elevated temperature remained unsolved.

The cation-doping attempts induced the discovery of a category of “5 V” spinel cathode materials of $LiM_xMn_{2-x}O_4$ ($0< x< 1$) with M = Ni, Co, Fe, Cr and Cu [24-29]. These materials are very attractive in high power LIBs for their high operation voltage at

~5 V, synthesis easiness and low cost. Unfortunately, their high voltage plateaus exceed the safe operation window (1-4.5 V) of current organic electrolytes [30]. The high potential aggravates the electrolyte degradation, resulting in poor cycleability and safety concerns [2, 31]. The feasibility of these high potential spinel materials greatly relies on breakthroughs in the organic electrolyte system in the future.

The strategy of surface modification is to coat the particle surfaces with inert materials to prevent HF etching. Oxide materials, such as MgO, Al_2O_3, ZnO, and ZrO_2, have been successfully coated on spinel $LiMn_2O_4$ particles [32-35]. $LiMn_2O_4$ with these surface coatings exhibit significantly improved cyclic performance even at elevated temperature of ~55 ºC. Nevertheless, the insulating coatings hinder the interparticle electronic transport, resulting in poor rate capability. Moreover, the wet-chemistry routes through which the surface modifications were realized are still too difficult to scale up into industrial productions.

1.4 $LiMPO_4$ with olivine structure

One vital drawback of oxide cathode materials is the instability of the oxygen close-packed structure and the possible oxygen loss when overcharged or overheated. On the other hand, phosphates have incredibly high lattice stability and safety features owing to the strong covalent bond of P-O. In 1980s~1990s, a series of compounds with framework formed by polyanions $(XO_4)^{y-}$ (X ~ S, P, As, Mo, W) were explored by the research group of Goodenough [36-42]. The strong covalent bonds of P-O or S-O

constraint the oxygen atoms and minimize the defects of oxygen site, leading to stable frameworks. Furthermore, the presence of the polyanion $(XO_4)^{y-}$ with strong X-O covalent bond stabilizes the anti-bonding transitional metal redox couple through an M-O-X inductive effect to generate a relatively high potential. In 1997, Padhi and Goodenough et al. first reported $LiMPO_4$ (M =Fe, Mn, Co, and Ni) compounds with olivine structure as cathode materials [43]. Olivine structured phosphates have received great attention as safe cathode materials for large-scale applications owing to their incredibly high lattice stability.

1.4.1 $LiFePO_4$

Fig. 1.4 shows the crystal structure of olivine type $LiMPO_4$ (M= Fe, Mn, Co and Ni). As can be seen, the corner sharing FeO_6 octahedrons form layers that are further cross linked by PO_4 tetragons. PO_4 tetragons and FeO_6 octahedrons form a 3d framework that undergoes small volume change of 6.8% after removal of Li^+ [43]. The M_2PO_4 olivine structure has metal atoms in half of the octahedral sites and P atoms in one-eighth of the tetrahedral sites of the hexagonal close-packed (HCP) oxygen array. M1 octahedral site is occupied by Li^+, while M2 octahedral site is occupied by transitional metal ions M^{2+} (M= Fe, Mn, Co and Ni).

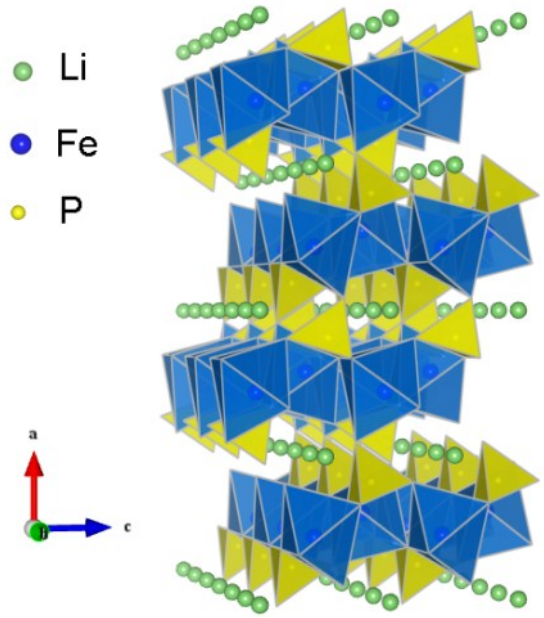

Fig. 1.4 Crystal structure of olivine $LiFePO_4$

$LiFePO_4$ initially carries one Li^+ ion per formula unit that can be reversibly extracted. The theoretical capacity based on this one-electron reaction is ~170 mAh g^{-1} with a potential of ~3.45 V vs. Li^+/Li [43, 44]. $LiFePO_4$ has been regarded as the most promising cathode material for large-scale LIBs in EVs/HEVs particularly, owing to its relatively large specific capacity, extremely high stability and safety features, excellent cyclic performance, non-toxicity, low cost and abundant availability.

Although the phosphate framework structure of $LiFePO_4$ leads to favorable lattice stability, it also results in inferior electronic and ionic conductivities when compared to oxide materials. In the lattice of $LiFePO_4$, each FeO_6 octahedron has four nearest neighbors being linked through cornering sharing oxygen atoms, in contrast to the edge-sharing feature in layered $LiCoO_2$ and spinel $LiMn_2O_4$. As a result, the electron hopping conduction of Fe-O-Fe has a longer distance and is therefore relatively weaker

than that in oxide cathode materials. In addition, transitional metal FeO_6 layers are separated by the inductive covalent-bonded PO_4 layers, resulting in poor interlayer electron hopping. Affected by these factors, the electronic conductivity of $LiFePO_4$ is only ~10^{-9} S cm^{-1} [45, 46], far lower than that of $LiCoO_2$ (~10^{-3}-10^{-1} S cm^{-1}) and $LiMn_2O_4$ (~10^{-5}-10^{-4} S cm^{-1}). $LiFePO_4$ also has a very poor ionic transport with a diffusion coefficient of only 10^{-17}-10^{-14} s cm^{-1} [47], in comparison with $LiCoO_2$ (~10^{-9} S cm^{-1}) and $LiMn_2O_4$ (~10^{-8} s cm^{-1}). This is because Li^+ ions can only migrate in one-dimensional tunnels along [010] direction in olivine lattice, compared to the 2d diffusion in layered $LiCoO_2$ and 3d diffusion in spinel $LiMn_2O_4$.

1.4.2 $LiMnPO_4$

The redox potentials of Ni^{2+}/Ni^{3+} (5.1 V vs. Li^+/Li) in olivine lattice exceed the anodic limit (≤ 5 V) of current organic electrolyte system. Although the redox of Co^{2+}/Co^{3+} (4.9 V vs. Li^+/Li) in olivine $LiCoPO_4$ seems to be more feasible, severe electrolyte degradation is still unavoidable. The practical applications of these "5V" cathode materials strongly rely on breakthrough of electrolyte system with better anodic stability.

On the other hand, olivine $LiMnPO_4$ does have a pleasing high potential of ~ 4.1 V; however, lithium extraction from $LiMnPO_4$ lattice has been proved to be extremely difficult due to poor electronic/ionic conductivities and anisotropic Jahn-Teller lattice distortion induced by Mn^{3+} [43, 45, 48, 49]. Although some notable achievements on $LiMnPO_4$ have been made recently through critical nanosizing and intensive carbon

coating [50-58], the rate capability and cycleability still cannot meet the requirements of practical application at this moment. A viable solution is to fabricate solid solution $LiMn_{1-x}Fe_xPO_4$ ($0 \leq x \leq 1$), in which super-interaction of Mn^{2+}-O-Fe^{2+} leads to improved structural, electrical and electrochemical properties [43, 49]. Recently, Aburch et al. successfully improved the electrochemical performances by M2 site substitution of Fe^{2+} and extensive carbon coating [59]. The specific capacity of the carbon coated $LiMn_{0.8}Fe_{0.2}PO_4$ can reach 160 mAh g^{-1}. Nevertheless, the rate capability of the $LiMn_xFe_{1-x}PO_4$ ($0 \leq x \leq 1$) material is still not desirable at this moment. The solid-solution $LiMn_xFe_{1-x}PO_4$ ($0 \leq x \leq 1$) attracts increasing attention for the higher potential and the higher energy/power density when compared to $LiFePO_4$. $LiMn_{1-x}Fe_xPO_4$ with various compositions of x = 0.15 [60, 61], 0.2 [59], 0.25 [62], 0.4 [48, 63], and 0.5 [64-67] etc. have been developed for optimized electrochemical performances. High quality carbon coating and effective nanosizing are requisites to thorough extraction of Li^+ from Mn based olivine cathode material due to the poor electronic and ionic conductivity and strong reactivity of Mn^{3+} with electrolyte.

1.4.3 Modification strategies

As stated in Section 1.4.1 and 1.4.2, the low electronic and ionic conductivities are the main obstacles to achieve high rate performance of olivine cathode materials. Supervalent cation doping and conductive coating have been proven as effective methods to overcome the poor electronic conductivity. On the other hand, ionic transport can be improved by particle size reduction. Nanosizing can shorten diffusion

pathway, enlarge reaction area and improve electrolyte infiltration. These strategies are often combined with each other to obtain optimal electrochemical properties in practical applications.

1.4.3.1 Cation doping

Cation substitution on both Li site (M1) and transitional metal site (M2) have been studied with various metal ions. Chiang and co-workers first found that trace-level doping with supervalent ions, for example Nb^{5+}, on M1(Li) site of $LiFePO_4$ could significantly increase the electronic conductivity by up to eight orders [46]. As shown in Fig. 1.5, the electrochemical performances of $LiFePO_4$ have been largely improved by only 0.2 mol% Nb^{5+} doping on M1 site. Supervalent cations doping on M1 site has been done via several synthesis routs, such as solid-state reaction, microwave heating, mechanical alloying, sol-gel and hydrothermal reaction. Supervalent cations sucn as Mg^{2+}, Al^{3+}, Y^{3+}, Ti^{4+}, Zr^{4+}, Cr^{3+}, Nb^{5+} and W^{6+} etc. have been used to dope on M1 site to improve the electronic conductivity [68-70]. Rietveld refinements with high quality X-ray diffraction (XRD) and neutron ray diffraction (NRD) from different research groups have proved the solubility of trace amount supervalent cations in olivine lattice [71, 72]. These rigorous refinement results also suggest that supervalent cations should most likely occupy M1 site substitution with M1-site vacancies generated for electro-neutrality [71, 73]. In general, supervalent cations trace doping on M1 site indeed leads to significantly improved electronic conductivity and electrochemical performance.

The cause for the elevated electronic conductivity and enhanced electrochemical performances is still in debates. Chiang suggested that the trace doping create more holes and raise the p-type conduction. On the other hand, some researchers argued that the olivine lattice were not able to accommodate foreign cations and that conductive metallic species such as Fe_2P and $NbOPO_4$ were probably formed on the particle surfaces or grain boundaries, which accounts for the elevated electronic conductivity [69].

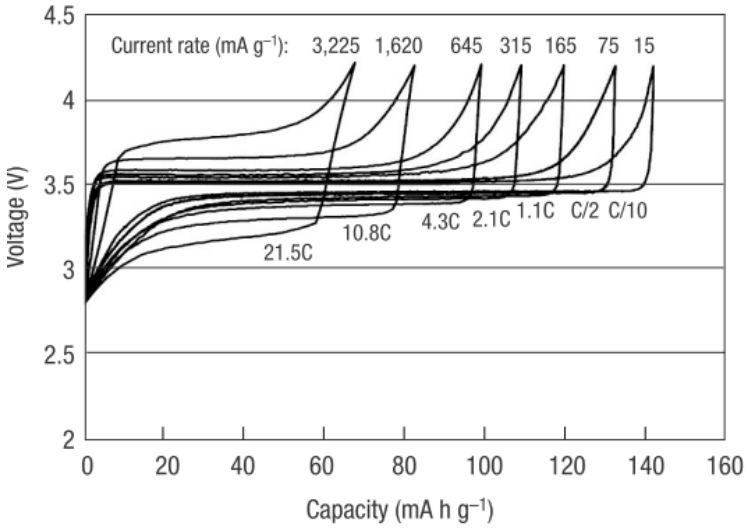

Fig. 1.5 Enhanced rate performance of 0.2 mol% Nb^{5+} doped $LiFePO_4$[46]

It has been found that Nb^{5+} trace doping on M1 site of $LiFePO_4$ can re-orientate the intrinsic Li^+-Fe^{2+} anti-site defects in olivine lattice [74]. The originally homogeneously distributed Fe^{2+} defects on the Li^+ diffusion pathway in olivine lattice was reduced after trace Nb^{5+} doping, leading to improved Li^+ diffusion kinetics. Single crystal of silicon and aluminum doped $LiFePO_4$ were successfully synthesized by Maier et al. [75, 76]. The conductivity results based on single crystal specimens indicate that the electronic and ionic conductivities can be raised in single crystal level after

cation doping, although the enhancement is not as high as those of the works from Chiang [46]. Moreover, the defected lattice after supervalent doping can also leads to an "extended lithium solid solubility" in the lithium rich $LiFePO_4$ and lithium poor $FePO_4$ phases, which can potentially reduce the interphase strain-stress during Li^+ extraction and insertion [71, 77].

Researches of cations doping on M2 (Fe) site of $LiFePO_4$ mainly focus on direct substitution with divalent metal ions including Cu^{2+} [78], Mg^{2+} [79, 80] and Zn^{2+} [81] etc.. M2 site substitution seems to have very little effects on electronic conductivity. Although these works showed certain improvements of electrochemical properties over the pristine $LiFePO_4$, they were usually accompanied with other modifications such as carbon coating to enhance electronic transport.

1.4.3.2 Conductive additives

The feasible conductive additives include amorphous carbon [82-85], carbon nanotubes [86], silver [87-89], copper [90], conductive polymer [91, 92] and so on. The ideal coating should not only deliver electrons to all the particle surfaces, but also facilitate electrolyte infiltration. Although metals such as silver and copper have very high electronic conductivities, the poor electrolyte infiltration and considerably high cost hinder their practical applications. Conductive networks such as carbon nanotubes [86], graphene sheets [62, 93, 94] and conductive polymers [91, 92, 95] may have promising future only after the processing difficulties in large quantity production are solved.

On the other hand, amorphous carbon coating is a simple, facile, economical and effective strategy to improve the electronic transport and electrochemical properties of phosphate materials. It has been widely adopted in the research of electrode materials and industrial production. The carbon-coating strategy for phosphates materials though pyrolysis of organic compounds was initially proposed by Huang and Nazer et al. [82]. In general, there are three important benefits of carbon coating : (1) to serve as a reductive agent to prevent Fe^{3+} oxidation; (2) to hinder particle growth; and (3) to enhance the electronic conductivity over the particles. Carbon coating can be conducted through many synthesis routes with various carbon sources such as carbon black, sucrose, glucose, citric acid, pitch, polymer and various organic compounds. The morphology and the performance of the final products largely depend on the processing and carbon sources.

1.4.4 Synthesis routes

Nanosized particles are necessary for phosphate materials due to their sluggish electronic and ionic transport properties in bulk phase. Nano-sized phosphate materials have been developed and engineered through various synthesis methods. In addition, particle size, micromorphology, impurity, defects and crystallinity of the electrode materials also play important roles in the electrochemical performances. The following sections will review the main synthesis routs that have been proposed and optimized for phosphate cathode materials.

1.4.4.1 Solid -State Reaction

Solid-state reaction, as the name suggests, is a chemical reaction in the absence of solvent. The raw materials are mechanically mixed or milled homogenously, while the mixture is calcinated at high temperature to promote atom diffusion and reaction in solid phases. Solid-state reaction has the advantages of synthesis ease, economics (no solvent needed) and high reaction rate (high reactant concentration without solvent). As a conventional method for producing materials and ceramics with a long history, solid-state reaction is the most widely used synthesis route in the commercial production of electrode materials. Leading industrial companies such as A123, Valence and Sony are all using solid-state reaction to produce powders of $LiCoO_2$, $LiMn_2O_4$ and $LiFePO_4$ [96].

In a typical solid-state synthesis route of $LiFePO_4$, stoichiometric amount of iron salt (usually ferrous oxalate), a lithium compound (usually lithium carbonate or lithium hydroxide), and ammonium phosphate as the phosphorous source, are firstly milled into a homogeneous mixture. The mixture is then decomposed at a temperature of 300–400 $^{\circ}C$ in inert atmosphere to expel the gases. Finally, the mixture is sintered at temperatures ranging from 400 to 800 $^{\circ}C$ for 5-24 h in inert atmosphere, sometimes with reductive hydrogen to reduce Fe^{3+} if applicable. The purity, composition and morphology of the final material depend largely on the processing parameters such as the homogenization parameters and calcinations temperature. Although an inert or even reductive atmosphere is employed, the presence of the residual Fe^{3+} phase is still possible and

often reported, since Fe^{2+} is very sensitive to oxygen. Fe^{3+} might be formed by a small amount of oxygen included in the inert gas and/or residual air trapped in the small pores of the particles. When the sintering temperature is higher than 800 °C, some impurities such as Fe_2O_3, $Li_3Fe_2(PO4)_3$, Fe_2P, Li_3PO_4 etc. may be formed [97-99]. Carbon or carbon-containing organics, for example sucrose and citric acid can be added into the mixture as carbon sources in order to enhance the electronic conductivity of the final products.

Carbon thermal reduction is a type of solid-state reaction that uses Fe^{3+} reactants instead of Fe^{2+} as iron source. Naturally abundant Fe^{3+} compounds such as Fe_2O_3 are much cheaper than the Fe^{2+} reactant such as ferrous oxalate. Carbon sources are added in the mixture as reductive agent to reduce Fe^{3+} to Fe^{2+} at high temperature. Single-phase $LiFePO_4$ can be obtained by thermal treatment above 800 °C. Since the calcination temperature is much higher than that in traditional solid-state reaction, the particle size is relatively large, and Fe^{3+} impurities are possibly residual. Thus, electrochemical performances of $LiFePO_4$ synthesized via carbon thermal reduction are normally not ideal [96, 100, 101]. Nevertheless, carbon thermal reduction is of particular significance in industrial production for its low cost.

Mechanical activation/alloying are variants of solid-state reaction for production of very fine powders. Mechanochemical alloying/activation take place in high-energy milling with continuous rigid impact and friction. The raw material powders undergo repeated welding and fracturing in a dry high-energy ball-milling vessel during

mechanochemical alloying/activation. The process is able to produce powder with very fine particles in less time when compared to the traditional solid-state reaction [96, 102-105]. However, the impurities contaminated from the ball milling media and oxidation of Fe^{2+} during high-energy ball milling are still problems to be solved, particularly in large scale productions.

1.4.4.2 Wet-chemistry routes

Wet-chemistry routes such as hydrothermal reaction, sol-gel and co-precipitation, refer to chemical reactions in liquid solutions. Wet-chemistry routes offer the feasibility of molecular level mixing and reaction, nanosizing, nano- and micro-structure control, and in-situ conductive coating. The drawbacks of the wet chemistry routes may include low crystallinity, impurity phase, oxidation of Fe^{2+} in aqueous solution and relatively higher cost when compared to conventional solid-state reaction.

Sol-gel method is probably the most widely used wet-chemistry route for $LiFePO_4$. The motivation for sol-gel processing of $LiFePO_4$ primarily lies in the fact that it ensures a potentially higher purity and homogeneity than mechanical mixing process. Sol-gel processing enables the control of the structure of a $LiFePO_4$ on a nanometer scale from the earliest stages of processing [83, 96, 106, 107]. In a typical sol-gel synthesis of $LiFePO_4$, stoichiometric Fe^{2+}, PO_4^{3-} and Li^+ are mixed in aqueous solution with chelating agents added to form a homogenous sol. Citric acid or other chelating agents continue to form a 3d gel framework as shown in Fig. 1.6 [108]. The gel was then dried and then calcinated to obtain crystalized $LiFePO_4$. Chelating agents and

other soluble organic compounds such as sucrose, glucose and ascorbic acid act as the *in-situ* carbon sources for the final $LiFePO_4$ nanoparticles. As a result of the molecular level mixing, nanoparticles of $LiFePO_4$ synthesized via sol-gel are fine, uniform and disperse.

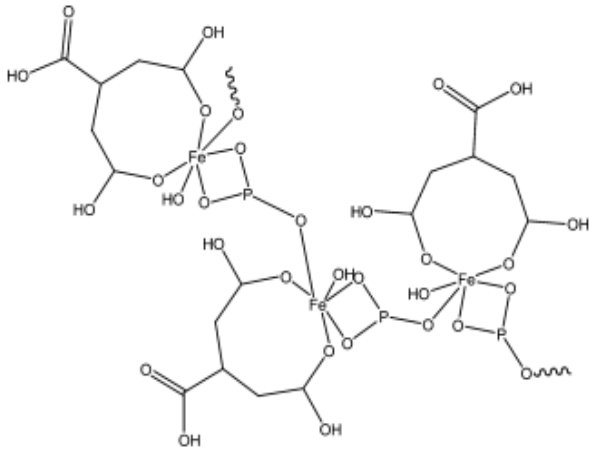

Fig. 1.6 Typical gel structure for developed using sol-gel with citric acid [108].

Hydrothermal synthesis is a quick, facile, energy-saving and economical method to prepare nanostructured materials. It has been proven as a very successful and efficient method for many oxide materials and in many research fields including LIBs, super-capacitors, photovoltaics and sensors. $LiFePO_4$ with preferred crystal shape and surfaces can be tailored using the hydrothermal synthesis [109, 110]. Nevertheless, the hydrothermally synthesized $LiFePO_4$ has relative inferior electrochemical properties due to severe Li-Fe anti-site defects [96, 111-113]. It was found that more than 7% of the Fe^{2+} ions occupy the M1 site in the hydrothermally synthesized $LiFePO_4$ [111], which blocks the one-dimensional migration pathway of Li^+ ions. Additionally, tavorite $LiFePO_4(OH)$ impurities have often been found along with hydrothermally

synthesized $LiFePO_4$ due to the oxidizing circumstances in aqueous solution [109]. Hence, hydrothermal reaction is not a favorable approach for electrochemically active olivine materials.

Co-precipitation is also a solution-based method that offers the advantages in uniform particle size. Pure and homogeneous $LiFePO_4$ can be synthesized by aqueous co-precipitation and subsequent heat treatment in inert atmosphere [96, 114-116]. Heating the solution containing Li^+, Fe^{2+}, and PO_4^{3-} ions with the pH value adjusted between 6 and 10 facilitates the formation of $LiFePO_4$ rather than the formation of Li_3PO_4 and $Fe_3(PO_4)_2$. The main drawback of this method is low production rate and possible impurities of $LiFePO_4(OH)$, $Fe_3(PO_4)_2$ and Li_3PO_4.

1.4.4.3 Other synthesis routes

Various synthesis routes have been developed to synthesize phosphate materials, such as emulsion-drying, spray pyrolysis, freeze-drying method, KCl molten salt method, polyol method, rheological phase reaction, electric discharge assisted mechanical milling etc [117]. However, most of these unusual methods require either special complex processing or expensive equipment, leading to high cost of final products.

1.5 $LiMPO_4F$ with tavorite structure

Olivine $LiFePO_4$ has been regarded as one of the most promising cathode material in LIBs for EVs/HEVs. However, its low potential (3.4 V vs. vs. Li^+/Li) is an intrinsic

drawback for high power and energy applications. Recently, many efforts have been devoted to exploration and development of high potential or high capacity phosphates and fluorophosphates materials such as $LiMn_xFe_{1-x}PO_4$, $LiFePO_4F$ and $LiFeSO_4F$ [56, 118-120]. Tavorite $LiVPO_4F$, first proposed by Barker et al. in a pioneering work [121], is a 4.2 V (vs. Li^+/Li) fluorophosphate cathode material with a theoretical capacity of 155 mAh g^{-1}, as shown in [121]. It is much more electrochemically active than its direct competitor $LiMnPO_4$ (4.1 V), from which through extraction of lithium is still very difficult [43, 45]. Although $LiFePO_4$ has superior advantages as cathode material in large-scale power source, especially in electric vehicles, its low potential (3.45 V vs. Li^+/Li) is not satisfactory. The intrinsic low potential limits the energy and power density of the material.

Unlike other high potential materials, $LiVPO_4F$ has good stability with electrolyte and decent long cyclic performance. Differential scanning calorimetry (DSC) test showed that $LiVPO_4F$ in charged state is thermally stable up to 175 ºC with very small heat flow [122]. Zhou et al. further confirmed the thermal stability of charged state $LiVPO_4F$ electrode with electrolyte was as good as $LiFePO_4$, the most stable cathode material known so far [123]. Good cyclic performances have been demonstrated both in half-cells and full-cells coupled with commercial graphite anode [124, 125].

The sensitive and volatile fluoride is the main obstacle in synthesis of electrochemically active $LiVPO_4F$. Most previous reports on $LiVPO_4F$ used solid-state reaction with carbon thermal reduction to reduce V^{5+} to V^{3+}. Other than carbon thermal

reduction, Barker et al. applied an ion exchanging method to achieve $LiVPO_4F$ from isomorph $NaVPO_4F$ [126], while Li et al. developed a sol-gel method to obtain nanocrystalline $LiVPO_4F$ [127]. The $LiVPO_4F$ in the previous reports has often been found with impurities of either LiF or $Li_3V_2(PO_4)_3$ [123, 124, 127], which limits the electrochemical properties. Normally the realizable specific capacity of $LiVPO_4F$ is limited to about 130 mAh g^{-1}, much lower than the theoretical capacity of 155 mAh g^{-1}.

1.6 Anode materials

Graphite and its derivatives have dominated as the anode material in commercial LIBs for over two decades. It has a high theoretical capacity of ~370 mAh g^{-1}, good electronic conductivity and low operation potential at 0.2 V (vs. Li^+/Li). Until now, graphite is still the first choice for small cells in portable devices and other applications that can endure long charge duration. However, graphite falls short on fast charge capability and safety features required by EVs/HEVs. Metallic lithium easily deposits on graphite surface at elevated temperature (60 ºC) and/or upon fast charge [128]. The metallic lithium dendritic crystals can penetrate the separator, causing internal short circuit between cathode and anode. The high flammability of lithiated graphite further intensifies safety concerns especially when it is used in large-scale LIBs.

Alternatives to graphite such as $Li_xTi_yO_z$, Sn, Si, TiO_2 and other metal oxides have intensively been studied in recent years. Among them, Sn, Si and other conversion type

metal oxides (i.e. SnO_2) have demonstrated much larger capacities than graphite. However, they are not practically suitable for commercial LIBs, especially for large-scale applications, due to their low coulombic efficiency, relatively poor fast charge performances and severe safety concerns. Sn and Si undergo >300% volume changes [129, 130] upon first lithiation, resulting in serious safety risk in close-packed commercial LIBs.

Among various candidates for anode materials, titanium based materials, especially TiO_2 and $Li_4Ti_5O_{12}$, have received particular attention because of their crucial advantages in safety features and fast charge capability. Li^+ insertion potential for Ti^{3+}/Ti^{4+} redox is normally ~1.5-2 V, lying inside the organic electrolyte window (1-4.5 V)[30]. Titanium based materials also undergo much smaller volume changes upon lithiation (e.g. 4% for anatase TiO_2) when compare to graphite (10%), Sn and Si (> 300%), leading to better electrode stability [129, 130]. TiO_2 and $Li_4Ti_5O_{12}$ may the most promising anode material for safe and fast charge large-scale LIBs. The main drawback of $Li_xTi_yO_z$ materials is the relatively low capacity compared to Sn and Si. TiO_2 has a theoretical capacity of up to 335 mAh g^{-1}, while $Li_4Ti_5O_{12}$ has a theoretical capacity of only 175 mAh g^{-1}.

1.7 Summary

Table 1.1 Comparison of cathode materials for large-scale LIBs

Candidates	Potential/V	Theoretical	Practical	Rate	Safety	Cycleability

	(vs. Li^+/Li)	capacity/ mAh g^{-1}	capacity/ mAh g^{-1}	Performance		
$LiCoO_2$	>3.9	270	140	Good	Fair	Fair
$LiCo_{1/3}Ni_{1/3}Mn_{1/3}O_2$	>3.7	270	200†	Fair	Poor†	Poor†
$LiMn_2O_4$	4.1	140	120	Fair	Poor	Poor
$LiNi_{0.5}Mn_{1.5}O_4$	4.7	140	120	Fair	Poor	Fair
$LiFePO_4$	3.4	170	140-160*	Good*	Excellent	Excellent
$LiFe_xMn_{1-x}PO_4$	4.0/3.5	170	100-160*‡	Poor*	Good	Good
$LiVPO_4F$	4.2	155	130*	Fair*	Good	Good

† charged to 4.6 V vs. Li^+/Li

* after proper modifications

‡ largely depends on the processing and Mn content

Table 1.1 summarizes the basic features of the candidate cathode materials for the next generation LIBs in large-scale applications. In summary, phosphate cathode materials, particularly $LiFePO_4$, are probably the most promising candidates for large-scale applications owing to their crucial advantages on safety features, cycleability and lattice stability over the oxide materials. $LiFePO_4$ is also economical, nontoxic, and environmentally friendly. Over the past decade, researchers have spent most efforts on $LiFePO_4$ due to its superior potential as cathode materials for large-scale applications. However, as shown in Table 1.1, the operation potential of $LiFePO_4$ is relatively lower than most of the oxide cathode materials. On the other hand, isomorph $LiFe_xMn_{1-x}PO_4$ ($0 \le x \le 1$) and tavorite $LiVPO_4F$ with high potential of ~4 V may be promising for the next generation high power LIBs. Nevertheless, the poor electronic

and ionic conductivity hinder their rate performances. To overcome these drawbacks, these phosphate materials need to be modified through cation doping/substituion, conductive coating, and/or nano-structuring.

This research work mainly focuses on the development of high rate performance phosphate materials with olivine and tavorite structure. Firstly, electrical conductive olivine $LiFePO_4$ was achieved through supervalent doping in Chapter 3, and through carbon coating in Chapter 4. Carbon coated olivine $LiFePO_4$ was synthesized with a facile liquid phase polymer assisted mechanical activation. Both strategies have demonstrated impressive improvements in electrochemical performances. Then, carbon coated high potential "4V" olivine $LiFe_xMn_{1-x}PO_4$ ($0 \leq x \leq 1$) and tavorite $LiVPO_4F$ that may qualify the next generation of large-scale LIBs were developed in Chapter 4 and Chapter 5. Electronic conductivities and ionic diffusivity, electrochemical properties, and Li^+ extraction/ insertion mechanisms of tavorite $LiVPO_4F$ have also been studied in detail. Unlike the extensively researched olivine materials, some inherent properties and mechanisms of tavorite materials are still not uncovered with very few reports. The study of the tavorite materials will reveal the limitation factor and guide the further modification of these materials. Thirdly, a novel solution based synthesis route based on phosphonate compounds was proposed for the first time and preliminarily studied in Chapter 6. This synthesis route can be applied to synthesize various kinds of phosphate materials with nanoparticles formed 3d secondary architectures. Finally, nanosized TiO_2 was developed in Chapter 7 through a

facile and economical mechanochemical milling. The nanosized TiO_2 may be a safer alternative of the conventional graphite anode to couple with the high rate performance phosphate materials developed in this work.

2 Experimental Approach

2.1 Material Preparation

Most of the materials were synthesized via a conventional solid-state reaction in this dissertation, expect for Chapter 7 in which a novel solution based wet-chemistry method is proposed and preliminarily studied. Generally, solid-state reaction involves a mechanical milling process to mix and mill raw materials into homogenous fine powders. Thereafter, chemical reactions take place through solid-state diffusion, nucleation and grain growth at elevated temperature, thus yielding the crystallized material. Details of the material preparation will be elaborated in each chapter.

2.2 Material Characterization

2.2.1 Elemental Analysis

Elemental analysis, especially inductively coupled plasma atomic emission spectroscopy (ICP-AES), was used to determine the elemental ratio in the synthesized material. The ICP-AES technology offers high precision detections of trace amount of heavy metal element.

2.2.2 X-ray diffraction

Crystal structure of the material investigated was identified using powder X-ray diffraction (XRD, Shimadzu XRD-6000/7000, Cu Kα radiation). To acquire credible diffraction results with high counts, most of the XRD measurements were carried out

using continuous scan mode with a scanning rate of 1 °/min. For Rietveld refinement, high count XRD data were obtained using step scan mode with 0.02 °/step and long duration of up to 12 s per step.

Nanocrystalline materials have noticeable XRD peak broadening effects. Average crystallite size can be therefore estimated from XRD peak broadening by application of Scherrer equation:

$$d = \frac{0.89\lambda}{(B-B_0)cos\theta} \quad \text{Equation 2.1}$$

where λ is the X-ray wavelength ($K\alpha_1$, 1.540563 Å), B is the half maximum intensity (FWHM) of XRD peak in radians, B_0 corresponds to equipment broadening effects, and θ is the Bragg angle. To achieve high precision estimation, $K\alpha_2$ contributions were subtracted by software, while instrumental broadening (B_0) were corrected based on the diffraction data of standard polycrystalline silicon powders (325 mesh).

2.2.3 Raman spectroscopy

Raman spectroscopy is a spectroscopic technique widely used to characterize vibrational, rotational and other low-frequency modes in a material. An excitation laser of 532 nm wavelength was adopted for the Raman spectra measurements in current work. Raman spectroscopy is an effective analysis technique to identify the existence and disordered state of carbon coatings in the materials. Pyrolysis carbon coating in electrode materials are normally in amorphous form due to the low calcination temperature <800 ºC. Amorphous carbons show different electronic and mechanical

properties according to the clustering of π states (sp^2 in aromatic rings). Amorphous carbons with higher ordered sp^2 phase normally have better electronic conductivity.

As shown in Fig. 2.1, the main peaks of carbon in the Raman spectra are located at about 1580 cm^{-1} and 1360 cm^{-1} known as G band and D band, respectively. The peak intensity, position and width provide information on the disorder state of carbon hexagonal aromatic rings. The G band is caused by E_{2g} bond stretching of all pairs of sp^2 atoms in both rings and chains, while the D band is caused by A_{1g} breathing modes of sp^2 atoms in rings [131]. The ratio between the intensities of D and G peaks, I_D/I_G, is believed to be proportional to the number and cluster of aromatic rings in amorphous carbon [131-133]. Hence, the degree of graphitic disorder of the carbon coatings can be estimated through the measurement of I_D/I_G ratio. Higher value of I_D/I_G indicates less ordered graphite like sp^2 states, which normally implies better electronic conduction [134].

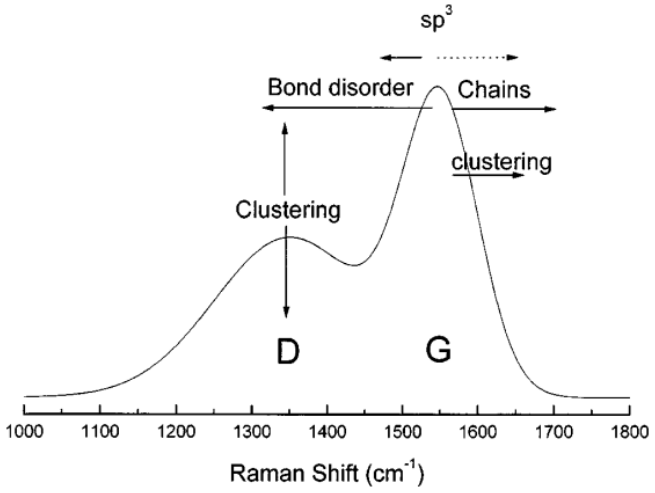

Fig. 2.1 Raman spectra of amorphous carbon[132]

2.2.4 Electron Microscopy

Electrochemical properties of electrode materials significantly depend on their micromorphology and particle size. Micromorphology and particle size of the materials investigated were directly observed using field-emission scanning electron microscopy (FE-SEM, Hitachi S-4300) and high-resolution transmission electron microscopy (TEM, JEOL-2010F).

2.2.5 Conductivity Measurement

Total electrical conductivity and electronic conductivity of dense pellets were measured by alternating current (AC) impedance spectroscopy and direct-current (DC) polarization using the Solartron 1260 frequency response analyzer and Solartron 1287 electrochemistry interface. For instance, a typical disc pellet is of ~10 mm in diameter and ~1 mm in thickness with a density at least 80% of the theoretical value. Ionic blocking gold or platinum electrodes were sputtered on both faces of the disc pellets.

AC impedance spectroscopy was carried out in the frequency range from 10^7 Hz to as low as 0.01 Hz. The intercept of the semi-circle with the *Z'* axis is used to calculate the AC conductivity σ_{AC}. Electronic conductivity σ_{DC} was determined using chronoamperometry from null to 500 mV at room temperature with a step interval of 50 mV. After each step of voltage increase, the voltage ΔU was stabilized for 1 h. In the beginning the current should be contributed by movement of electrons, holes and Li^+ ions in the electric field, thereafter the current gradually will decrease with

prolonged time due to polarization of Li^+. After sufficient long time of polarization, a stationary current $I_{stationary}$ was reached, which should be only contributed by electrons and holes. Therefore ΔU and $I_{stationary}$ should obey Ohm's law with electronic resistance $R_e = \Delta U/I_{stationary}$.

2.2.6 Thermal analysis

Simultaneous thermogravimetric analysis (TGA) and differential thermal analysis (DTA) were conducted using a Shimadzu DTG-60H. Thermal analysis is a useful tool to identify transformation and reactions upon heat treatment. Residual carbon content in the final products was also determined using TGA technique in this work.

2.3 Electrochemical Properties

2.3.1 Electrode preparation and battery assembly

Working electrodes were prepared by doctor-blade method. The active materials, carbon black (Super P) and polyvinylidenefluoride (PVDF, 99%, Sigma-Aldrich) were thoroughly ground and mixed in weight ratio of 80: 15: 5 in solvent n-methyl-2-pyrrolidone (NMP) to obtain a homogenous slurry. The viscous slurry was then pasted on an aluminum or copper foil to obtain the working electrodes. Active material loading densities of the working electrodes were controlled in the range of 3-6 mg cm^{-2} unless otherwise specified. Working electrodes were pressed using a rolling machine to enhance electronic contact followed by drying at 120 ºC for 12 h in a vacuum

oven before battery assembly. Two-electrode Swagelok^{TM} type half-cells were assembled in an argon glove box. A Celgard 2500^{TM} separator was sandwiched between the working electrode and a 0.59 mm thick metallic lithium foil. The electrolyte consists of 1 M LiPF6 in ethylene carbonate (EC), diethyl carbonate (DEC) and dimethyl carbonate (DMC) (DC: EC: DMC, 1:1:1, vol.) solutions.

2.3.2 Cyclic voltammetry

Cyclic voltammetry (CV) on half-cells was carried out using Solartron 1287 electrochemistry interface. CV is a widely used potentiodynamic electrochemical technique in research of LIBs and many other electrochemical systems. In a CV test, a linearly ramping potential known as scan rate in mV s^{-1} is applied to a cell, while the current response is recorded. CV curve recorded at slow scan rate provides useful thermodynamic information of the redox potential and polarization of the electrochemical reactions. The potential hysteresis ΔV (peak separation between cathodic and anodic peaks) indicates the polarization of the electrode.

2.3.3 Galvanostatic charge-discharge

Galvanic charge and discharge tests were carried out using Maccor 4304 and Neware BTS-5V1A. Specific capacity is defined as the capacity that a material can deliver at a reasonably small current rate, normally 0.2C or 0.1C in this work. 1C is normally defined as the current that can ideally charge/discharge the maximum attainable capacity or theoretical capacity in one hour. For instance, 1C is defined to be

160 mA g^{-1} for olivine $LiMPO_4$ (M = Fe, Mn) and 150 mA g^{-1} for tavorite $LiVPO_4F$ in this work. As for rate capability tests, the half-cells were first fully charged/discharged at a low current density of 0.1C or 0.2C, and then discharged/charged at various higher current densities. Normally, the capacity will decline with increase in current density and rate, while working voltage polarized from the equilibrium potential, due to the bottleneck effects of reaction speed, electronic transport or ionic diffusion. Discharge rate capability represents power and energy density that a particular cathode material can deliver, while charge rate capability shows how fast the cathode material can be charged. In long-term cyclic tests, the cell will be charge-discharged at high current rates for hundreds of cycles to challenge the lattice stability and electrode-electrolyte stability.

2.3.4 Electrochemical impedance spectroscopy

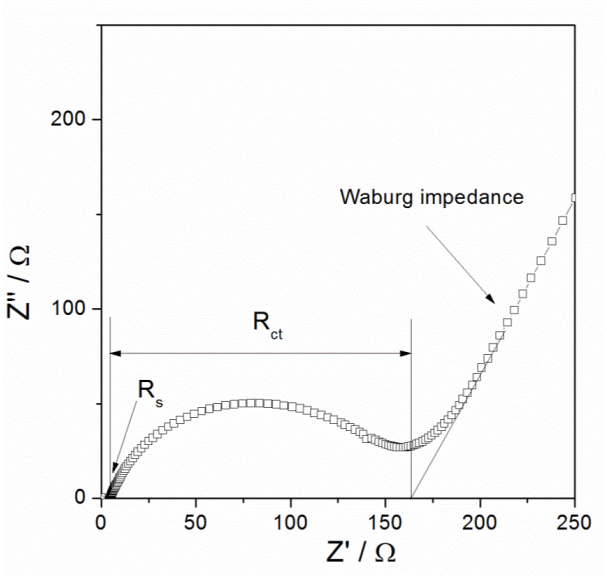

Fig. 2.2 Schematic of Nyquist plot of EIS of lithium-ion batteries

Electrochemical impedance spectroscopy (EIS) of half-cells were carried out at steady state using the Solartron 1260 frequency response analyzer and Solartron 1287 electrochemistry interface. As shown in Fig. 2.2, a typical Nyquist plot of EIS of LIBs comprises of at least one semicircle in high and mid frequency range and a sloping line in low frequency range. Such an EIS spectrum can be fitted with equivalent circuit shown in Fig. 2.3 (a). The first interception of the semicircle on the *Z'* axis reflects the Ohmic resistance R_s of the electrolyte, electrode contact, current collector and separator. The semicircle reflects the charge transfer resistance R_{ct} and the double layer capacitance C_{dl} of the electrochemical reaction of the electrode. In lithium-ion batteries, charge transfer reaction, or Faradic reaction, refers to the electrical charge transfer between electrode and electrolyte occurring at the electrode surface. Charge transfer resistance R_{ct} is a quantified characteristic for the charge-transfer step and is indicative of the inherent speed of the electrode reaction. A large charge transfer resistance R_{ct} indicates a slow Faradic reaction speed. Double layer capacitance C_{dl} is induced by the separation of the positively charged Li^+ ions and the negatively charged electrons at the boundary of the electrode reaction. Warburg impedance reflects the diffusion of the electrical charges (Li^+ ions in LIBs) in solid phases in the low frequency area where the diffusion of Li^+ in the bulk phase electrode material dominated the reaction speed.

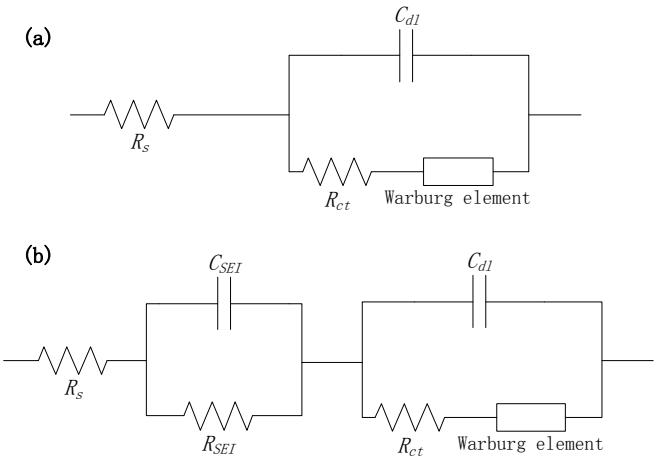

Fig. 2.3 Equivalent circuit for EIS of lithium-ion batteries
(a) with little influence of SEI, and (b) with considerable influence of SEI.

In some occasions, another semicircle contributed by solid electrolyte interface (SEI) layer may be observed at the low frequency range of the EIS spectra. SEI is a passivation layer formed on electrode in contact with electrolyte. SEI layer has the properties of a solid electrolyte and acts as an interface between the electrode and the electrolyte. As shown in Fig. 2.3 (b), the contribution of SEI is represented by an equivalent circuit of parallel resistance R_{SEI} and capacitance C_{SEI}. R_{SEI} can be seen as indicative of the resistance and thickness of the SEI layer on the electrode surface.

3 Ru^{4+} trace doping on M1 site of olivine $LiMPO_4$ (M = Fe, Mn, and Co)

3.1 Material design

To improve the electronic transport of olivine materials, supervalent Ru^{4+} trace doping on M1 site of $LiMPO_4$ (M= Fe, Mn and Co) has been studied in this chapter using RuO_2 as dopant. To the knowledge of the author, this is the first attempt of Ru^{4+} doping in olivine type cathode materials.

As described in Chapter 1, supervalent cation doping on M1 (Li) site has been proven as an effective solution to improve electronic transport of olivine $LiFePO_4$. Few reports have been published on the trace doping of cations with free 4*d* electrons. Although the trace doping of other 4*d* elements such as Y^{3+} ($4d^0 5s^0$), Zr^{4+} ($4d^0 5s^0$), Nb^{5+} ($4d^0 5s^0$) and Mo^{6+}($4d^0 5s^0$) have been reported [46, 68, 79, 135-137], the 4*d* orbitals of these ions are empty. On the other hand, the Ru^{4+} ($4d^4$) can contribute two free unpaired 4*d*-electrons and may increase the charge carrier concentration in the crystal lattice. Owing to this unique electronic configuration of Ru^{4+}, the dopant RuO_2 is a very rare 4*d*-band metallic conductive oxide with extraordinarily high electronic conductivity up to 10^4 S cm^{-1} [138], in contrast to other insulating oxide dopants such as Cr_2O_3, MgO, ZrO_2, Nb_2O_5 and MoO_3 [46, 70, 71]. The high electronic conductivity of RuO_2 is believed to be contributed by Ru^{4+}-O^{2-} π^* electron band just at the Fermi level [139]. Compounds of Ru^{4+} ($4d^4$) such as Li_2RuO_3 also exhibit very high electronic

conductivity [46, 71]. Wang et al. successfully doped up to 5 mol% Ru^{4+} into the octahedral sites of spinel cathode material $LiNi_{0.5}Mn_{1.5}O_4$, resulting in 5 folds increase in electronic conductivity [140]. RuO_2 has also been widely used in the study of glass composites to enhance the total electronic conductivity [141-143], in super-capacitors and as anode materials in LIBs [144, 145]. Ru^{4+} has a 6-fold radii of 0.62 Å [146] that is very close to those of the doped cations in previous reports [46, 135-137] such as Mo^{6+} (0.59 Å [146]), Ti^{4+} (0.605 Å [146]) and Nb^{5+} (0.64 Å [146]), smaller than the host ions of Li^+ (0.76 Å [146]) and Fe^{2+} (0.78 Å [146]) in olivine lattice. Therefore, Ru^{4+} tracing doping in the olivine lattice is supposed to be feasible.

With these advantages in mind, defected $Li_{1-4x}Ru_xFePO_4$ was designed according to the following defect chemistry reaction:

$$LiFePO_4 \underset{Ru^{4+}}{\Rightarrow} (1-4X)Li_{Li}^{x} + 3XV_{Li}^{'} + XLi_{R_u}^{\bullet\bullet\bullet} + Fe_{Fe}^{x} + P_P^x + 4O_O^x$$

where each Ru^{4+} occupies M1 (Li) site with three Li vacancies for electro-neutrality according to ref. [70] and [71]. In this design, the $Li_{Ru}^{\cdots}$ holes and the free 4*d* electrons of Ru^{4+} may both contribute to the electronic conduction in $Li_{1-4x}Ru_xFePO_4$. In Section 3.2, $Li_{1-4x}Ru_xFePO_4$ with x = 0.005, 0.01, 0.02 and 0.03 were prepared and characterized in this chapter. Thereafter, the effects of supervalent Ru^{4+} doping on high potential olivine $LiMnPO_4$ and $LiCoPO_4$ were also explored subsequently in Sections 3.3 and 3.4.

3.2 Ru^{4+} doping on M1 site of $LiFePO_4$

3.2.1 Material preparation

Pristine $LiFePO_4$ and $Li_{1-4x}Ru_xFePO_4$ (x = 0.005, 0.01, 0.02 and 0.03) were synthesized via a conventional solid-state reaction. In a typical route, stoichiometric amounts of iron (II) oxalate dihydrate ($FeC_2O_4 \cdot 2H_2O$, 99%, Aldrich), lithium carbonate (Li_2CO_3, 99%, Riedel-de Haën), ammonium dihydrogen phosphate ($NH_4H_2PO_4$, 99%, Arcos) and ruthenium dioxide (RuO_2, 99.9%, Aldrich) were ball milled in liquid acetone or ethanol at 300 rpm for 2 h. Acetone and ethanol act as dispersing agent to protect the sensitive Fe^{2+} from oxidization during rigid milling. Grinding media are zirconia (ZrO_2) balls of 3 mm and 10 mm in diameter. The ratio between zirconia grinding media and raw materials is roughly 5:1 by weight. The milled homogenous slurry was dried at 80 ºC and then pre-calcinated at 350 ºC for 10 h in flowing argon to expel gases of CO_2, H_2O and NH_3 in the reactants. The pre-calcinated powder was reground and finally calcinated at 600-800 ºC for 12 h in flowing argon.

3.2.2 Characterization

3.2.2.1 Elemental analysis

An essential concern in the processing of trace-doping and solid-state reaction is whether the elements, particularly the dopant elements, can be homogenously distributed throughout the material. Table 3.1 shows the results of elemental analysis of pristine $LiFePO_4$ and $Li_{0.96}Ru_{0.01}FePO_4$. The elemental ratio results were normalized

based on Fe. The ICP-AES results demonstrate that the composition of the synthesized materials is generally consistent with design. The content of lithium is slightly lower than the designed value for both materials. This is probably caused by the low sensitivity of ICP-AES technique to light atoms and/or lithium volatilization during calcination.

Table 3.1 Elemental analysis results of $LiFePO_4$ and $Li_{0.96}Ru_{0.01}FePO_4$

Sample	Li	Fe	P	Ru
$LiFePO_4$	0.9813	1.000	1.004	N.A.
$Li_{0.96}Ru_{0.01}FePO_4$	0.9387	1.000	1.016	0.008

3.2.2.2 Crystal structure

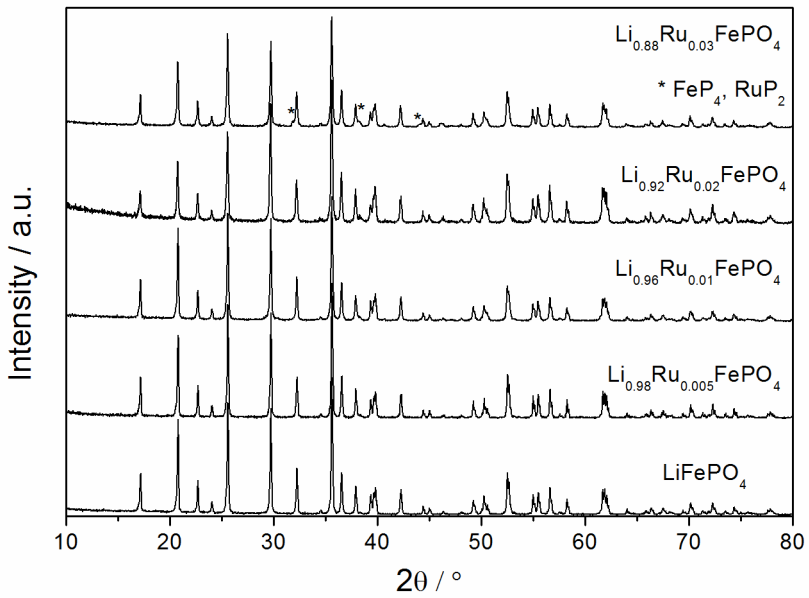

Fig. 3.1 XRD spectra of $LiFePO_4$ and $Li_{1-4x}Ru_xFePO_4$ (x = 0.005, 0.01, 0.02 and 0.03)

Fig. 3.1 shows the XRD spectra of pristine $LiFePO_4$ and $Li_{1-4x}Ru_xFePO_4$ (x = 0.005, 0.01, 0.02 and 0.03). As can be seen, the diffraction patterns show single-phase olivine

structure for pristine $LiFePO_4$ and $Li_{1-4x}Ru_xFePO_4$ with x up to 0.02. Impurities such as RuP_2 and or FeP_4 start to emerge with x = 0.03. This is in line with reports of other supervalent cation dopants [73, 147] in which the occupancy of foreign metal dopant on M1 site of $LiFePO_4$ was found to be normally less than 3 mol%. Table 3.2 summarizes the Rietveld refined lattice parameters using GSAS+EXPGUI. Due to pronounced impurity phases, $Li_{0.88}Ru_{0.03}FePO_4$ was not involved in this refinement. As can be seen, the lattice parameters *a, b* and the unit cell volume of $Li_{1-4x}Ru_xFePO_4$ increase proportionally over the compositional range x from 0 to 0.01, which follows Vegard's law very well. *a* and *b* of $Li_{0.96}Ru_{0.01}FePO_4$ are ~0.15% and ~0.1% larger respectively than those of pristine $LiFePO_4$, while the unit cell volume of $Li_{0.96}Ru_{0.01}FePO_4$ is ~0.3% larger than that of pristine $LiFePO_4$. This further demonstrates that the lattice of $LiFePO_4$ can probably accommodate at least 1 mol% of Ru^{4+}. The lattice expansion after trace doping is in line with other dopant of Nb^{5+} and Zr^{4+} [71]. It is interesting to find that the lattice parameters of $Li_{0.92}Ru_{0.02}FePO_4$ are not larger than those of $Li_{0.96}Ru_{0.01}FePO_4$ as expected. Therefore, the practical Ru^{4+} concentration in the lattice of $Li_{0.92}Ru_{0.02}FePO_4$ might be lower than the designed value. The attainable solubility of supervalent cations in olivine lattice may largely depend on the ionic radii, particle size, sintering temperature and synthesis route, as suggested by ref. [71]. XRD analysis suggests that the solubility limit of Ru^{4+} in the lattice of $LiFePO_4$ is probably $\leq$ 2 mol% with the current processing condition.

Table 3.2 Lattice parameters of pristine $LiFePO_4$ and $Li_{1-4x}Ru_xFePO_4$

Composition	*Lattice parameters*				*Refinement parameters*		
	a (Å)	*b* (Å)	*c* (Å)	*V* (Å^3)	R_{wp}	R_p	CHI^2
x=0	10.3256(4)	6.0077(2)	4.6947(2)	291.23(2)	12.3%	9.39%	3.69
x=0.005	10.3303(4)	6.0103(2)	4.6968(2)	291.62(2)	10.98%	8.24%	2.982
x=0.01	10.3412(5)	6.0140(3)	4.6958(2)	292.04(5)	10.25%	7.83%	1.645
x=0.02	10.3334(3)	6.0091(2)	4.6987(2)	291.83(2)	7.7%	6.17%	2.136

3.2.2.3 XPS analysis

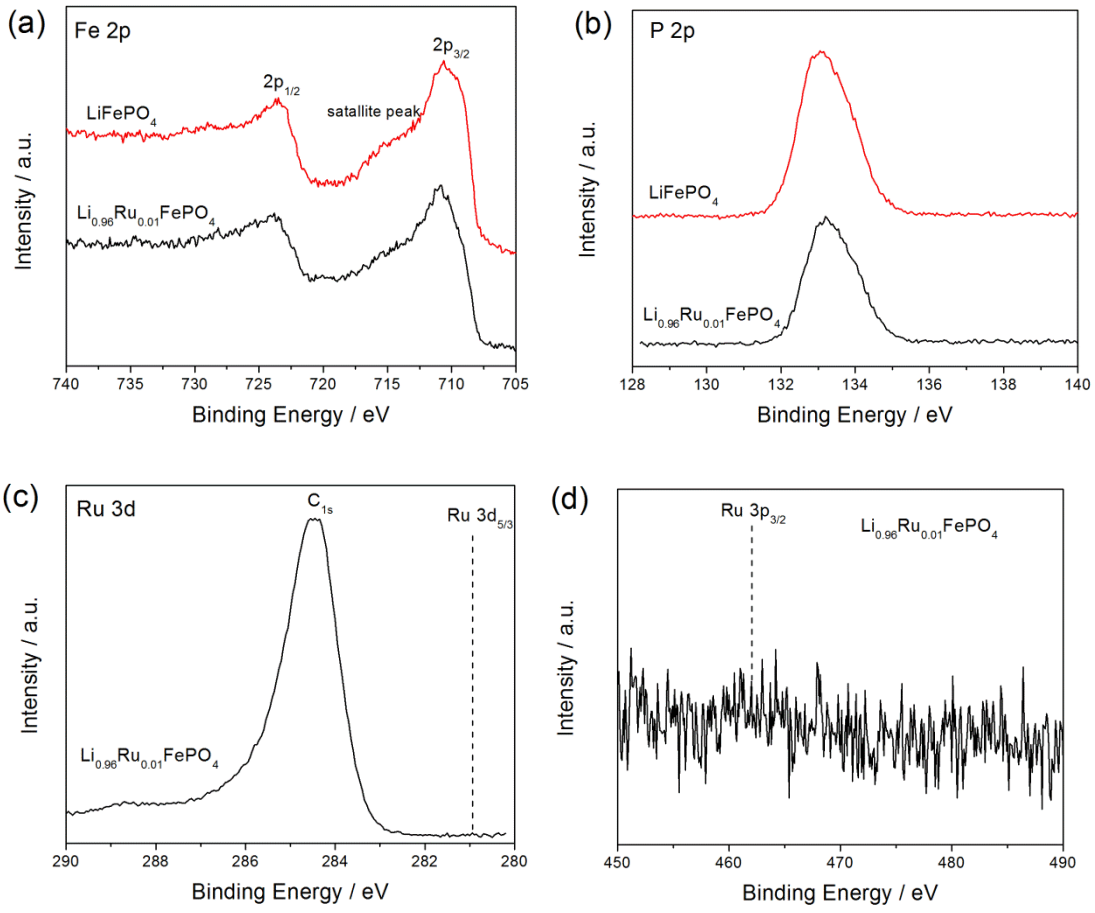

Fig. 3.2 XPS peaks of $LiFePO_4$ and $Li_{0.96}Ru_{0.01}FePO_4$; (a) Fe 2p, (b) P 2p, (c) Ru 3d and (d) Ru 3p

The surface chemistry of the pristine and Ru^{4+} doped $LiFePO_4$ particles was investigated using XPS. Fig. 3.2 shows the XPS peaks of $LiFePO_4$ and $Li_{0.96}Ru_{0.01}FePO_4$. Both materials show the similar peaks of Fe 2p and P 2p in Fig. 3.2 (a) and (b), which agrees well with literatures [148, 149]. The Fe $2p_{1/2}$ and Fe $2p_{3/2}$ peaks are characteristics of the Fe^{2+}, which are located at 723.8 eV and 710.4 eV for $LiFePO_4$, and 724.0 eV and 710.9 eV for $Li_{0.96}Ru_{0.01}FePO_4$. No characteristic peaks of phosphides (FeP, Fe_2P etc.) or Li_3PO_4 surface impurities [97] have been observed from XPS spectra of both pristine and Ru^{4+} doped $LiFePO_4$. Conductive phase $NbOPO_4$ has been found on the particle surface of the Nb^{5+} doped $LiFePO_4$ [69]. However, in this work, the characteristic peaks Ru $3d_{5/3}$ and Ru 3p of ruthenium were not observed in the XPS spectrum of $Li_{0.96}Ru_{0.01}FePO_4$. This demonstrates that the trace amount of RuO_2 has been successfully doped in to the lattice rather than coated on the particle surface.

3.2.2.4 Micromorphology

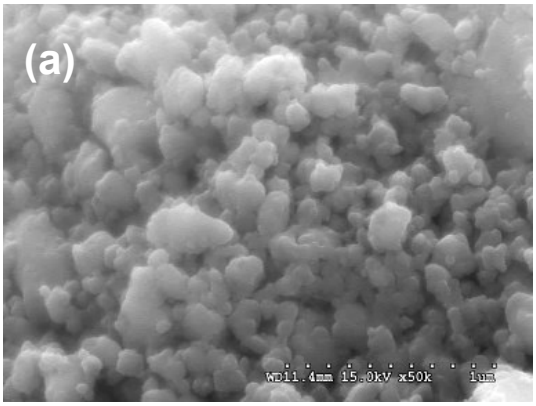

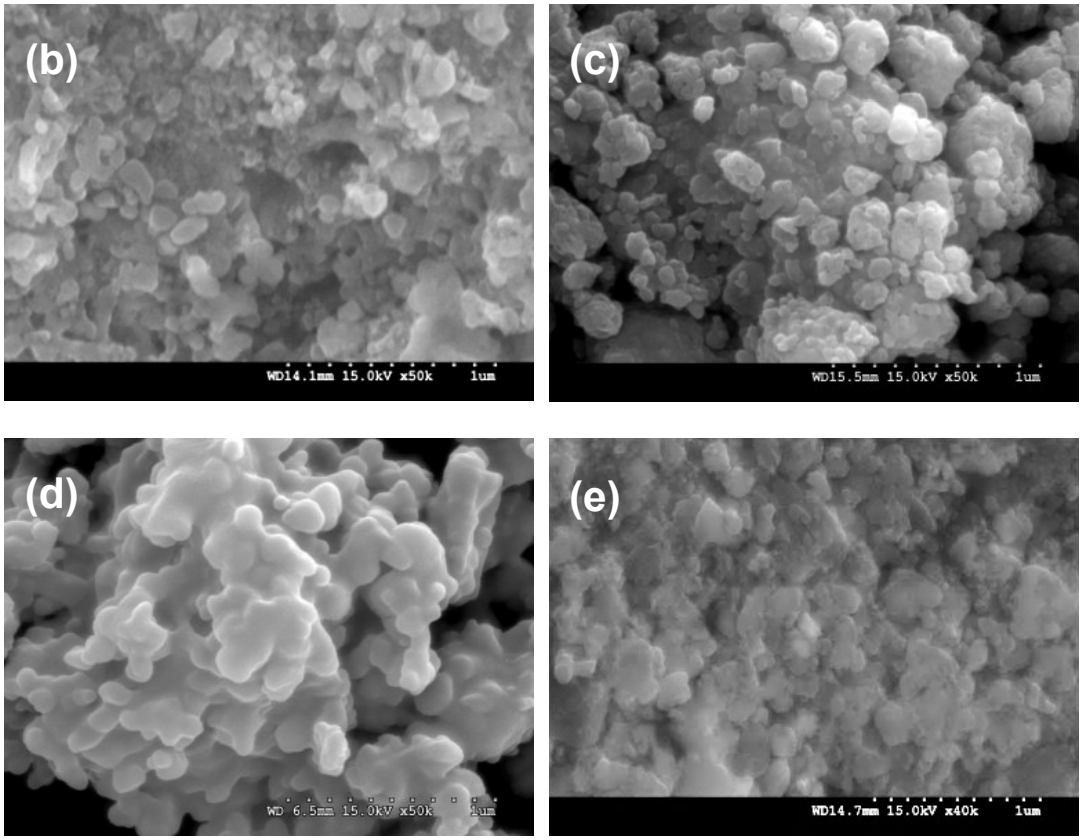

Fig. 3.3 SEM images of LiFePO4 and $Li_{1-4x}Ru_xFePO_4$;
(a) pristine $LiFePO_4$, (b) x=0.005, (c) x=0.01, (d) x=0.02 and (e) x=0.03.

Fig. 3.3 shows the FE-SEM images of pristine $LiFePO_4$ and $Li_{1-4x}Ru_xFePO_4$ (x= 0.005, 0.01, 0.02 and 0.03). As can be seen, all these materials have similar particle sizes and micro-morphologies due to the same processing. Primary particle sizes of pristine $LiFePO_4$ and $Li_{1-4x}Ru_xFePO_4$ are mostly in the range of 50-150 nm. The nanosized primary particle enables the extraction of lithium from the innermost part of the particles. Secondary particles are randomly shaped with size from ~200 nm to tens of micrometers. Due to the agglomerated morphology, the intrinsic electronic conductivity and electron transport inside and between primary particles may largely influence the matrix electronic transport as in the electrodes.

3.2.2.5 Conductivity

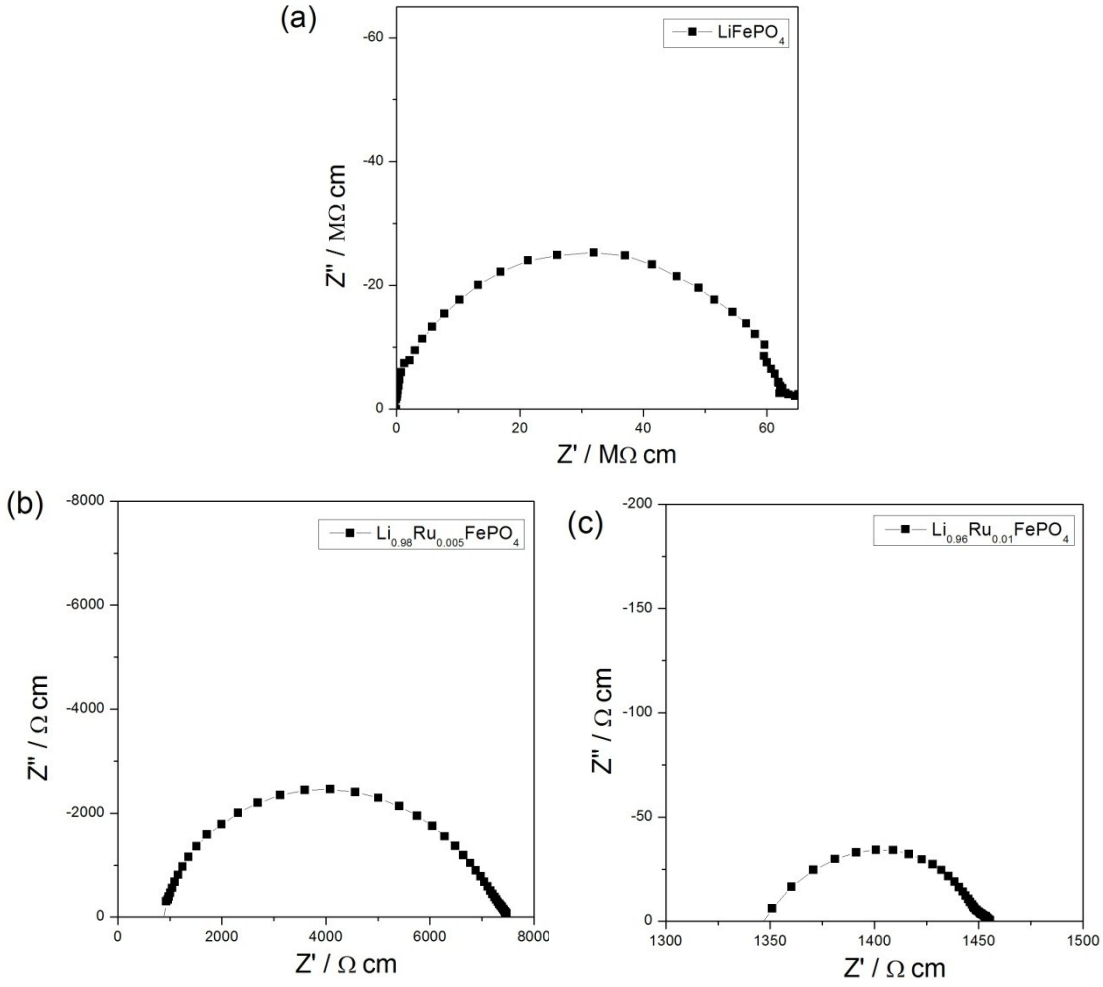

Fig. 3.4 AC impedance spectra of Au/$Li_{1-4x}Ru_xFePO_4$/Au pellets;
(a) pristine $LiFePO_4$, (b) $Li_{0.98}Ru_{0.005}FePO_4$ and (c) $Li_{0.96}Ru_{0.01}FePO_4$

To measure the electrical and electronic conductivity of $LiFePO_4$ and $Li_{1-4x}Ru_xFePO_4$, dense ceramic disc pellets of ~10 mm in diameter and 1 mm in thickness were prepared. The 350 ºC pre-calcinated powders of $LiFePO_4$ and $Li_{1-4x}Ru_xFePO_4$ were pelletized using an axial pressure of 250 MPa. The pellets were then sintered at relatively high temperature of 800-900 ºC for 12 h to promote grain growth. To prevent lithium deficiency, the pellets were immersed in powders of the

same composition during the high temperature sintering. Both faces of the as-prepared disc pellets were ground and polished before the deposition of gold (Au) electrode.

Fig. 3.4 shows the Cole-Cole plots of AC impedance spectra of pristine $LiFePO_4$ and $Li_{1-4x}Ru_xFePO_4$ (x = 0.005 and 0.01) dense pellets measured at room temperature (25 ºC). Only one semicircle can be observed from each impedance spectrum. This semicircle reflects the total electrical resistance of the bulk phase, whereas grain boundary effects can be neglected. The total electrical conductivity of pristine $LiFePO_4$ is 1.58×10^{-8} S cm^{-1}, slightly higher than that (1.39×10^{-9} S cm^{-1}) reported in ref. [45]. With trace amount of RuO_2 doping, electrical conductivity of $Li_{0.98}Ru_{0.005}FePO_4$ and $Li_{0.96}Ru_{0.01}FePO_4$ increases dramatically to 1.34×10^{-4} S cm^{-1} and 6.87×10^{-4} S cm^{-1} respectively, four orders higher than that of pristine $LiFePO_4$. As for $Li_{0.92}Ru_{0.02}FePO_4$ and $Li_{0.88}Ru_{0.03}FePO_4$, complete impedance semicircles cannot be obtained due to their tiny impedance values. Electrical conductivities of $Li_{0.92}Ru_{0.02}FePO_4$ and $Li_{0.88}Ru_{0.03}FePO_4$ were simply calculated from the intercept of Cole-Cole plot on the Z' axis.

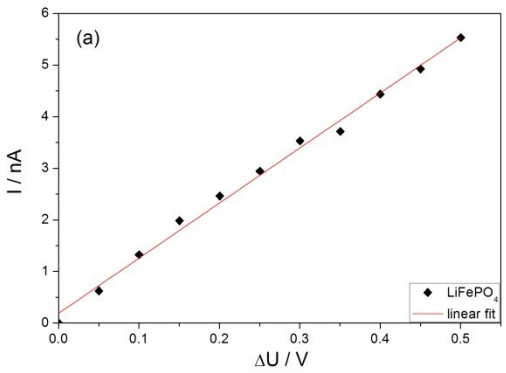

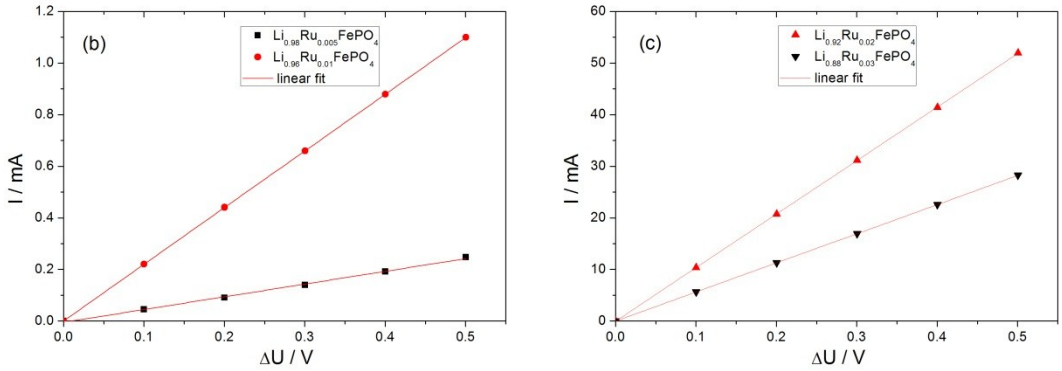

Fig. 3.5 I-V relationship in DC conductivity measurements of pristine $LiFePO_4$ and $Li_{1-4x}Ru_xFePO_4$; (a) pristine $LiFePO_4$, (b) x=0.005 and 0.01 and (c) x=0.02 and 0.03.

To derive the contribution of electronic conductivity to the total electrical conductivity, DC polarization chronoamperometry measurements were carried out using ionic blocking Au/$Li_{1-4x}Ru_xFePO_4$/Au pellets. Fig. 3.5 shows the I-V relationship in the DC electronic conductivity measurements at room temperature. All the pellets of different compositions show good Ohmic behavior with DC polarization up to 500 mV.

The calculated electrical and electronic conductivities are summarized in Fig. 3.6. As can be seen, $Li_{1-4x}Ru_xFePO_4$ (x = 0.005, 0.01, 0.02 and 0.03) materials have much higher electrical and electronic conductivity than $LiFePO_4$, while the total electrical conductivities are mainly contributed by the electronic transport. With only 0.5 mol% dopant concentration, $Li_{0.98}Ru_{0.005}FePO_4$ shows an electronic conductivity of 1.15×10^{-4} S cm^{-1}, 5 orders higher than that (2.66×10^{-9} S cm^{-1}) of pristine $LiFePO_4$. The electronic conductivity of the RuO_2 doped $LiFePO_4$ is comparable with that of the traditional oxide cathode materials such as $LiCoO_2$ (~10^{-3} S cm^{-1} [7]) and $LiMn_2O_4$ (~10^{-5} S cm^{-1} [14]). The electronic conductivity of $Li_{1-4x}Ru_xFePO_4$ generally increases with dopant concentration x over the compositional range of $0 \leq x \leq 0.02$. $Li_{0.92}Ru_{0.02}FePO_4$ has the

highest electronic conductivity of up to 10^{-2} S cm^{-1}. On the other hand, $Li_{0.88}Ru_{0.03}FePO_4$ has slightly lower electronic conductivity when compared to $Li_{0.92}Ru_{0.02}FePO_4$, which is probably affected by the nonconductive phosphides impurities as indicated in the XRD analysis. This trend is also in line with ref. [46] in which the electronic conductivity decreases drastically to 10^{-6} S cm^{-1} with 4 mol% Nb^{5+}.

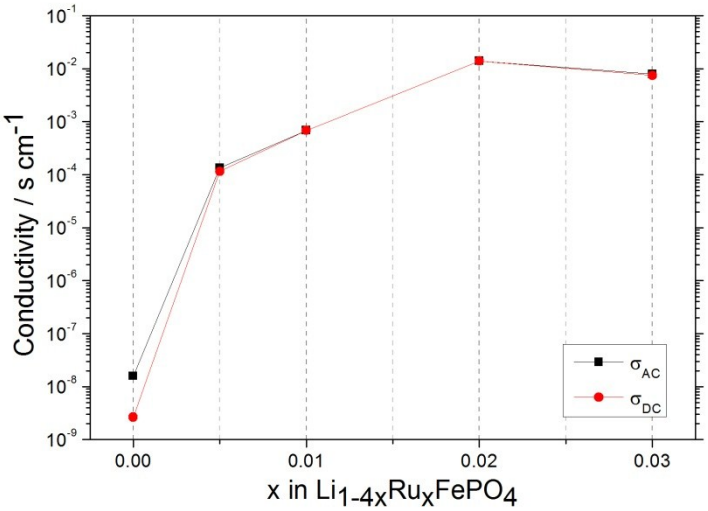

Fig. 3.6 Conductivity comparison of pristine $LiFePO_4$ and $Li_{1-4x}Ru_xFePO_4$

3.2.3 Electrochemical Properties

3.2.3.1 Cyclic voltammetry

Fig. 3.7 compares the cyclic voltammetry (CV) curves of pristine $LiFePO_4$ and $Li_{1-4x}Ru_xFePO_4$ (x=0.005, 0.01, 0.02 and 0.03) recorded at a slow scan rate of 0.1 mV s^{-1}. Pristine $LiFePO_4$ has only one pair of anodic and cathodic reactions at ~3.3/3.6 V that can be ascribed to the Fe^{2+}/Fe^{3+} redox couple in the olivine lattice. Likewise, the redox

couple of Fe^{2+}/Fe^{3+} was also located at ~3.3/3.5 V in the CV curves of $Li_{1-4x}Ru_xFePO_4$ with x = 0.005, 0.01, 0.02 and 0.03. No additional redox couple from Ru^{4+} can be found from the CV curves of $Li_{1-4x}Ru_xFePO_4$ (x=0.005, 0.01 and 0.02). This indicates that there is no electrochemically active impurity phase in the $Li_{1-4x}Ru_xFePO_4$ (x=0.005, 0.01 and 0.02) materials. However, the CV curve of $Li_{0.88}Ru_{0.03}FePO_4$ in Fig. 3.7 (e) reveals an additional redox couple at 4.04/4.08 V which should be ascribed to a reversible reaction of phosphides impurity phases etc.

The potential hysteresis ΔV characterizes the polarization and reaction resistance of the electrochemical reactions on the electrodes. As can be seen, Ru doping significantly reduces the potential hysteresis ΔV of $Li_{1-4x}Ru_xFePO_4$ electrodes due to the largely elevated inherent electronic conductivity of the active materials. $Li_{0.96}Ru_{0.01}FePO_4$ and $Li_{0.92}Ru_{0.02}FePO_4$ have the smallest ΔV of ~195 mV, almost 100 mV smaller than that of pristine $LiFePO_4$ (293 mV). On the other hand, potential hysteresis ΔV of $Li_{0.88}Ru_{0.03}FePO_4$ is ~40 mV higher than that of $Li_{0.96}Ru_{0.01}FePO_4$, although its electronic conductivity is even higher than that of $Li_{0.96}Ru_{0.01}FePO_4$. This is probably because of the impurity phases in $Li_{0.88}Ru_{0.03}FePO_4$ that impedes the Li^+ insertion and extraction on the particle surface.

Furthermore, all $Li_{1-4x}Ru_xFePO_4$ electrodes have much higher cathodic and anodic peak currents when compared to pristine $LiFePO_4$, indicating faster reaction rates and higher realizable capacities. Fig. 3.7 (c) indicates an anodic peak current of 0.45 A g^{-1} and a capacity of 157 mAh g^{-1} in the forward scan of $Li_{0.92}Ru_{0.02}FePO_4$ from 2 V to 4.5

V. On the other hand, Fig. 3.7 (a) indicates an anodic peak current of only 0.16 A g^{-1} and a capacity of only 74 mAh g^{-1} for the pristine $LiFePO_4$.

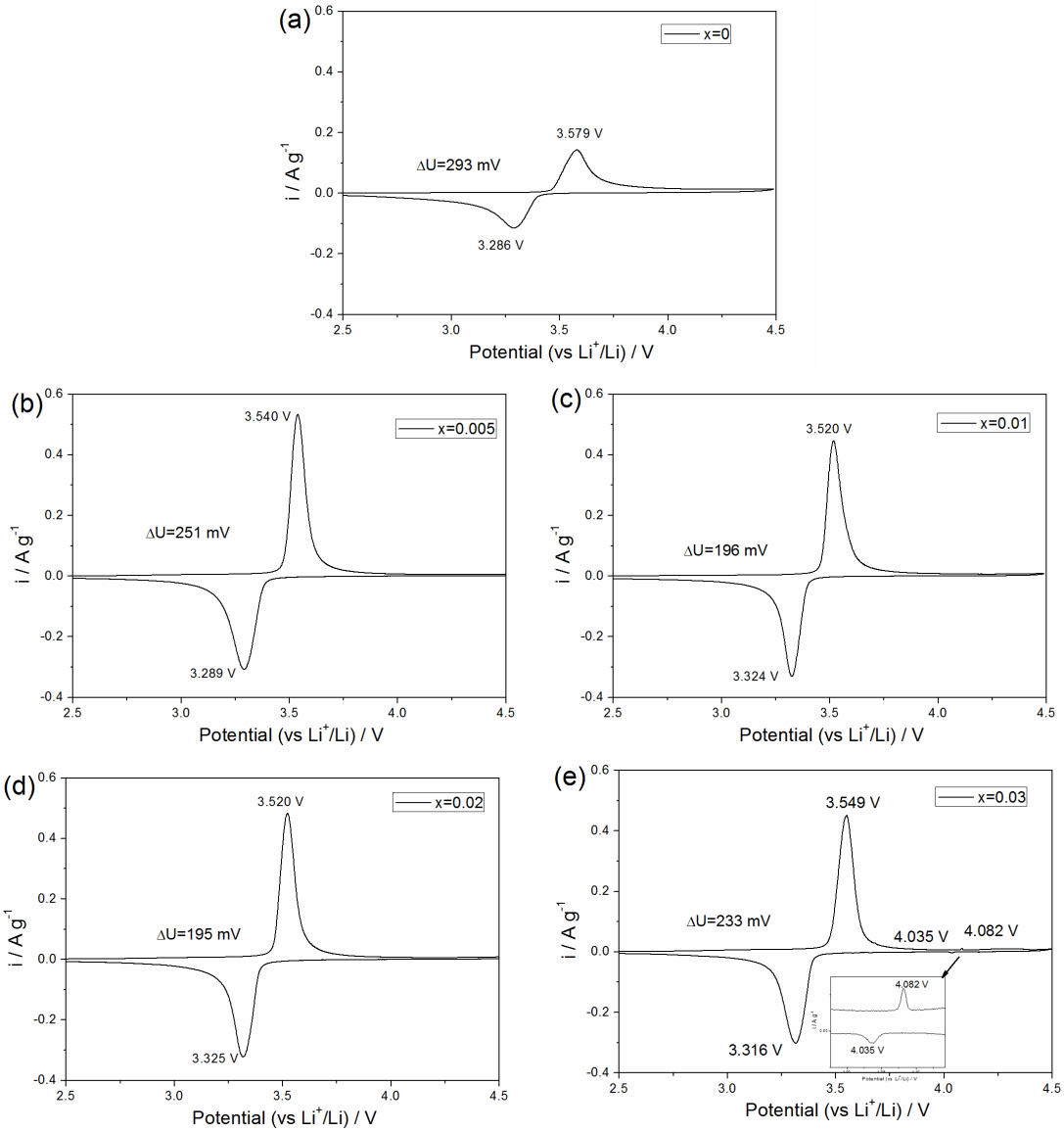

Fig. 3.7 Cyclic voltammetry of pristine $LiFePO_4$ and $Li_{1-4x}Ru_xFePO_4$ at a 0.1 mV s^{-1}. (a) pristine $LiFePO_4$, (b) x=0.005, (c) x=0.01, (d) x=0.02 and (e) x=0.03.

3.2.3.2 Electrochemical impedance spectroscopy

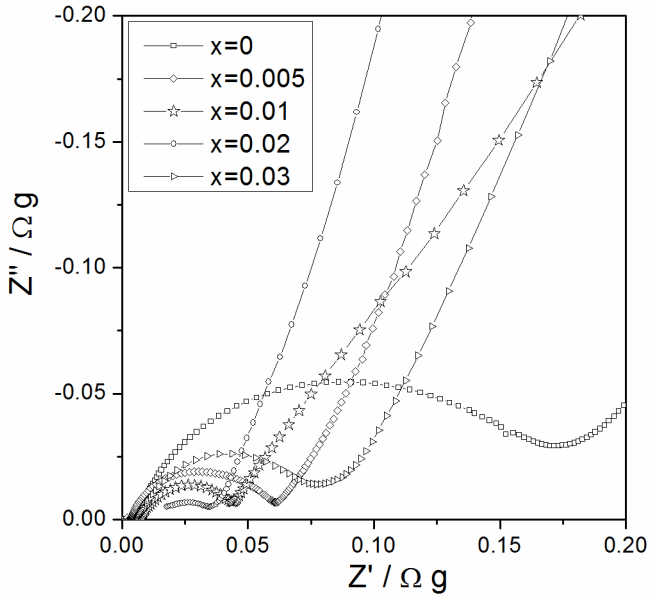

Fig. 3.8 Nyquist plots of EIS of $LiFePO_4$ and $Li_{1-4x}Ru_xFePO_4$ electrodes at fully discharged state.

Fig. 3.8 compares the EIS spectra of the electrodes of pristine $LiFePO_4$ and $Li_{1-4x}Ru_xFePO_4$ (x= 0.005, 0.01, 0.02 and 0.03) at fully discharged states. Prior to EIS tests, the half-cells were firstly cycled at 0.2C for 3 cycles, then discharged to 2 V at 0.1C and finally kept at open circuit for at least 6 h to reach the equilibrium states. As can be seen, all $Li_{1-4x}Ru_xFePO_4$ electrodes have smaller charge transfer resistances when compared to pristine $LiFePO_4$. This should be ascribed to the largely enhanced electronic conductivity after the RuO_2 trace doping. The charge transfer resistance of pristine $LiFePO_4$ electrode is 0.17 Ω·g, while the charge transfer resistance of $Li_{0.98}Ru_{0.005}FePO_4$ electrode is only 0.08 Ω·g. With the highest electronic conductivity, $Li_{0.92}Ru_{0.02}FePO_4$ electrode has the lowest charge transfer resistance of only 0.035 Ω·g. The charge transfer resistance in $Li_{1-4x}Ru_xFePO_4$ electrodes generally decreases with

increasing electronic conductivity of the active material. The only exception is $Li_{0.88}Ru_{0.03}FePO_4$ that has the highest charge transfer resistance among all $Li_{1-4x}Ru_xFePO_4$ electrodes. The large electrochemical charge transfer resistance of $Li_{0.88}Ru_{0.03}FePO_4$ may be caused by the poor Li^+ penetration behavior of the surface impurities. Although the bulk electronic conductivity of $Li_{0.88}Ru_{0.03}FePO_4$ is relatively high, the surface impurities probably impede the Li^+ extraction and insertion on the surface, resulting in relatively higher charge transfer resistance. This finding is also in line with potential hysteresis analysis in the CV spectra.

3.2.3.3 Specific capacity

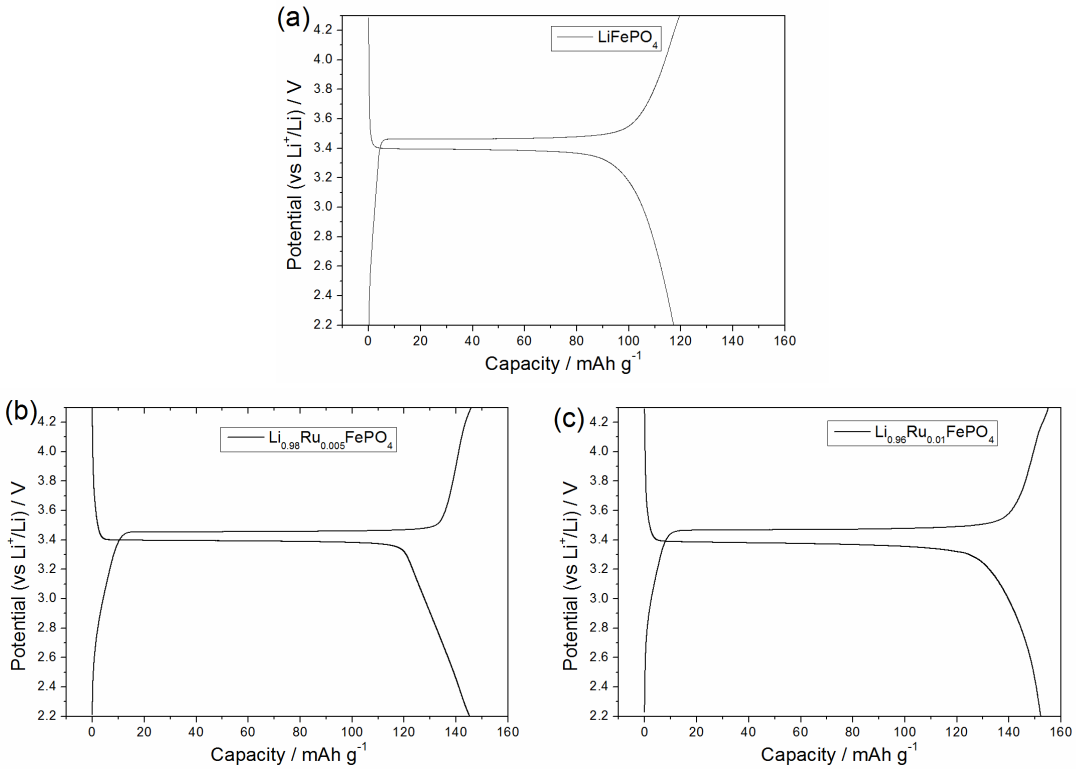

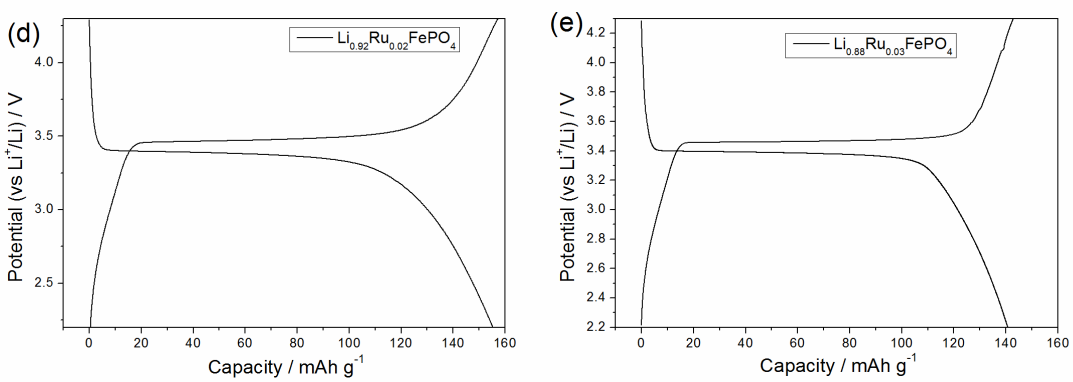

Fig. 3.9 Charge-discharge curves of pristine $LiFePO_4$ and $Li_{1-4x}Ru_xFePO_4$ at 0.1C (a) pristine $LiFePO_4$, (b) x=0.005, (c) x=0.01, (d) x=0.02 and (e) x=0.03.

Before the comparison of specific capacity of pristine $LiFePO_4$, it should be noted that the theoretical specific capacity of $Li_{1-4x}Ru_xFePO_4$ decreases with increasing x and consequently reducing initial Li^+ content in the lattice. The theoretical specific capacity of $Li_{1-4x}Ru_xFePO_4$ can be calculated from following equation:

$$Q = \frac{q_e \cdot N_A \cdot (1-4x)}{M_w} \qquad \text{Equation 3.1}$$

where q_e is the electron charge, N_A is Avogadro constant, x is the designed Ru^{4+} dopant level, and M_w is the molecular weight. For example, the theoretical capacity for $LiFePO_4$ is 170 mAh g^{-1}, while it reduces to 163 mAh g^{-1} for $Li_{0.96}Ru_{0.01}FePO_4$ and 156 mAh g^{-1} for $Li_{0.92}Ru_{0.02}FePO_4$.

Specific capacities of pristine $LiFePO_4$ and $Li_{1-4x}Ru_xFePO_4$ are shown in Fig. 3.9. As can be seen, all $Li_{1-4x}Ru_xFePO_4$ (x= 0.005, 0.01, 0.02 and 0.03) samples exhibit much higher specific capacities when compared to the pristine $LiFePO_4$. At a considerably low current density of 0.1C, the pristine $LiFePO_4$ can only deliver a capacity of 117 mAh g^{-1} due to the sluggish electronic conduction. In contrast, $Li_{0.96}Ru_{0.01}FePO_4$ and $Li_{0.92}Ru_{0.02}FePO_4$ have much higher specific capacities of 152

and 154 mAh g^{-1}, approaching the theoretical limits. With improved electronic conductivity, more Li^+ in the lattice can be reversibly removed from $Li_{1-4x}Ru_xFePO_4$ in the electrochemical reaction.

3.2.3.4 Discharge rate capability

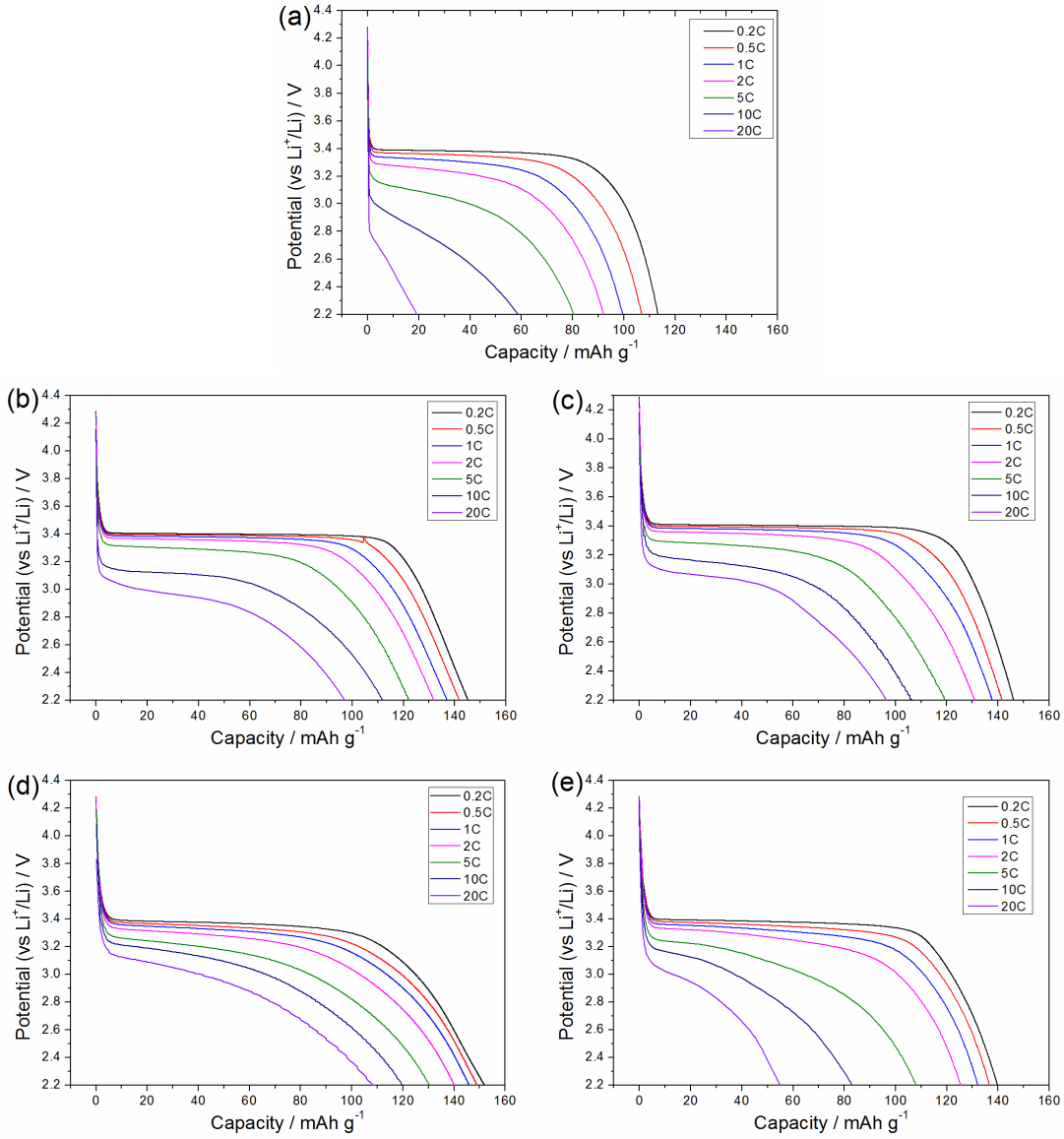

Fig. 3.10 Discharge rate capabilities of $LiFePO_4$ and $Li_{1-4x}Ru_xFePO_4$; (a) pristine $LiFePO_4$, (b) x=0.005 and (c) x=0.01.

Fig. 3.10 shows discharge rate capabilities of pristine $LiFePO_4$ and $Li_{1-4x}Ru_xFePO_4$.

As can be seen, insulating pristine $LiFePO_4$ shows very poor high rate performances even at low current densities. Pristine $LiFePO_4$ delivers only 117 mAh g^{-1} at 0.2C and 58 mAh g^{-1} at 10C. On the contrary, $Li_{0.96}Ru_{0.01}FePO_4$ and $Li_{0.92}Ru_{0.02}FePO_4$ can still deliver capacities of 105 mAh g^{-1} and 120 mAh g^{-1} at 10C, respectively. $Li_{1-4x}Ru_xFePO_4$ has a notably improved discharge rate capability especially at high current densities of 10C and 20C. The reduced polarization and electrode resistance as described in Sections 3.2.3.1 and 3.2.3.2 should be the main reason for this improvement. As a consequence of pronounced impurities, $Li_{0.88}Ru_{0.03}FePO_4$ shows relatively worse rate capability when compared to other $Li_{1-4x}Ru_xFePO_4$ (x = 0.005, 0.01 and 0.02) materials. $Li_{0.88}Ru_{0.03}FePO_4$ can deliver a capacity of only 82 mAh g^{-1} at 10C.

3.2.3.5 Fast charge capability

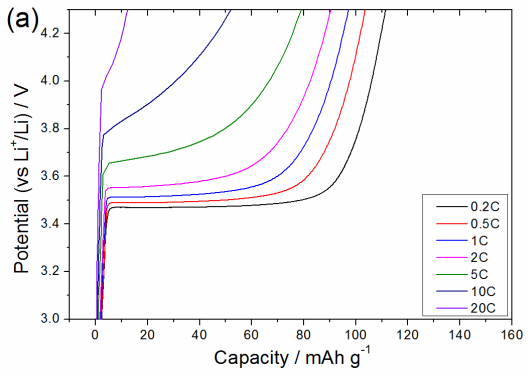

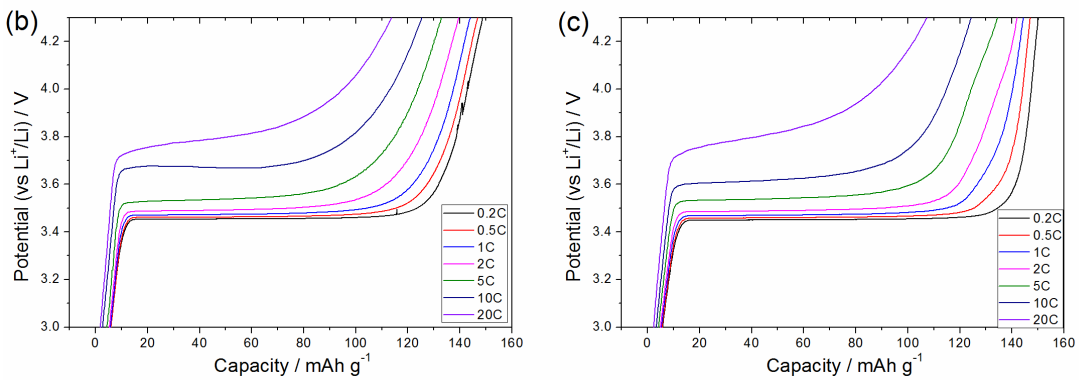

Fig. 3.11 Fast charge capabilities of $LiFePO_4$ and $Li_{1-4x}Ru_xFePO_4$; (a) pristine $LiFePO_4$, (b) x=0.005, and (c) x=0.01

In addition to the high power output demonstrated above, $Li_{1-4x}Ru_xFePO_4$ materials also exhibit impressive fast charge capabilities, as shown in Fig. 3.11. Upon fast charge at 10C, only 56 mAh g^{-1} can be charged for pristine $LiFePO_4$, whereas more than 120 mAh g^{-1}, or ~80% of the specific capacity at 0.2C, can be charged for $Li_{0.98}Ru_{0.005}FePO_4$ and $Li_{0.96}Ru_{0.01}FePO_4$. The half-cell of $Li_{1-4x}Ru_xFePO_4$ can be charged to 80% of its full capacity in merely 5 min. This fast charge feature of $Li_{1-4x}Ru_xFePO_4$ is able to fulfill the urgent needs in EV/HEVs.

3.2.3.6 Cycleability

The charge-discharge cyclic performances of the pristine $LiFePO_4$ and $Li_{1-4x}Ru_xFePO_4$ (x = 0.005 and 0.01) are shown in Fig. 3.12. As can be seen, $Li_{1-4x}Ru_xFePO_4$ materials exhibit excellent capacity retention at various current densities from 1C to 20C, while pristine $LiFePO_4$ has shown noticeable capacity fading in the first 10 cycles at 1C and 10C. The cyclic performances of the pristine $LiFePO_4$ and $Li_{0.96}Ru_{0.01}FePO_4$ were further challenged in the long-term tests of 1000 cycles, as shown in Fig. 3.12 (b). Pristine $LiFePO_4$ can only deliver 32 mAh g^{-1} in the first cycle,

while only 14 mAh g^{-1} can be retained after 1000 cycles. On the other hand, $Li_{0.96}Ru_{0.01}FePO_4$ can discharge a capacity of 89 mAh g^{-1} in the first cycle, while 84 mAh g^{-1} capacity can still be retained after 1000 cycles. The capacity loss of $Li_{0.96}Ru_{0.01}FePO_4$ after 1000 cycles is as low as 5.6%. This long-term cyclic test demonstrates good lattice stability of $Li_{1-4x}Ru_xFePO_4$ at high current densities and repeated cycles. This excellent long-term cyclic performance exceeds the common 500-cycle requirement in LIB industries.

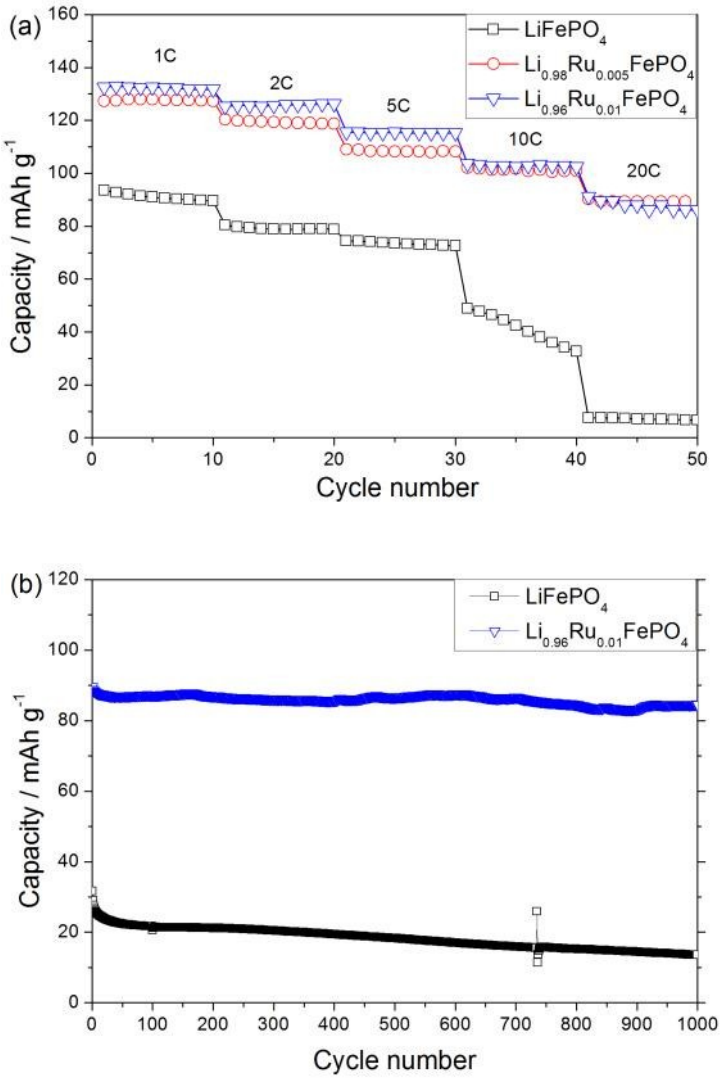

Fig. 3.12 Cyclic performances of $Li_{1-4x}Ru_xFePO_4$; (a) at various current densities from 1C to 20C, and (b) long-term cyclic performances at 20C

3.3 Ru^{4+} doping on M1 site of $LiMnPO_4$

In recent years, $LiMnPO_4$ is attracting attention owing to its higher potential at ~4 V. However, the extremely poor electronic conductivity and Jahn-Teller lattice distortion make it barely possible to extract lithium ions from $LiMnPO_4$ at a reasonable rate. Given the success of Ru^{4+} trace doping on isomorph $LiFePO_4$, the effects of RuO_2 trace doping on the electrochemical performances of $LiMnPO_4$ were explored in this Section 3.3.

3.3.1 Characterization

Fig. 3.13 shows the XRD spectra of pristine $LiMnPO_4$ and $Li_{0.96}Ru_{0.01}MnPO_4$. As can be seen, pristine $LiMnPO_4$ shows a single phase ordered olivine structure similar to $LiFePO_4$, with lattice parameters of a = 10.450 Å, b = 6.106 Å, c = 4.746 Å and cell volume of 302.9 $Å^3$. However, notable reflections from RuO_2 and $Mn_2P_2O_7$ can be observed from the XRD spectrum of $Li_{0.96}Ru_{0.01}MnPO_4$, suggesting that the $LiMnPO_4$ lattice is not able to accommodate Ru^{4+} at all under the present processing conditions. The initial cell volume of $LiMnPO_4$ (302.9 $Å^3$) is considerably larger than that of $LiFePO_4$ (291.2 $Å^3$), therefore Ru^{4+} with relatively smaller radii (0.62 Å) than the host Li^+ (0.78 Å) may have a lower solubility in $LiMnPO_4$. The lattice deformation of the $LiMnPO_4$ lattice described in Chapter 1 is also a possible reason for this phenomenon.

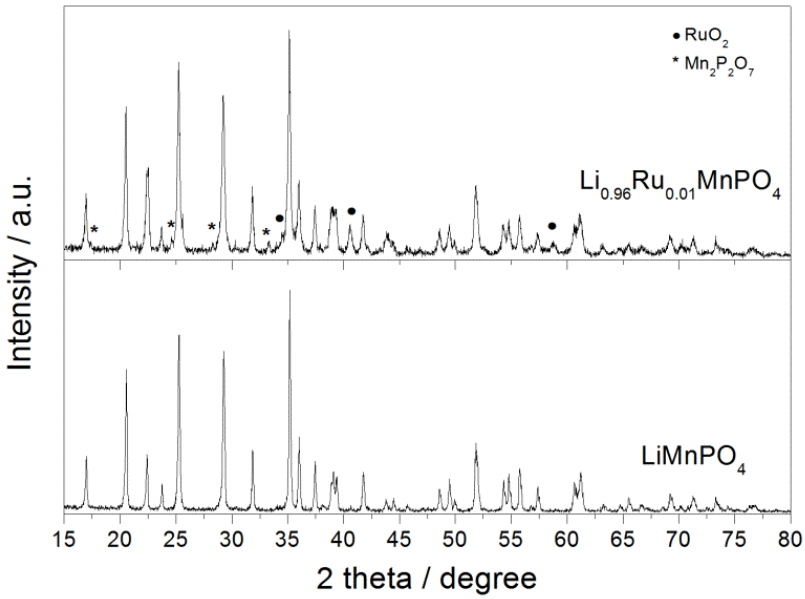

Fig. 3.13 XRD spectra of $LiMnPO_4$ and $Li_{0.96}Ru_{0.01}MnPO_4$

3.3.2 Electrochemical properties

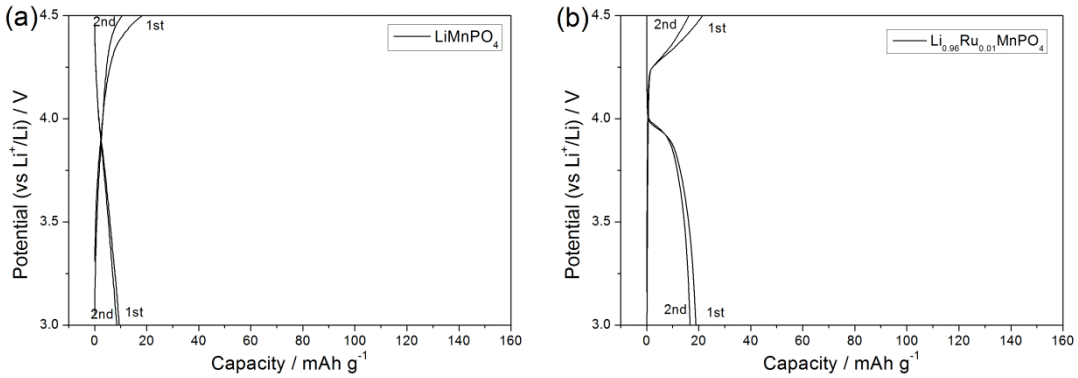

Fig. 3.14 Charge-discharge curves of (a) $LiMnPO_4$ and (b) $Li_{0.96}Ru_{0.01}MnPO_4$ at 0.1C

Fig. 3.14 shows the charge-discharge curves of $LiMnPO_4$ and $Li_{0.96}Ru_{0.01}MnPO_4$ at a low current density of 0.1C (16 mA g^{-1}). Both $LiMnPO_4$ and $Li_{0.96}Ru_{0.01}MnPO_4$ show extremely poor electrochemical activity and very low specific capacity. Similar to the previous reports [43], little amount of Li^+ can be extracted from the lattice of pristine $LiMnPO_4$. The specific capacity of pristine $LiMnPO_4$ is less than 10 mAh g^{-1},

corresponding to merely 5% of the Li^+ in the lattice. $Li_{0.96}Ru_{0.01}MnPO_4$ has a slightly higher capacity of about 19 mAh g^{-1}, which may be benefited from the residual conductive RuO_2. In addition to the poor specific capacity, the first cycle columbic efficiencies of the two materials are both very low, implying a relatively strong side reaction between $LiMnPO_4$ and the electrolyte. Similar to spinel $LiMn_2O_4$, Mn^{3+} in lithiated $LiMnPO_4$ may react with electrolyte and gradually dissolves at high potential [150].

3.4 Ru^{4+} doping on M1 site of $LiCoPO_4$

Ru^{4+} trace doping on olivine $LiCoPO_4$ has been studied in this Section 3.4. Olivine $LiCoPO_4$ has a high operation potential of 4.9 V vs. Li^+/Li, more than 40% higher than that of $LiFePO_4$. However, its potential (4.9 V) exceeds the anodic limit of most of the developed electrolytes. Nevertheless, the high operation potential may be desirable for high power and energy density LIBs in the future after development of electrolyte system.

3.4.1 Characterization

Fig. 3.15 shows the XRD spectra of $Li_{0.96}Ru_{0.01}CoPO_4$ and $LiCoPO_4$. $LiCoPO_4$ has lattice parameters of a = 10.204 Å, b = 5.922 Å, c = 4.700 Å and cell volume of 284.0 $Å^3$. As the cell volume is smaller than that of $LiFePO_4$ (291.2 $Å^3$), Ru^{4+} trace doping is supposed to be feasible in $LiCoPO_4$ in contrast to the case of $LiMnPO_4$. As expected, no impurity phases can be found from the XRD pattern of $Li_{0.96}Ru_{0.01}CoPO_4$,

indicating that the $LiCoPO_4$ lattice seems to be able to accommodate at least 1 mol% of Ru^{4+}.

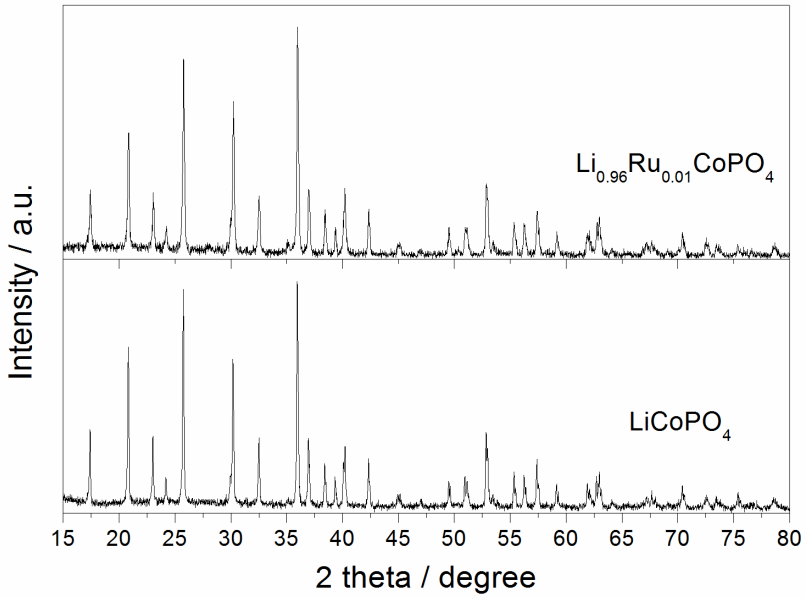

Fig. 3.15 XRD spectra of $LiCoPO_4$ and $Li_{0.96}Ru_{0.01}CoPO_4$

Fig. 3.16 shows the Cole-Cole plots of AC impedance spectra of $LiCoPO_4$ and $Li_{0.96}Ru_{0.01}CoPO_4$ measured at room temperature. The electrical conductivity of $LiCoPO_4$ is about 2×10^{-10} S cm^{-1}, 2 orders lower than that (1.5×10^{-8} S cm^{-1}, this work) of $LiFePO_4$. $Li_{0.96}Ru_{0.01}CoPO_4$ has an apparently improved electrical conductivity of about 1×10^{-7} S cm^{-1}, 3 orders higher than that of pristine $LiCoPO_4$. However, the absolute value of the electrical conductivity of $Li_{0.96}Ru_{0.01}CoPO_4$ is still 3-4 orders lower than that of $Li_{1-4x}Ru_xFePO_4$.

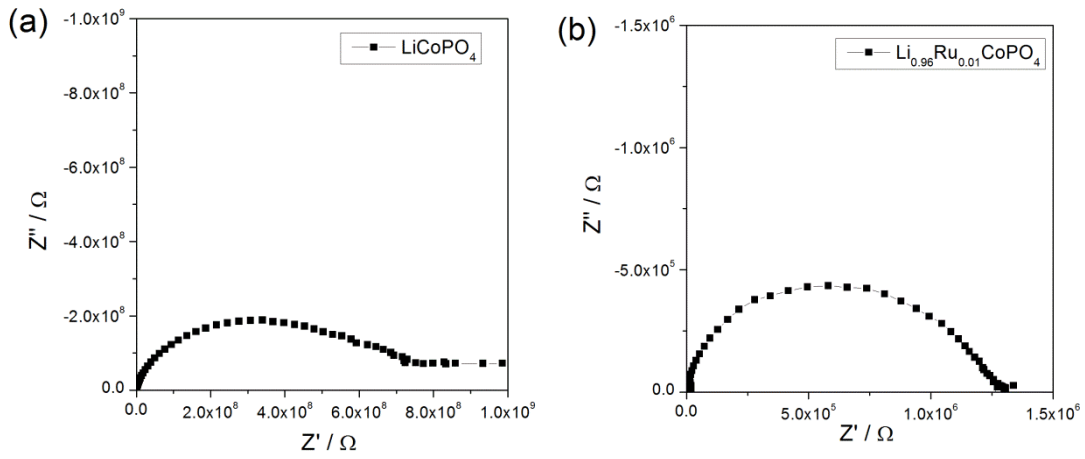

Fig. 3.16 AC impedance spectra of $LiCoPO_4$ and $Li_{0.96}Ru_{0.01}CoPO_4$ pellets

3.4.2 Electrochemical properties

Fig. 3.17 shows charge-discharge curves of $LiCoPO_4$ and $Li_{0.96}Ru_{0.01}CoPO_4$ cycled at a low current density of 0.1C (16 mA g^{-1}). As can be seen, the specific capacity of $Li_{0.96}Ru_{0.01}CoPO_4$ is c larger than that of $LiCoPO_4$ due to the improved electrical conductivity. Nevertheless, $Li_{0.96}Ru_{0.01}CoPO_4$ can only deliver a specific capacity of 38 mAh g^{-1} with a considerably large irreversible capacity loss in the first cycle. The first cycle columbic efficiencies of $LiCoPO_4$ and $Li_{0.96}Ru_{0.01}CoPO_4$ are only 28% and 25% respectively. Moreover, the capacities also decline rapidly in the second cycle. The high operation potential of $LiCoPO_4$ and high reactivity of Co^{3+} induce severe electrolyte degradation, resulting in the large irrepressible pseudo charge capacity and the rapid capacity fading. Since the potential of $LiCoPO_4$ (about 4.9 V vs. Li^+/Li) is far beyond the anodic limit of current electrolyte (~4.5 V) [30], severe electrolyte degradation is unavoidable even at room temperature. Hence, the feasibility of $LiCoPO_4$ in practical applications strongly depends on a breakthrough in current

organic electrolyte, while surface modification may be another choice to ease the electrolyte degradation.

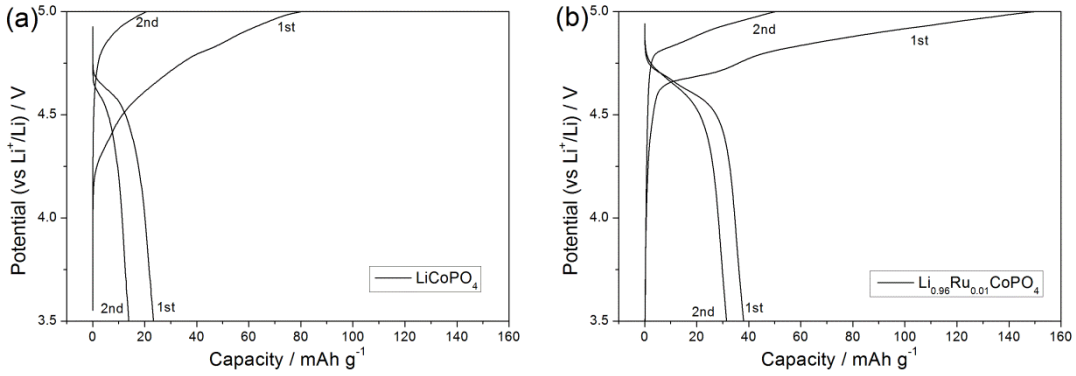

Fig. 3.17 Charge-discharge curves of (a) $LiCoPO_4$ and (b) $Li_{0.96}Ru_{0.01}CoPO_4$ at 0.1C

3.5 Summary

In summary, $LiMPO_4$ (M = Fe, Mn and Co) doped with trace amount of RuO_2 has been successfully prepared via solid-state reaction. The effects of RuO_2 trace doping on crystal structure, conductivity and electrochemical properties were systemically investigated. The solubility of Ru dopant on M1 (Li) site of $LiFePO_4$ is probably limited to 2 mol% based on XRD analysis. RuO_2 trace doping can dramatically raise the electronic conductivity by 4-6 orders over the pristine $LiFePO_4$. As a result, a nearly full utilization of theoretical capacity can be achieved for $Li_{1-4x}Ru_xFePO_4$ (x = 0.005, 0.01 and 0.02). Electronically conductive $Li_{1-4x}Ru_xFePO_4$ (x = 0.005, 0.01 and 0.02) exhibits impressive high power performance and good fast charge capability. Excellent long-term cyclic performances for over 1000 cycles at high current densities of 20C (3200 mA g^{-1}) have also been demonstrated with $Li_{0.96}Ru_{0.01}FePO_4$. The trace doping

technique appears to be suitable for high power and energy densities LIBs in the aspect of electrochemical properties. The only unfavorable factor may be the limited availability of RuO_2, which may lead to 10-20% increase in the cost of raw materials. Even though the trace doping technique requires very small amount of expensive RuO_2 dopant, it is still urgent to develop a low cost modification techniques for $LiFePO_4$.

The current work also found that RuO_2 trace doping can barely improve the electrochemical performances of $LiMnPO_4$ and $LiCoPO_4$ with the same olivine structure. The XRD analysis suggests that $LiMnPO_4$ seems not able to accommodate Ru^{4+} at all. On the other hand, although Ru^{4+} can be doped within the lattice of $LiCoPO_4$ and the electrical conductivity can be increased by 3 orders after Ru^{4+} doping, the absolute value of the electrical conductivity ($\sim 10^{-7}$ S cm^{-1}) of $Li_{0.96}Ru_{0.01}CoPO_4$ is still too low. Moreover, the high reactivity between the high potential $LiMnPO_4$ and $LiCoPO_4$ electrodes and electrolyte also induces serious electrolyte degradation and large irreversible capacity. Consequently, all the pristine and Ru^{4+} doped $LiMnPO_4$ and $LiCoPO_4$ exhibit extremely low specific capacity and poor reversibility even at very low current density. To overcome this problem, surface modification may be a possible solution to reduce the direct contact between active material and the electrolyte.

4 Mn^{2+} substitution on M2 site: solid solution of olivine $LiFe_{1-x}Mn_xPO_4$

As described in Chapter 1, a notable intrinsic drawback of $LiFePO_4$ is the low potential (3.4V vs. Li^+/Li) when compared to oxide cathode materials, for example $LiCoO_2$ (>3.7 V) and $LiMn_2O_4$ (~4.0 V). On the other hand, olivine $LiMnPO_4$ does have a favorable high potential of 4.1 V, however, lithium extraction from $LiMnPO_4$ has been proven to be extremely difficult due to extremely poor electronic/ionic conductivities and anisotropic Jahn-Teller lattice distortion [43, 45, 48, 49]. Although some notable achievements on $LiMnPO_4$ have been made recently through nanosizing and/or intensive carbon coating [50-58], the rate capability and cycleability still cannot meet the requirements of practical application at this moment. The solid-solution $LiFe_{1-x}Mn_xPO_4$ ($0 \leq x \leq 1$) was investigated in this chapter with M2 site substitution.

Although RuO_2 trace doping can significantly improve the electronic transport and electrochemical performance of $LiFePO_4$, it has little effects on $LiMnPO_4$. In fact, there are also no reports on successful doping of other supervalent metal ions in $LiMnPO_4$ or $LiFe_{1-x}Mn_xPO_4$ so far. Conductive coating technology has been developed to overcome the poor electronic conductivity in this chapter. In addition, the surface coating may also protect the particle surface of $LiMnPO_4$ from HF etching. In addition, nano-sizing is also necessary to reduce stress-strain in bulk particle and to reduce the pathway of ionic and electronic transport.

4.1 Material preparation

A facile modified solid-state reaction, namely liquid polymer-assisted mechanical activation (PAMA), has been proposed for the first time in the synthesis of Mn based olivine materials. This method was firstly developed by Arrebola et al. to synthesize 80 nm $LiNi_{0.5}Mn_{1.5}O_4$ nanoparticles using polyethyleneglycol (PEG 400) as a "sacrificial template" [151]. However, in this work, the liquid polymer act not only as dispersion medium in mechanical activation, but also as *in-situ* sources of carbon coating. The long chains of liquid polymer can wrap and separate the nanoparticles from welding and clustering during the rigid mechanical activation, while their pyrolysis products can further restrict unfavorable grain growth and coarsening during calcination. This synthesis approach will be examined and characterized with carbon coated $LiFe_{0.25}Mn_{0.75}PO_4$ in Section 4.2. Then, the influences of Mn content on electrochemical properties of $LiFe_{1-x}Mn_xPO_4$ will be subsequently studied in Section 4.3 to explore the effects of Mn content and the optimized composition.

Considering the advantages of long polymer chain, polypropylene glycol (PPG 2000) was also adopted as the assistant agents in addition to the PEG 400 proposed by Arrebola et al.[151]. $LiFe_{1-x}Mn_xPO_4/C$ ($0 \leq x \leq 1$) composites were synthesized via a modified mechanical activation with assistance of liquid polymer. Stoichiometric amounts of LiAC (99%, Sigma-Aldrich), $Mn(AC)_2 \cdot 4H_2O$ (99%, Sigma-Aldrich), $FeC_2O_4 \cdot 2H_2O$ (99%, Sigma-Aldrich) and $NH_4H_2PO_4$ (99%, Arcos) were mechanical activated in the presence of 15 mL liquid polymer (PEG 400 or PPG 2000) at a speed

of 400 rpm for 2 h using planetary mill Retsch PM-100. The milled viscous slurry was directly calcinated at 600 ºC for 10 h in flowing argon. The as prepared $LiFe_{1-x}Mn_xPO_4/C$ ($0 \leq x \leq 1$) composites were denoted with the carbon source, for example, PPG-$LiFePO_4$. As a comparison, pristine $LiMn_{0.75}Fe_{0.25}PO_4$ was synthesized via a similar processing, except that the liquid polymer was replaced by the conventional ethanol.

4.2 $LiFe_{0.25}Mn_{0.75}PO_4/C$ synthesized via polymer-assisted mechanical activation

The effectiveness of the PAMA method in the synthesis of $LiMn_{1-x}Fe_xPO_4/C$ nanocomposite was evaluated first. It is believed that Mn has a much weaker catalytic activity for carbonization when compared to Fe [152], thus leading to poor carbon coating on $LiMnPO_4$ and Mn rich $LiMPO_4$. Therefore, this work started with Mn rich $LiMn_{0.75}Fe_{0.25}PO_4$ and the relatively active $LiFePO_4$ to examine the function of the liquid polymers as effective carbon sources.

4.2.1 Characterization

4.2.1.1 Crystal structure

As shown in Fig. 4.1, pristine $LiFe_{0.25}Mn_{0.75}PO_4$, PEG-$LiFe_{0.25}Mn_{0.75}PO_4$ and PPG-$LiFe_{0.25}Mn_{0.75}PO_4$ are all in ordered olivine structure of *Pnma* space group. The reflection peaks of all these $LiFe_{0.25}Mn_{0.75}PO_4$ materials shift notably to the small angle direction when compared to $LiFePO_4$, indicating solid-solution behavior of Fe^{2+} and

Mn^{2+} in the olivine lattice. The lattice parameters of the $LiMn_{0.75}Fe_{0.25}PO_4$ materials were calculated to be a = 10.428 Å, b = 6.082 Å and c = 4.733 Å, corresponding to a unit cell volume of 300.2 $Å^3$, in good agreement with previous reports [43].

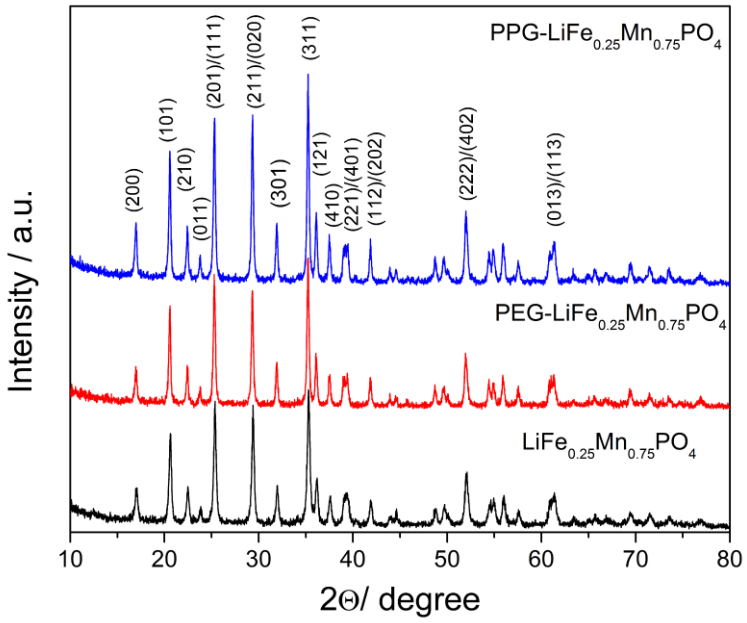

Fig. 4.1 XRD spectra of pristine $LiFe_{0.25}Mn_{0.75}PO_4$, PEG-$LiFe_{0.25}Mn_{0.75}PO_4$ and PPG-$LiFe_{0.25}Mn_{0.75}PO_4$

4.2.1.2 Micromorphology

Fig. 4.2 compares the micro-morphology and particle sizes of the $LiFe_{0.25}Mn_{0.75}PO_4$ materials synthesized with and without the assistance of liquid polymer. SEM observations show that PEG-$LiFe_{0.25}Mn_{0.75}PO_4$ and PPG-$LiFe_{0.25}Mn_{0.75}PO_4$ have notably smaller particle sizes when compared to the pristine $LiFe_{0.25}Mn_{0.75}PO_4$. For instance, PPG-$LiFe_{0.25}Mn_{0.75}PO_4$ has a uniform particle size of ~50 nm, while the pristine $LiMn_{0.75}Fe_{0.25}PO_4$ has an inhomogeneous particle size distribution of 50-300 nm with a mean particle size >100 nm. The TEM image

also clearly reveals the disperse particles of ~50 nm for the PPG-$LiFe_{0.25}Mn_{0.75}PO_4$, while the particles of PEG-$LiFe_{0.25}Mn_{0.75}PO_4$ appear to be more agglomerated.

As shown in Fig. 4.2 (e) and (g), the morphology of carbon coatings was further observed using high resolution TEM. Crystallized $LiFe_{0.25}Mn_{0.75}PO_4$ particles were well wrapped by uniform and thin carbon layer for both materials synthesized with assistance of polymer. The carbon layer is ~5 nm thick for PEG-$LiFe_{0.25}Mn_{0.75}PO_4$, whereas it is only 1-2 nm thick for PPG- $LiFe_{0.25}Mn_{0.75}PO_4$ with less carbon content.

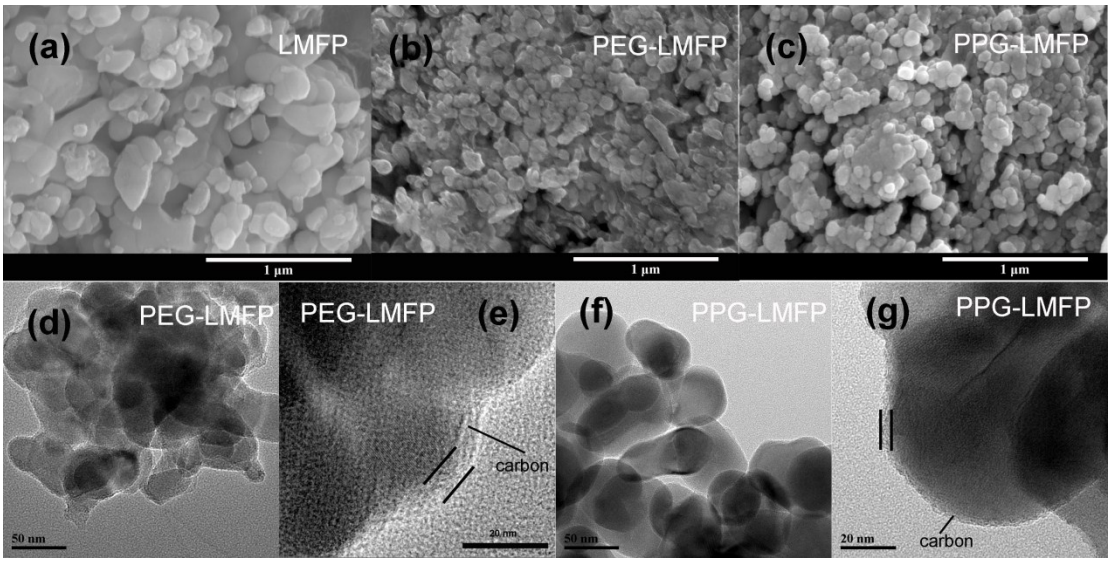

Fig. 4.2 SEM images of (a) pristine $LiFe_{0.25}Mn_{0.75}PO_4$ (b) PEG- $LiFe_{0.25}Mn_{0.75}PO_4$ (c) PPG-$LiFe_{0.25}Mn_{0.75}PO_4$; TEM images of (d) and (e) PEG-$LiFe_{0.25}Mn_{0.75}PO_4$, (f) and (g) PPG-$LiFe_{0.25}Mn_{0.75}PO_4$

4.2.1.3 Raman spectroscopy

Residual carbon in PEG-$LiFe_{0.25}Mn_{0.75}PO_4$ and PPG-$LiFe_{0.25}Mn_{0.75}PO_4$ should exist in amorphous form, thus no carbon phases can be identified from the XRD spectra. Carbon contents in these materials synthesized via PAMA were determined using TGA. Residual carbon content resulted from PEG was estimated to be 5.9 wt%

for PEG-$LiFe_{0.25}Mn_{0.75}PO_4$, while residual carbon content resulted from PPG was estimated to be 1.8 wt% for PPG-$LiFe_{0.25}Mn_{0.75}PO_4$. Even though the starting amounts of PEG and PPG were almost the same, PEG apparently produced more carbon upon pyrolysis than PPG did. As a comparison, the carbon content in the sucrose-$LiFePO_4$ is about 4.6 wt%.

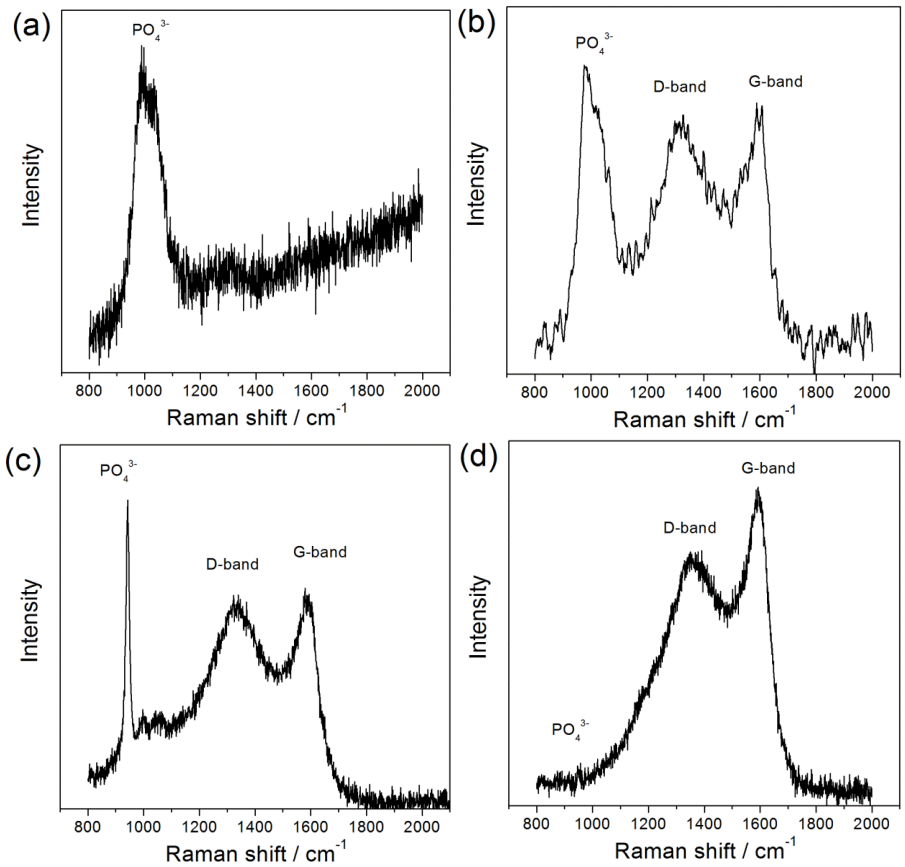

Fig. 4.3 Raman spectra of carbon resulted from different carbon sources; (a) bare (b) sucrose (c) PEG and (d) PPG

Fig. 4.3 shows the Raman spectra of carbon coating resulted from different carbon sources. The peaks over the range of 900 -1100 cm^{-1} should be attributed to the intermolecular stretching of PO_4^{3-}. Two peaks over the range of 1200-1800 cm^{-1} are attributed to carbon layers. The peak at around 1360 cm^{-1}, namely D-band, is attributed

to the sp^3 disordered carbon, while the other peak at around 1680 cm^{-1}, namely G-band, is attributed to the sp^2 graphite carbon. Bared $LiFePO_4$ exhibits no signal of D-band or G-band in the Raman spectrum, indicating almost no residual carbon. Both D-band and G-band can be found in Raman spectra of all the carbon-coated materials, confirming that all the carbon coatings are in amorphous form. As described in Chapter 2, the peak intensity ratio of I_D/I_G implies the graphitic level of amorphous carbon. As shown in previous reports, the lower ratio of I_D/I_G normally indicates the higher graphitic level and therefore the higher electrical conductivity [50, 153]. Ratios of I_D/I_G of carbon resulted from sucrose, PEG and PPG are 0.94, 0.96 and 0.79, respectively. Carbon resulted from PPG has the lowest I_D/I_G ratio, which may give the highest electronic conductivity [154]. Moreover, the peaks of PO_4^{3-} of PPG-$LiFe_{0.25}Mn_{0.75}PO_4$ are barely detectable compared to other materials. This suggests that the carbon coating PPG-$LiFe_{0.25}Mn_{0.75}PO_4$ is uniform to resist laser penetration in the Raman spectroscopy tests.

4.2.2 Electrochemical properties

4.2.2.1 Cyclic voltammetry

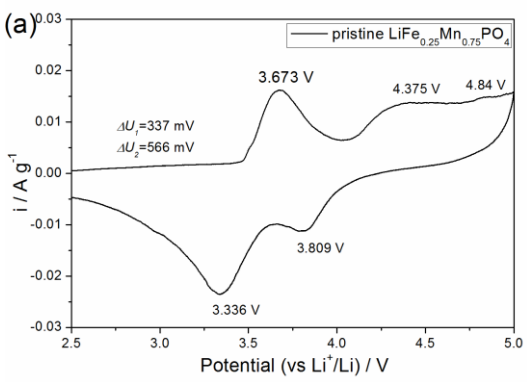

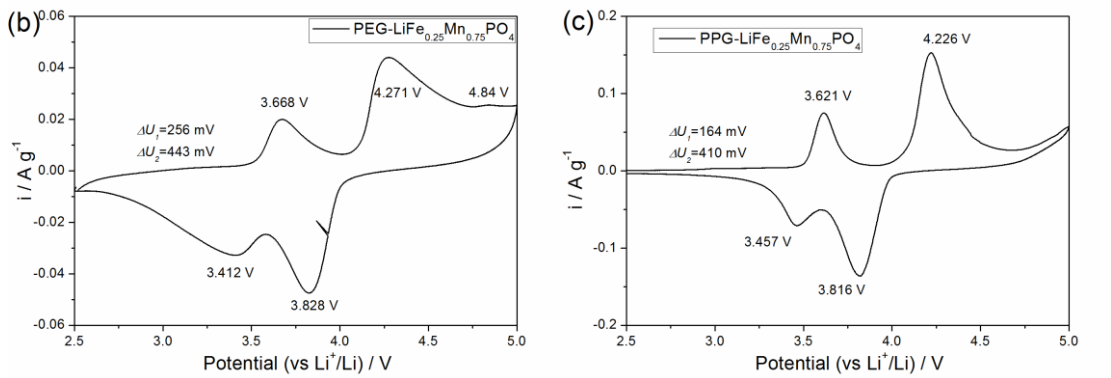

Fig. 4.4 Cyclic voltammetry of (a) $LiFe_{0.25}Mn_{0.75}PO_4$, (b) PEG-$LiFe_{0.25}Mn_{0.75}PO_4$ and (c) PPG-$LiFe_{0.25}Mn_{0.75}PO_4$

CV measurements were carried out to examine the redox couple of Mn^{2+}/Mn^{3+} and Fe^{2+}/Fe^{3+}. Fig. 4.4 shows CV profiles of pristine $LiFe_{0.25}Mn_{0.75}PO_4$, PEG-$LiFe_{0.25}Mn_{0.75}PO_4$ and PPG-$LiFe_{0.25}Mn_{0.75}PO_4$. The Fe^{2+}/Fe^{3+} redox is located at ~3.5 V, while Mn^{2+}/Mn^{3+} redox is located at ~4.0 V. The CV curve of pristine $LiFe_{0.25}Mn_{0.75}PO_4$ indicates a relatively lower peak current of Mn^{2+}/Mn^{3+} redox when compared to that of Fe^{2+}/Fe^{3+} redox, even though the Mn content triples Fe content. This suggests that most of the Mn in pristine $LiFe_{0.25}Mn_{0.75}PO_4$ has not been activated due to the poor electronic/ionic conductivity and relatively larger particle size. The peak currents of Mn^{2+}/Mn^{3+} redox couple of both PEG-$LiFe_{0.25}Mn_{0.75}PO_4$ and PPG-$LiFe_{0.25}Mn_{0.75}PO_4$ are much stronger than that of $LiFe_{0.25}Mn_{0.75}PO_4$. For instance, the peak current of anodic reaction of $Mn^{2+} \rightarrow Mn^{3+}$ is only 0.014 A g^{-1} for pristine $LiFe_{0.25}Mn_{0.75}PO_4$ in comparison of 0.15 A g^{-1} for PPG-$LiFe_{0.25}Mn_{0.75}PO_4$.

The potential hystereses of Mn^{2+}/Mn^{3+} redox and Fe^{2+}/Fe^{3+} redox of pristine $LiFe_{0.25}Mn_{0.75}PO_4$ are 556 mV and 337 mV, respectively. It can be found that the potential hysteresis of Fe^{2+}/Fe^{3+} redox of pristine $LiFe_{0.25}Mn_{0.75}PO_4$ is 44 mV larger

than that of pristine $LiFePO_4$ (Chapter 3). This increased polarization should be caused by the influences of the inactive Mn^{2+}/Mn^{3+}. Owing to the uniform carbon coating and small particle size from PMMA synthesis, the polarization of Mn^{2+}/Mn^{3+} redox has been significantly reduced to 443 mV for PEG-$LiFe_{0.25}Mn_{0.75}PO_4$ and 410 mV for PPG-$LiFe_{0.25}Mn_{0.75}PO_4$, while the polarization of Fe^{2+}/Fe^{3+} redox has been reduced to 256 mV for PEG-$LiFe_{0.25}Mn_{0.75}PO_4$ and 164 mV for PPG-$LiFe_{0.25}Mn_{0.75}PO_4$. Although the carbon content in PPG-$LiFe_{0.25}Mn_{0.75}PO_4$ is considerably lower than that in PEG-$LiFe_{0.25}Mn_{0.75}PO_4$, PPG-$LiFe_{0.25}Mn_{0.75}PO_4$ electrode still shows considerable smaller polarizations for both Fe^{2+}/Fe^{3+} and Mn^{2+}/Mn^{3+} redox couples. As indicated in Raman spectra, the carbon coating resulted from PPG has a higher graphitic level and a lower degree of sp^3 disorder, benefiting the electronic conduction in PPG-$LiFe_{0.25}Mn_{0.75}PO_4$ electrode.

4.2.2.2 Specific capacity

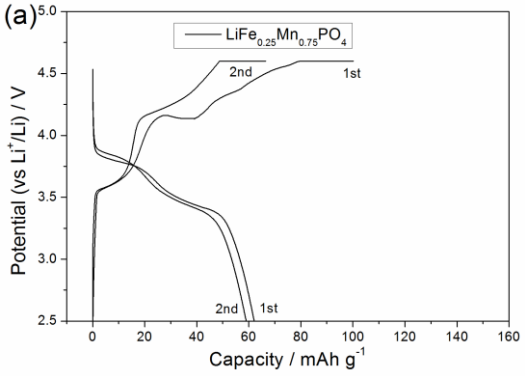

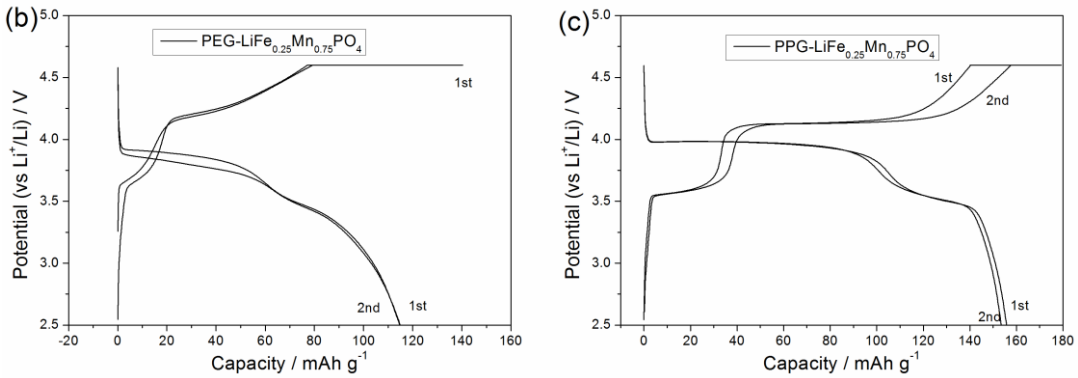

Fig. 4.5 Charge-discharge curves of (a) $LiFe_{0.25}Mn_{0.75}PO_4$, (b) PEG-$LiFe_{0.25}Mn_{0.75}PO_4$ and (c) PPG-$LiFe_{0.25}Mn_{0.75}PO_4$

Fig. 4.5 shows the charge-discharge curves of pristine and PAMA synthesized $LiFe_{0.25}Mn_{0.75}PO_4$ at a low current density of 0.1C. Due to the poor electrochemical activity of Mn^{2+}/Mn^{3+}, the half-cells were then further charged at a constant voltage mode until that current fell below 0.02C. As can be seen, PEG-$LiFe_{0.25}Mn_{0.75}PO_4$ and PPG-$LiFe_{0.25}Mn_{0.75}PO_4$ have significantly higher specific capacities than that of pristine $LiFe_{0.25}Mn_{0.75}PO_4$. Although pristine $LiFe_{0.25}Mn_{0.75}PO_4$ has a much higher specific capacity when compared to pristine $LiMnPO_4$ (Chapter 3), the absolute value (62 mAh g^{-1}) is still very low. Moreover, the capacity loss and abnormal voltage plateau in the first charge cycle indicate a strong passivation process between electrode and electrolyte, resulting in a low coulombic efficiency of only 61%. With efficient carbon coating, the specific capacities of PEG-$LiFe_{0.25}Mn_{0.75}PO_4$ and PPG-$LiFe_{0.25}Mn_{0.75}PO_4$ are remarkably increased to 117 mAh g^{-1} and 154 mAh g^{-1}, respectively. The first cycle coulombic efficiencies of the PEG-$LiFe_{0.25}Mn_{0.75}PO_4$ and PPG-$LiFe_{0.25}Mn_{0.75}PO_4$ are 82% and 87% respectively, much higher than that of the pristine $LiFe_{0.25}Mn_{0.75}PO_4$ (61%). The electrolyte degradation is also significantly

alleviated due to the protection layer of carbon.

4.2.2.3 Rate capability

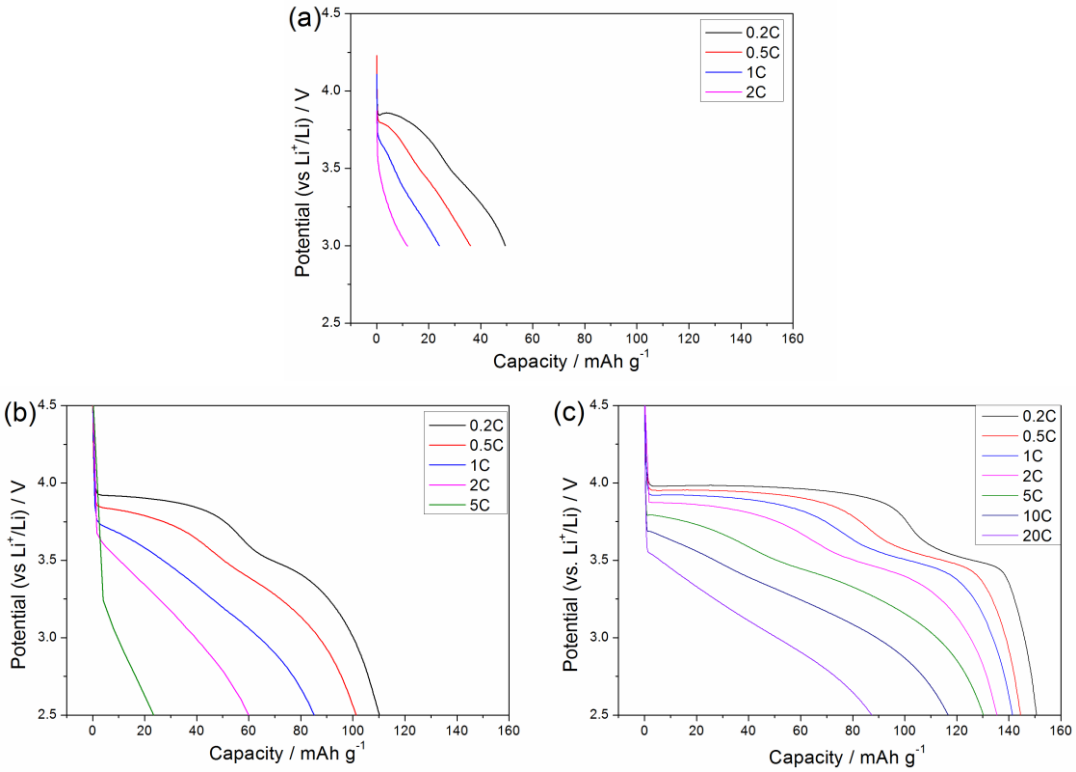

Fig. 4.6 Discharge rate capabilities of (a) $LiFe_{0.25}Mn_{0.75}PO_4$, (b) PEG-$LiFe_{0.25}Mn_{0.75}PO_4$ and (c) PPG-$LiFe_{0.25}Mn_{0.75}PO_4$

Fig. 4.6 compares discharge rate capabilities of pristine $LiMn_{0.75}Fe_{0.25}PO_4$, PEG-$LiMn_{0.75}Fe_{0.25}PO_4$ and PPG-$LiMn_{0.75}Fe_{0.25}PO_4$. As expected, pristine $LiMn_{0.75}Fe_{0.25}PO_4$ shows an extremely poor discharge rate capability. Only 49% of the specific capacity can be retained at 1C for pristine $LiMn_{0.75}Fe_{0.25}PO_4$. On the other hand, PPG-$LiMn_{0.75}Fe_{0.25}PO_4$ can deliver a high capacity of 141 mAh g^{-1} at 1C, corresponding to 94% of the specific capacity. At high current rates, discharge capacities of PPG-$LiMn_{0.75}Fe_{0.25}PO_4$ can still reach 117 mAh g^{-1} at 10C and 87 mAh g^{-1} at 20C. Such a good rate capability outstands previous reports [60, 61, 64-66] for

Mn rich $LiFe_{1-x}Mn_xPO_4$ compositions with only 2 wt% of residual carbon. Moreover, the simple and facile synthesis route of PAMA also exhibit crucial advantages in mass production over the other synthetic routes [62].

It is interesting to note that PPG-$LiMn_{0.75}Fe_{0.25}PO_4$ with less residual carbon shows a notably larger specific capacity and better discharge rate capability over PEG-$LiMn_{0.75}Fe_{0.25}PO_4$. This may be caused by two reasons. Firstly, the carbon coating resulted from PPG has a higher graphitic level and a lower degree of sp^3 disorder, leading to a better electronic conduction. Secondly, the thinner carbon layer and the milder particle agglomeration of PPG-$LiMn_{0.75}Fe_{0.25}PO_4$ are friendlier to electrolyte infiltration.

4.2.2.4 Cycleability

Fig. 4.7 compares the cyclic performances of $LiFe_{0.25}Mn_{0.75}PO_4$, PEG-$LiFe_{0.25}Mn_{0.75}PO_4$ and PPG-$LiFe_{0.25}Mn_{0.75}PO_4$. PPG-$LiFe_{0.25}Mn_{0.75}PO_4$ was cycled at 10C with constant voltage charge for 5 min in each cycle, whereas pristine $LiFe_{0.25}Mn_{0.75}PO_4$ and PEG-$LiFe_{0.25}Mn_{0.75}PO_4$ were cycled at 1C with constant voltage charge for 30 min, since they cannot deliver reasonable capacity at 10C. Nevertheless, PPG-$LiFe_{0.25}Mn_{0.75}PO_4$ still has a much higher initial capacity at 10C than the pristine $LiFe_{0.25}Mn_{0.75}PO_4$ and PEG-$LiFe_{0.25}Mn_{0.75}PO_4$ at 1C. Moreover, the PPG-$LiFe_{0.25}Mn_{0.75}PO_4$ also exhibits a better cycleability. Due to the high reactivity of Mn^{3+} with electrolyte at high potential, only about 20% and 50% of the maximum capacity can be retained after 500 cycles for PEG-$LiFe_{0.25}Mn_{0.75}PO_4$ and pristine

$LiFe_{0.25}Mn_{0.75}PO_4$. On the other hand, 73% of the maximum capacity can be retained after 500 cycles for PPG-$LiFe_{0.25}Mn_{0.75}PO_4$, which surpass the cycleability of similar materials reported in literature [64, 66]. It is clear that the uniform carbon coating of PPG-$LiFe_{0.25}Mn_{0.75}PO_4$ can effectively protect the particle surface from electrolyte degradation. Even though, carbon coated $LiFe_{0.25}Mn_{0.75}PO_4$ still shows much pronounced capacity fading when compared to $LiFePO_4$. The effects of the Mn content x on the cyclability of $LiFe_{1-x}Mn_xPO_4$ will be further characterized in Section 4.3.

The cause of the inferior cycleability of PEG-$LiFe_{0.25}Mn_{0.75}PO_4$ may be the highly sp^3 disordered carbon resulted from PEG. Highly sp^3 disordered pyrolysis carbon often contain large amount of hydrogen bond from its organic precursor. These hydrogen atoms may react with the electrolyte and may produce acidic HF, which may severely damage the durability of the cell.

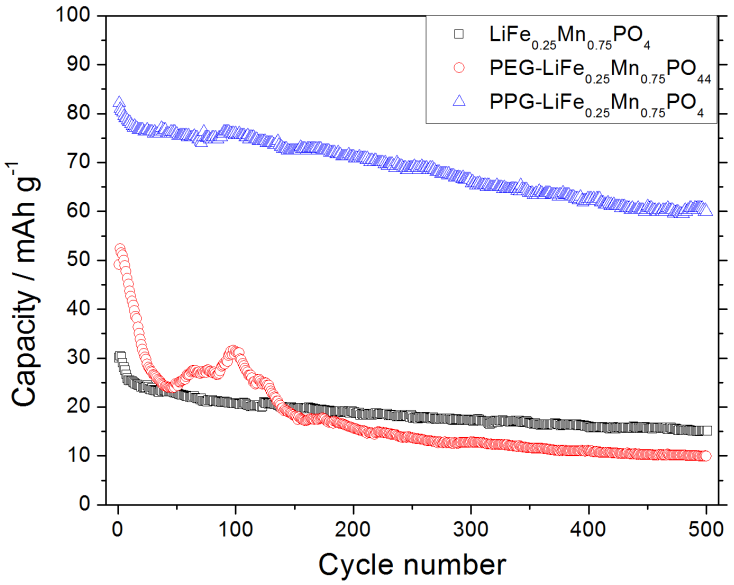

Fig. 4.7 Cycleability of the pristine and carbon coated $LiFe_{0.25}Mn_{0.75}PO_4$ *

* PPG- $LiFe_{0.25}Mn_{0.75}PO_4$ cycled at 10C, while pristine $LiFe_{0.25}Mn_{0.75}PO_4$, PEG-$LiFe_{0.25}Mn_{0.75}PO_4$ cycled at 1C due to their poor rate capabilities.

4.3 Effects of Mn content in PPG-$LiFe_{1-x}Mn_xPO_4$

Carbon coated $LiFe_{0.25}Mn_{0.75}PO_4$ synthesized PAMA have shown impressive electrochemical properties as described in Section 4.2. The effects of Mn content *x* on the structural and electrochemical properties of PPG-$LiFe_{1-x}Mn_xPO_4$ will be further studied in this section. Although high Mn content offers a higher overall potential, the sluggish electrochemical activity of Mn^{2+}/Mn^{3+} redox may result in poor realizable capacity, large polarization, low reaction rates and high reactivitty with electrolyte. Therefore, it is essential to find out the optimum *x* value with the comprehensive considerations of specific capacity, power density, energy density, fast charge capability and cycleability.

4.3.1 Characterization

4.3.1.1 Crystal structure

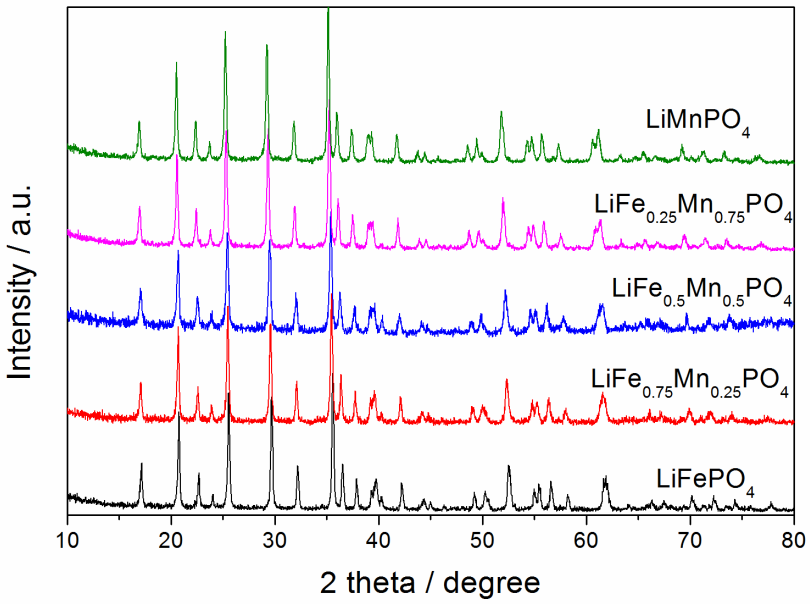

Fig. 4.8 XRD spectra of PPG-$LiFe_{1-x}Mn_xPO_4$ (x = 0, 0.25, 0.5, 0.75 and 1)

Fig. 4.8 shows the XRD spectra of PPG-$LiFe_{1-x}Mn_xPO_4$ synthesized via PAMA method. As can be seen, all the PPG-$LiFe_{1-x}Mn_xPO_4$ materials have the ordered olivine structure of *Pnma* space group over the compositional range of $0 \leq x \leq 1$, without any visible impurities. This indicates that single phase solid-solution of $LiFe_{1-x}Mn_xPO_4$ can be achieved with arbitrary proportions between Fe and Mn. All the reflection peaks of $LiFe_{1-x}Mn_xPO_4$ are notably shifted to the small angle direction with increasing x. Fig. 4.9 shows an example of the reflection peak from (311) planes with highest intensity among all reflections. As can be seen, peak (311) evidently shifts to smaller angle proportionally with increasing x. According to Bragg's diffraction equation, the inter-plane spacing of the $LiFe_{1-x}Mn_xPO_4$ lattice increase with increasing x. Therefore, the variation of lattice constants of $LiFe_{1-x}Mn_xPO_4$ with x can also be calculated based on Bragg's diffraction equation.

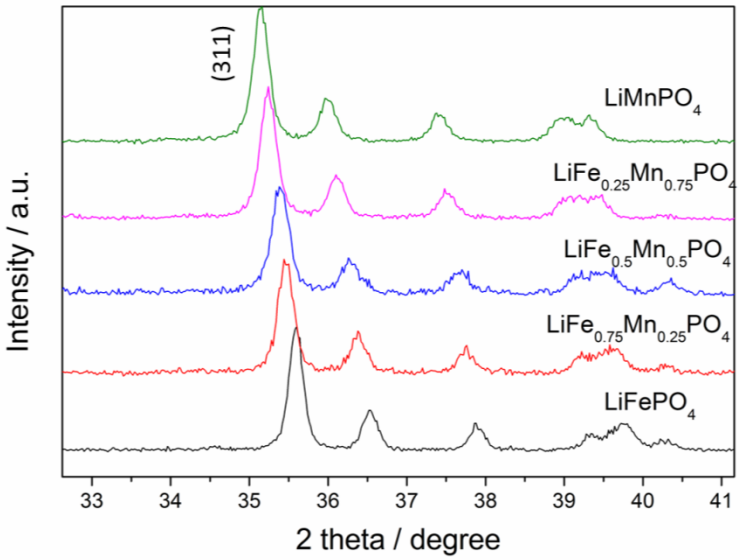

Fig. 4.9 XRD specta of (311) peak of $LiFe_{1-x}Mn_xPO_4$ (x = 0, 0.25, 0.5, 0.75 and 1)

Fig. 4.10 shows the variation of lattice parameters and unit cell volume of the PPG-$LiFe_{1-x}Mn_xPO_4$ with different Mn content *x*. Lattice constants of *a, b* and *c* increase proportionally with *x* from 0 to 1, which agrees well with Vegard's law. This once again demonstrates that Fe and Mn are in solid-solution state on M2 site of olivine $LiMPO_4$ with arbitrary proportion. Lattice constants *a*, *b* and *c* of $LiMnPO_4$ are respectively ~1.3%, ~1.6% and ~1.1% longer than those of $LiFePO_4$. The cell volume of $LiMnPO_4$ is ~4% larger than that of $LiFePO_4$. This expansion in unit cell is in good agreement with literatures [43, 48, 49], due to the larger effective ionic radius of Mn^{2+} (0.83 Å [146]) when compared to Fe^{2+} (0.78 Å [146]) in octahedral M2 site. In an ideal condition, each Mn atom can have four Fe atoms as all the nearest neighbors in $LiFe_{0.5}Mn_{0.5}PO_4$ and $LiFe_{0.75}Mn_{0.25}PO_4$, while each Mn atom have two Fe atoms as the nearest neighbors in $LiFe_{0.25}Mn_{0.75}PO_4$.

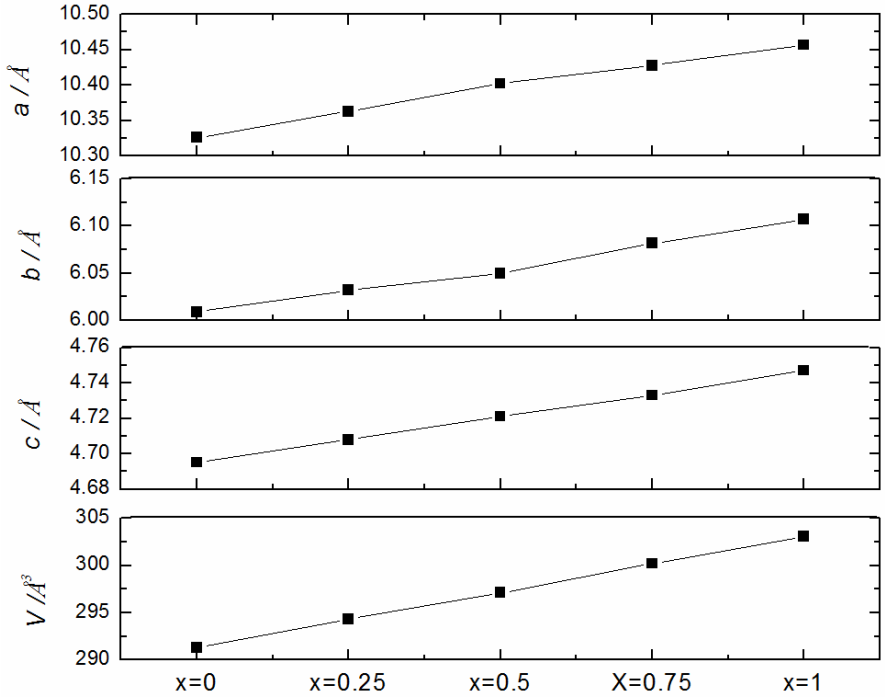

Fig. 4.10 Lattice constant variation with Mn content in PPG-$LiFe_{1-x}Mn_xPO_4$

Mean crystallite size of the PPG-$LiFe_{1-x}Mn_xPO_4$ was estimated using Scherrer equation (Equation 2.1) based on XRD peak broadening. Table. 4.1 summarizes the lattice constants and the estimated crystalline size of PPG-$LiFe_{1-x}Mn_xPO_4$ with x = 0, 0.25, 0.5, 0.75 and 1. PPG-$LiFe_{0.5}Mn_{0.5}PO_4$ has the smallest mean crystallite size of 56 nm, while PPG-$LiFePO_4$ has the largest average crystallites size of 68 nm. The small differences in crystallite size may be resulted from the proportions of raw materials of Fe and Mn salts. However, mean crystallite sizes of PPG-$LiFe_{1-x}Mn_xPO_4$ materials are generally very close to each other. Therefore, the particle size effects on the discussion of electrochemical properties can be neglected here.

Table 4.1 Lattice constants, mean crystallite sizes and carbon contents of PPG-$LiMn_{1-x}Fe_xPO_4$

Composition	a (Å)	b (Å)	c (Å)	V (Å^3)	Grain size (nm)	Carbon content
x = 1	10.326	6.009	4.695	291.3	68	2.2 wt%
x = 0.75	10.363	6.032	4.708	294.3	64	2.1 wt%
x = 0.5	10.402	6.050	4.721	297.1	56	1.6 wt%
x = 0.25	10.428	6.082	4.733	300.2	62	1.8 wt%
x = 0	10.457	6.107	4.747	303.1	62	1.1 wt%

4.3.1.2 Micro-morphology

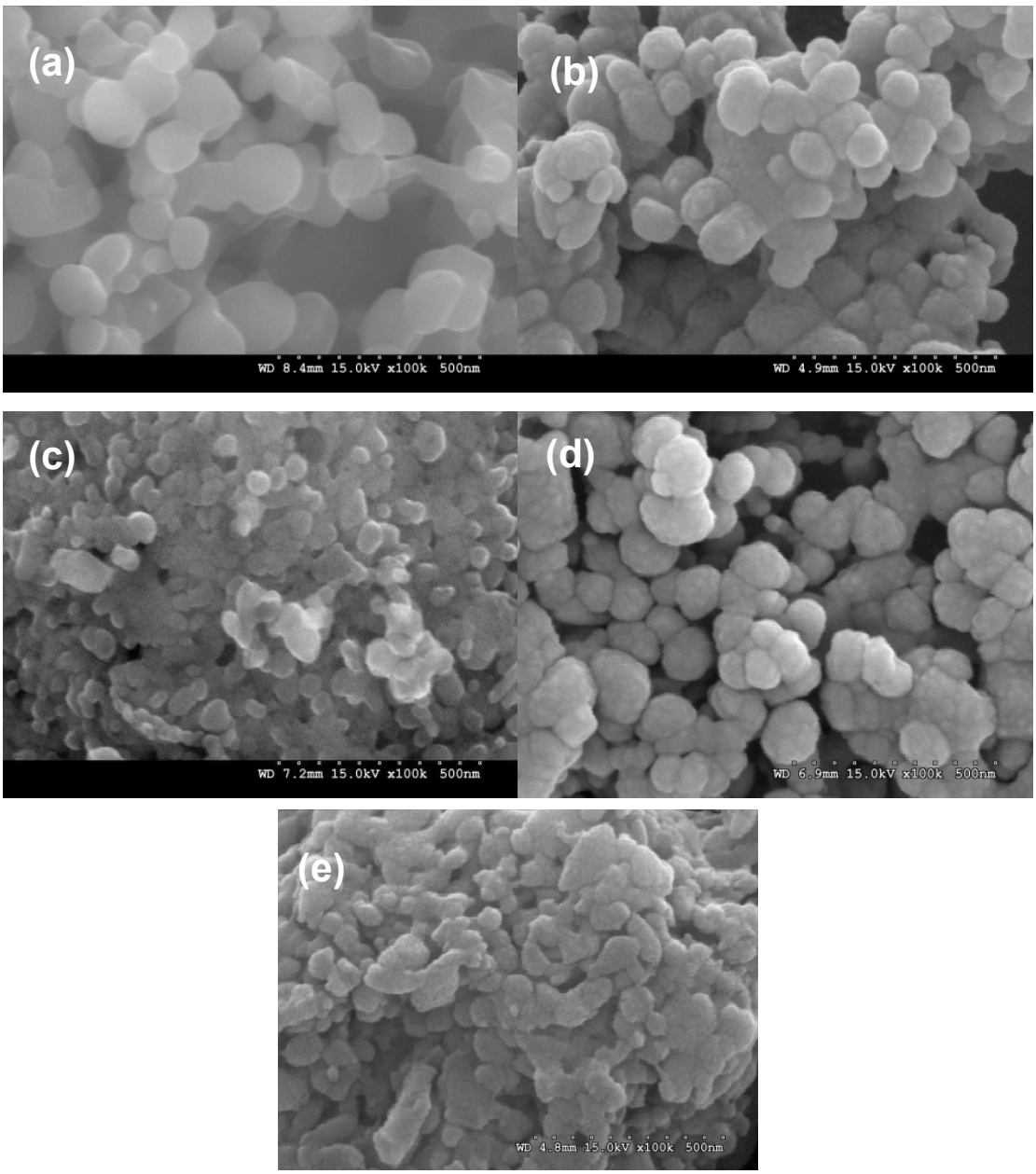

Fig. 4.11 SEM images of PPG-$LiFe_{1-x}Mn_xPO_4$ with (a) $x = 0$, (b) $x = 0.25$, (c) $x = 0.5$, (d) $x = 0.75$ and (e) $x = 1$

Fig. 4.11 shows the SEM images of PPG-$LiFe_{1-x}Mn_xPO_4$. The primary particle size of PPG-$LiFe_{1-x}Mn_xPO_4$ is generally about 50 nm, which agrees well with the crystallite size estimation from XRD analysis. The small primary particles are agglomerated in the secondary particles of micrometer size. The micro-morphology of the

PPG-$LiFe_{1-x}Mn_xPO_4$ was further characterized using high-resolution TEM as shown in Fig. 4.12. The primary particles are well wrapped by a very uniform thin layer of amorphous carbon, leading to desirable electronic transport in the electrode, where the electrons can be delivered to any surface point of nanoparticles. The primary particles are also well separated from each other by the thin carbon coatings. Hence, the specific active contact area between the electrolyte and PPG-$LiFe_{1-x}Mn_xPO_4$ electrode is supposed to be larger in comparison to the uncoated $LiFe_{1-x}Mn_xPO_4$.

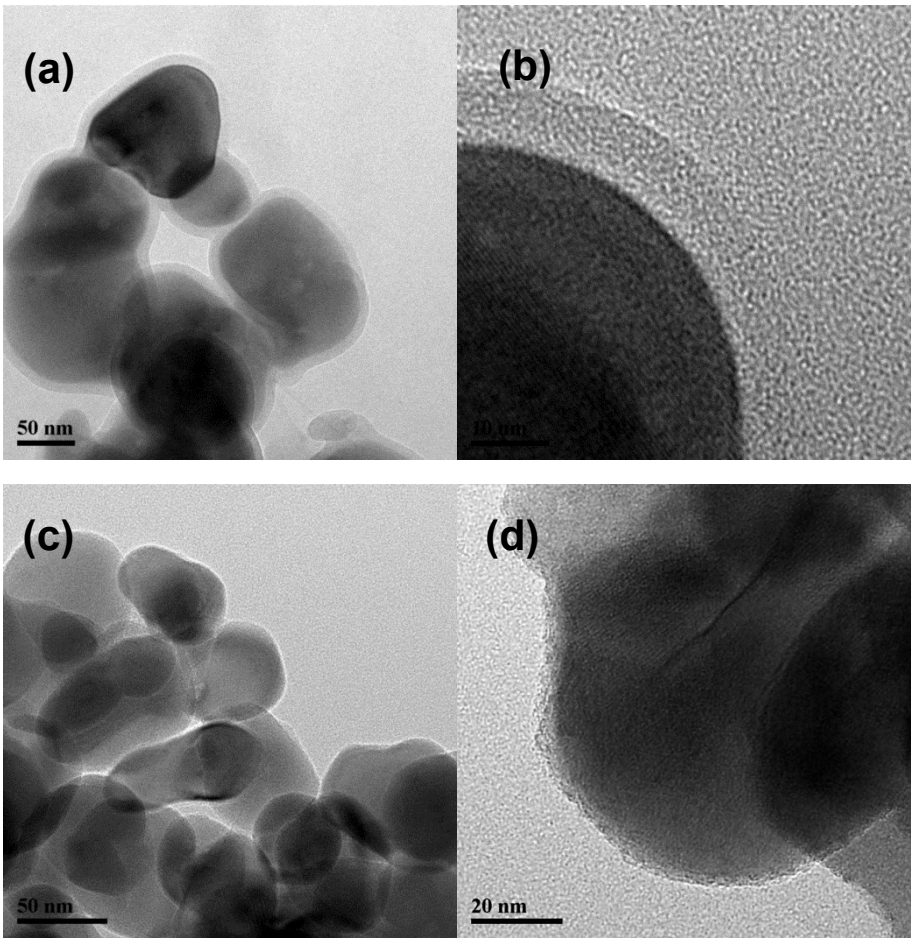

Fig. 4.12 TEM images of PPG-$LiFe_{1-x}Mn_xPO_4$; (a) and (b) x=0, (c) and (d) x=0.75

4.3.2 Electrochemical properties

4.3.2.1 Cyclic voltammetry

As shown in Fig. 4.13, Fe^{2+}/Fe^{3+} and Mn^{2+}/Mn^{3+} redox reactions of PPG-$LiFe_{1-x}Mn_xPO_4$ were studied using cyclic voltammetry. The potential hysteresis between cathodic and anodic peaks of Fe^{2+}/Fe^{3+} and Mn^{2+}/Mn^{3+} redox couples are denoted as ΔV_1 and ΔV_2, respectively. As for Fe^{2+}/Fe^{3+} redox couple, ΔV_1 remains almost invariable of ~160 mV with different Mn contents. On the other hand, as for Mn^{2+}/Mn^{3+} redox couple, ΔV_2 increases dramatically with increasing Mn content or x in PPG-$LiFe_{1-x}Mn_xPO_4$. $LiMnPO_4$ has very large polarization with ΔV_2 of 816 mV. This polarization of Mn^{2+}/Mn^{3+} redox couple is significantly reduced with Fe substitution. ΔV_2 of $LiFe_{0.25}Mn_{0.75}PO_4$ is reduced to 410 mV, while ΔV_2 of $LiFe_{0.5}Mn_{0.5}PO_4$ is further reduced to 270 mV, demonstrating that the Fe-O-Mn super-exchange interaction can evidently facilitate the reaction of Mn^{2+}/Mn^{3+} [43, 49]. $LiFe_{0.75}Mn_{0.25}PO_4$ has the smallest polarization with ΔV_2 of 232 mV, which is still ~70 mV larger than ΔV_1 (Fe^{2+}/Fe^{3+}) of the same sample. This implies the sluggish reaction activity of Mn^{2+}/Mn^{3+} redox couple even with Mn all surrounded by Fe atoms. In addition to the reduction of strong polarization in $LiMnPO_4$, the Fe substitution of Mn also significantly increases the peak current, leading to much higher realizable capacity. Hence, it can be concluded that the interaction of Fe-O-Mn evidently reduces polarization of Mn^{2+}/Mn^{3+} reaction.

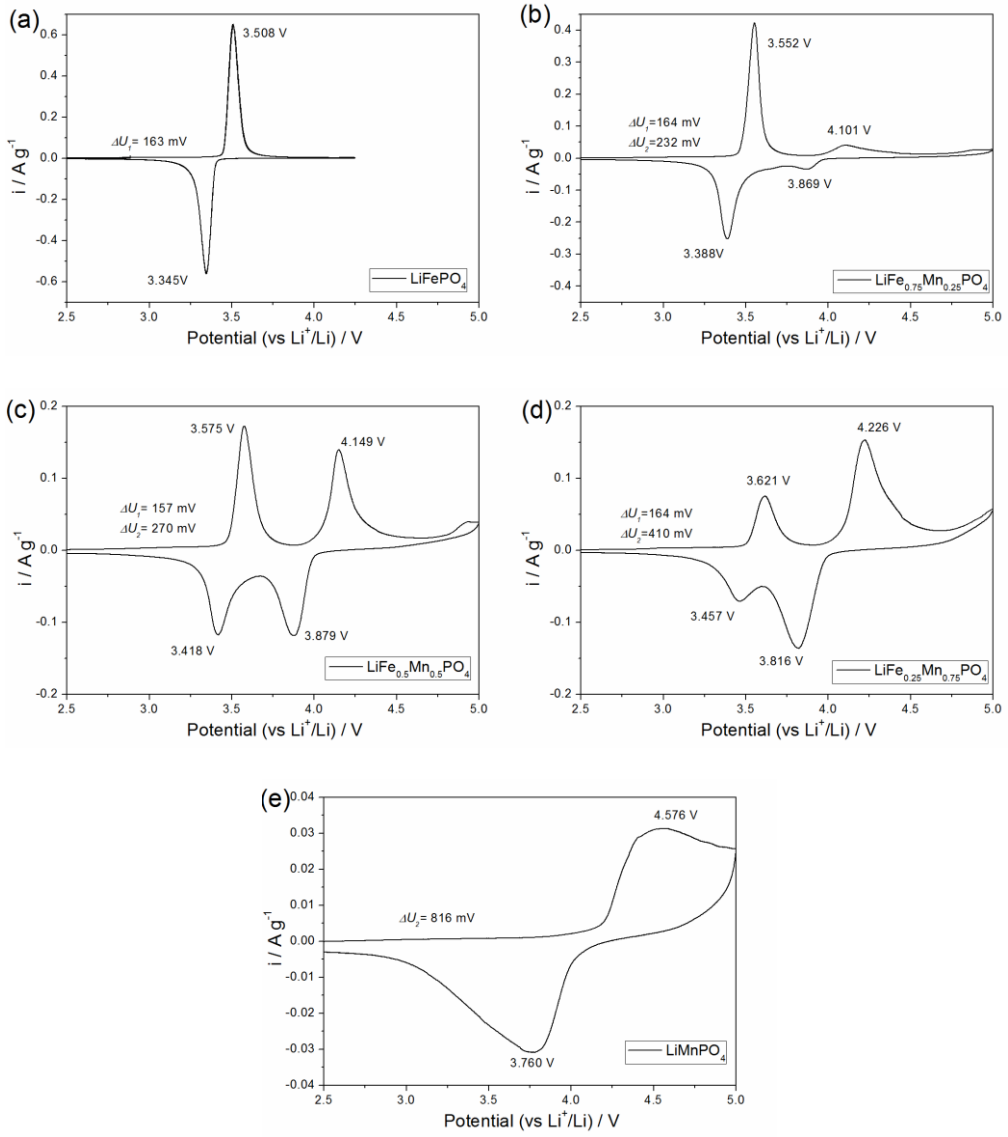

Fig. 4.13 Cyclic voltammetry of PPG-$LiFe_{1-x}Mn_xPO_4$ with (a) $x = 0$, (b) $x = 0.25$, (c) $x = 0.5$, (d) $x = 0.75$ and (e) $x = 1$, recorded at 0.1 mV s^{-1}

Another interesting finding in the CV analyses is the positions of cathodic and anodic peaks of Fe^{2+}/Fe^{3+} and Mn^{2+}/Mn^{3+} in PPG-$LiFe_{1-x}Mn_xPO_4$ shift apparently to higher potential with increasing x. The redox center of Fe^{2+}/Fe^{3+} is 3.426 V, 3.470 V, 3.496 V and 3.539 V for x = 0, 0.25, 0.5 and 0.75. Cathodic and anodic peaks for Fe^{2+}/Fe^{3+} of $LiFe_{0.75}Mn_{0.25}PO_4$ are at 3.457 V/3.621 V, while those of $LiFePO_4$ are 3.345 V / 3.508 V. The Fe^{2+}/Fe^{3+} redox couple has been elevated > 0.1 eV in $LiFe_{0.75}Mn_{0.25}PO_4$

when compared to that in $LiFePO_4$. The redox center of Mn^{2+}/Mn^{3+} is 3.985 V, 4.014 V, 4.021 V and 4.168 V, which also increases with the Mn content *x*. The increase of redox center should be ascribed to the lattice expansion as described in Section 4.3.1.1. The M-O (M = Fe and Mn) bond length in $LiFe_{1-x}Mn_xPO_4$ increase with Mn content *x*, resulting in the higher Fermi energy of the Fe^{2+}/Fe^{3+} and Mn^{2+}/Mn^{3+} redox couples in the olivine lattice.

4.3.2.2 Specific capacity

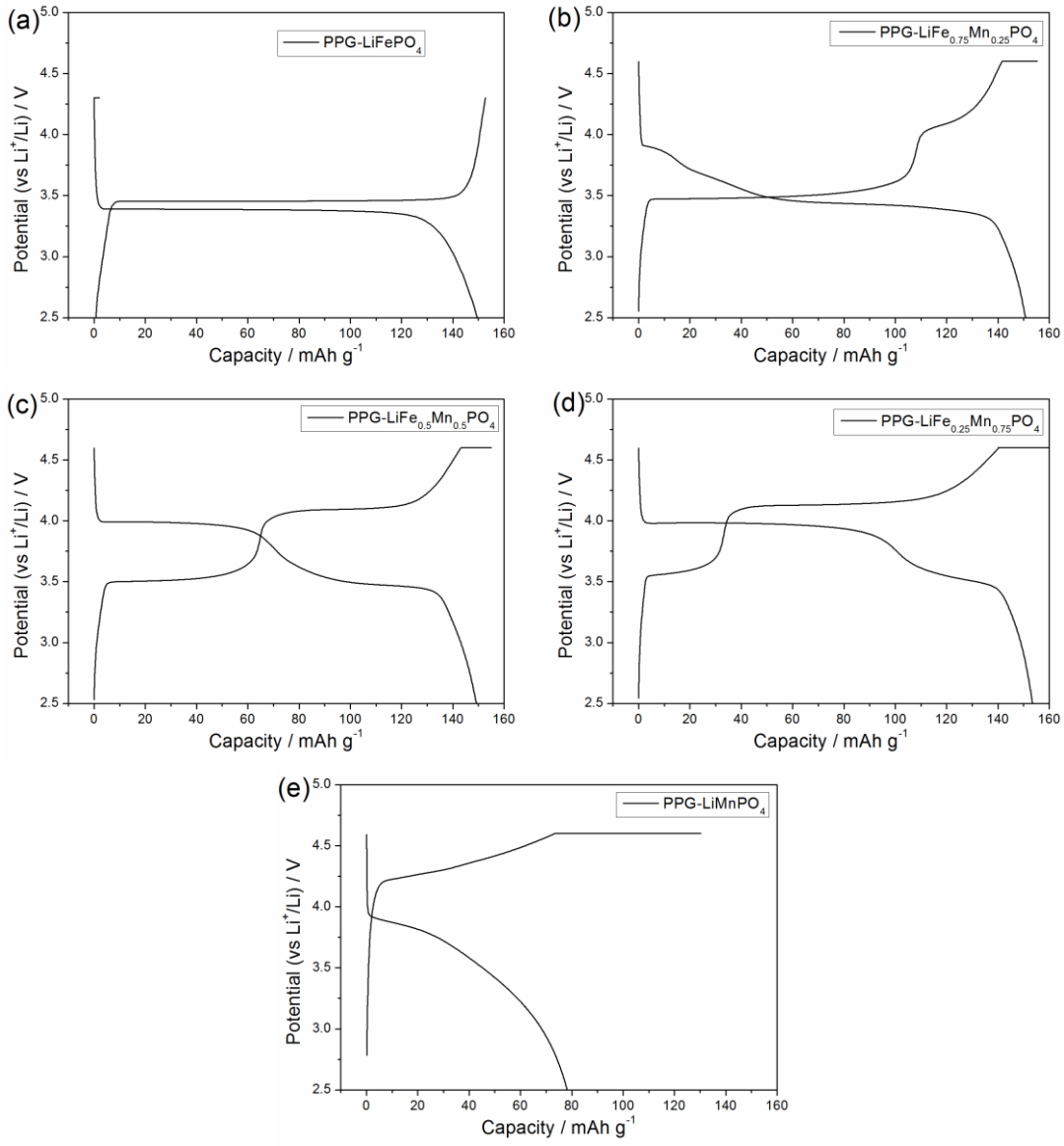

Fig. 4.14 Charge-discharge curves of PPG-$LiFe_{1-x}Mn_xPO_4$ at 0.1C with (a) x = 0, (b) x = 0.25, (c) x = 0.5, (d) x = 0.75 and (e) x = 1

Fig. 4.14 shows charge-discharge curves of PPG-$LiFe_{1-x}Mn_xPO_4$ (x = 0, 0.25, 0.5, 0.75 and 1) at 0.1C. To achieve higher attainable capacity, all the PPG-$LiFe_{1-x}Mn_xPO_4$ half-cells were charged following a CCCV protocol with a low charge rate of 0.1C and constant voltage charge to 0.02 C. The attainable capacity of PPG-$LiMnPO_4$ is considerably higher than that of pristine $LiMnPO_4$ as described in Chapter 2 owing to the conductive coating and nano-sizing effects. Nevertheless, the reversible specific capacity of PPG-$LiMnPO_4$ is only 78 mAh g^{-1}. PPG-$LiMnPO_4$ also shows a poor reversibility with a low coulombic efficiency of 61% in the first cycle, implying a strong side reaction of electrolyte. This sluggish electrochemical activity is due to the inherently poor electronic/ionic transport and Jahn-Teller lattice distortion of $LiMnPO_4$ [43, 49]. With the effective conductive coating and nano-sizing of PAMA, all the PPG-$LiFe_{1-x}Mn_xPO_4$ (x = 0, 0.25, 0.5 and 0.75) materials containing Fe show high specific capacity > 150 mAh g^{-1} at low current density of 0.1C. The 4 V voltage plateau contributed by Mn^{2+}/Mn^{3+} redox couple stretches longer with the Mn content x, leading to higher overall voltage. The results of specific capacity clearly indicate that the Fe substitution can effectively activate the Mn^{2+}/Mn^{3+} in olivine lattice and increase the attainable capacity of $LiFe_{1-x}Mn_xPO_4$.

4.3.2.3 Discharge rate capability

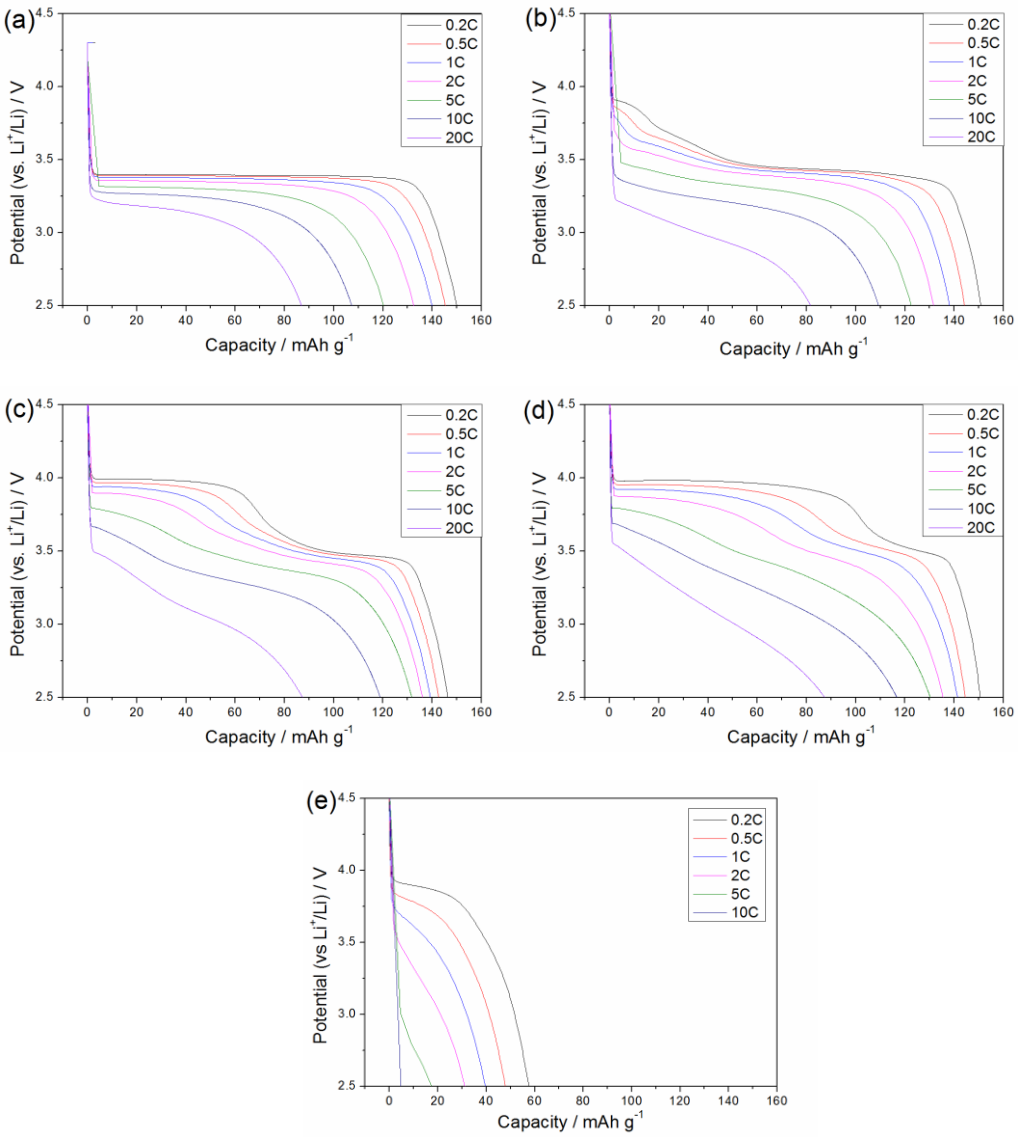

Fig. 4.15 Discharge rate capability of PPG-$LiFe_{1-x}Mn_xPO_4$ with (a) $x = 0$, (b) $x = 0.25$, (c) $x = 0.5$, (d) $x = 0.75$ and (e) $x = 1$

Fig. 4.15 shows the discharge rate capability of PPG-$LiFe_{1-x}Mn_xPO_4$. To achieve the same starting point of the fully charged states, all the PPG-$LiFe_{1-x}Mn_xPO_4$ half-cells were charged following a CCCV protocol with a low charge rate of 0.2C and constant voltage charge to 0.02 C. As can be seen, PPG-$LiFePO_4$ shows impressive discharge rate capability, whereas PPG-$LiMnPO_4$ has extremely poor rate capability, although

they were fabricated and processed identically. The specific capacity of PPG-$LiMnPO_4$ is only 57 mAh g^{-1}, around 1/3 of its theoretical capacity. The realizable capacity gets even worse at high current densities. For example, discharge capacity of PPG-$LiMnPO_4$ at 10C is only 5 mAh g^{-1}. It should be noted that the specific capacity of PPG-$LiMnPO_4$ is far larger than those of pristine $LiMnPO_4$ and $Li_{0.96}Ru_{0.01}MnPO_4$ in Chapter 3, indicating the effectiveness of carbon coating. With Mn partially substituted by Fe, PPG-$LiFe_{1-x}Mn_xPO_4$ ($0.25 \leq x \leq 0.75$) also shows good capacity retention at high current densities, similar to PPG-$LiFePO_4$. The capacity retention of PPG-$LiFe_{1-x}Mn_xPO_4$ at various current densities seems to be almost the same with PPG-$LiFe_{1-x}Mn_xPO_4$ with $0.25 \leq x \leq 0.75$. This indicates that Mn content in PPG-$LiFe_{1-x}Mn_xPO_4$ in the range of $0 \leq x \leq 0.75$ barely affects the realizable capacity even at high discharge current densities.

PPG-$LiFe_{1-x}Mn_xPO_4$ tends to have a higher overall potential with higher Mn content x, leading to higher energy and power density at the same current density. The energy and power densities of the PPG-$LiFe_{1-x}Mn_xPO_4$ at various current densities are compared in Fig. 4.16. As can be seen, PPG-$LiFe_{0.5}Mn_{0.5}PO_4$ and PPG-$LiFe_{0.25}Mn_{0.75}PO_4$ exhibit noticeably higher power and energy densities than PPG-$LiFePO_4$ does at almost every current rate. At a low current rate of 0.2C, PPG-$LiFe_{0.25}Mn_{0.75}PO_4$ provides energy density of 563 Wh Kg^{-1} compared to 506 Wh Kg^{-1} of PPG-$LiFePO_4$. At a high current rate of 5C, the energy and power density of the PPG-$LiFe_{0.25}Mn_{0.75}PO_4$ are 10.8% and 10.6% higher than that of the PPG-$LiFePO_4$, respectively. However, PPG-$LiFe_{0.5}Mn_{0.5}PO_4$ surpasses PPG-$LiFe_{0.25}Mn_{0.75}PO_4$ in both

energy and power density when the discharge current rate exceeds 10C. The energy density of the PPG-$LiFe_{0.25}Mn_{0.75}PO_4$ even falls below that of the PPG-$LiFePO_4$ at 20C, although their absolute discharge capacities are very close to each other. This phenomenon can be ascribed to the large polarization of PPG-$LiFe_{0.25}Mn_{0.75}PO_4$ at high current densities as shown in Fig. 4.15. Due to the relatively low practical operation voltage at high current rates, the practical power and energy densities of PPG-$LiFe_{0.75}Mn_{0.25}PO_4$ are significantly limited. As discussed the CV tests of PPG-$LiFe_{0.5}Mn_{0.5}PO_4$, electrode polarizations and reaction resistances of PPG-$LiFe_{0.25}Mn_{0.75}PO_4$ are much larger when compared to PPG-$LiFe_{0.75}Mn_{0.25}PO_4$ and PPG-$LiFe_{0.5}Mn_{0.5}PO_4$ due to the high content of inactive Mn.

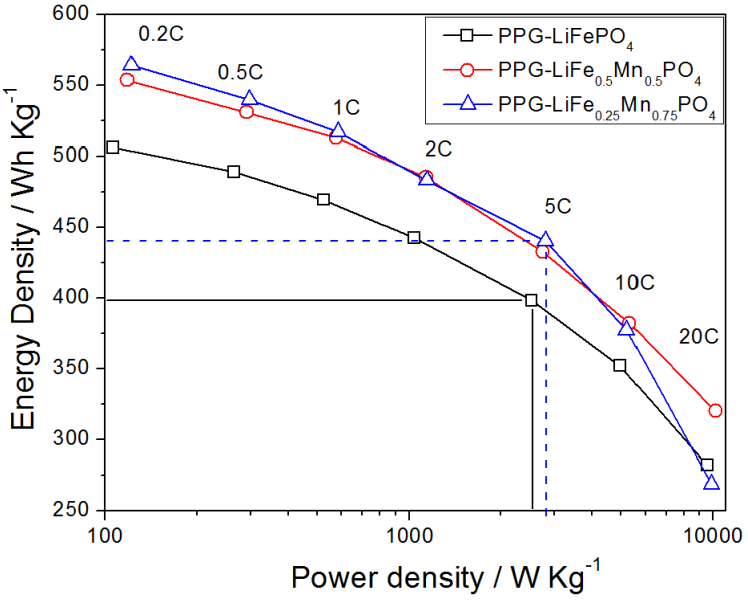

Fig. 4.16 Power and energy density comparison of PPG-$LiFe_{1-x}Mn_xPO_4$ (x=0, 0.5 and 0.75)

4.3.2.4 Fast charge capability

Fast charge capability of PPG-$LiFe_{1-x}Mn_xPO_4$ was characterized through constant

current charge as shown in Fig. 4.17. All the PPG-$LiFe_{1-x}Mn_xPO_4$ half-cells were charged at various current rates without prolonged constant voltage charge. As can be seen, the fast charge capability of the PPG-$LiFe_{1-x}Mn_xPO_4$ generally subsides with increasing Mn content x. PPG-$LiFePO_4$ exhibits superior fast charge capability. The PPG-$LiFePO_4$ can be charged to ~90% state of charge (SOC) at 10C. At the other extreme, the charge rate capability of PPG-$LiMnPO_4$ is extremely poor. Even at a low current rate of 0.2C, only 32 mAh g^{-1} can be charged for PPG-$LiMnPO_4$. As for PPG-$LiFe_{1-x}Mn_xPO_4$, the 3.5 V plateau of Fe^{2+}/Fe^{3+} decreases mildly with increasing current rate, whereas the 4 V plateau of Mn^{2+}/Mn^{3+} drops dramatically with increasing current rate. Therefore, charge capacities of PPG-$LiFe_{1-x}Mn_xPO_4$ are mainly limited by the inferior activity of Mn^{2+}/Mn^{3+}. On the other hand, PPG-$LiFe_{0.25}Mn_{0.75}PO_4$ can discharge 117 mAh g^{-1} at 10C, whereas 33 mAh g^{-1} can be charged at the same current density. This indicates that the Li^+ extraction from olivine $LiFe_{1-x}Mn_xPO_4$ seems to be more difficult when compared to the Li^+ insertion.

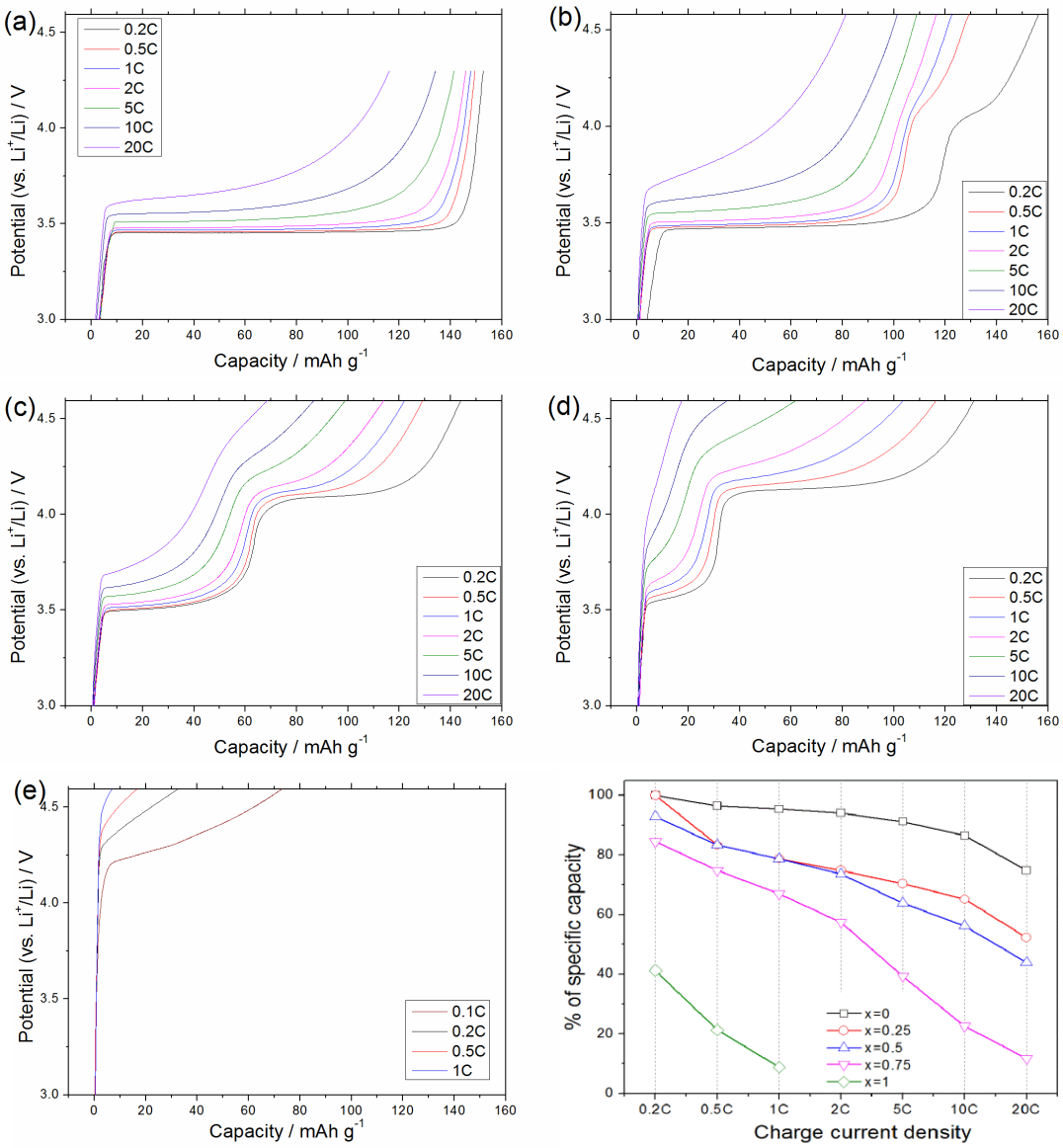

Fig. 4.17 Fast charge capability of PPG-$LiFe_{1-x}Mn_xPO_4$ (x=0, 0.25, 0.5 and 0.75)

4.3.2.5 Cycleability

Fig. 4.18 shows the cyclic performances of the PPG-$LiFe_{1-x}Mn_xPO_4$ cycled at 10C. To achieve higher charge capacities, the PPG-$LiFe_{1-x}Mn_xPO_4$ half-cells were charged using a CCCV mode, i. e. constant current charge at 10C followed by a constant voltage charge for 5 min. The PPG-$LiMnPO_4$ is not included in the long-term cyclic tests since the realizable capacity of the PPG-$LiMnPO_4$ at 10C is too low to provide a meaningful

comparison. Due to disparity in fast charge capability, the initial capacity of the PPG-$LiFe_{1-x}Mn_xPO_4$ in the cyclic tests generally decreases with increasing Mn content *x*. PPG-$LiFePO_4$ has the highest initial capacity of 125 mAh g^{-1} and also the best cyclic performances. A capacity of 111 mAh g^{-1}, 89% of the initial capacity, can be retained after 500 cycles. Despite of the differences in initial capacities, the capacity retention ratio of the PPG-$LiFe_{1-x}Mn_xPO_4$ also evidently decreases with increasing Mn content *x*. After 500 cycles, 84%, 81% and 73% of the initial capacity can be retained for PPG-$LiFe_{0.75}Mn_{0.25}PO_4$, PPG-$LiFe_{0.5}Mn_{0.5}PO_4$ and PPG-$LiFe_{0.25}Mn_{0.75}PO_4$, respectively. The cause of the capacity fading is believed to be Mn dissolution in electrolyte [51, 61]. Fe substitution can stabilize the crystal structure and reduces the number of Mn atoms exposed to the electrolyte.

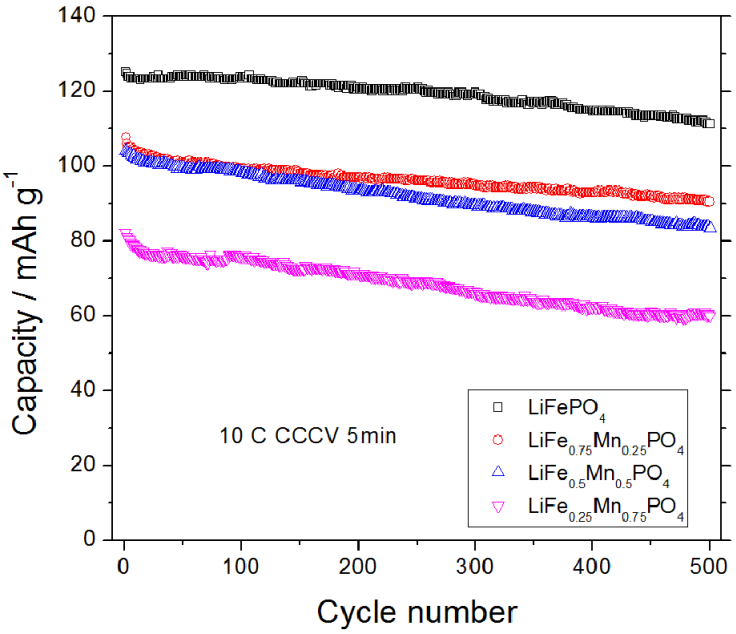

Fig. 4.18 Cyclic performances of PPG-$LiFe_{1-x}Mn_xPO_4$ (*x*=0, 0.25, 0.5 and 0.75) at 10C.

4.4 Summary

In summary, a facile polymer-assisted mechanical activation was proposed to synthesize electrochemical active $LiFe_{1-x}Mn_xPO_4$/C composites. The $LiFe_{1-x}Mn_xPO_4$/C composites synthesized with assistance of PPG have uniformly fine particle size of ~60 nm and thin carbon coating of 1-2 nm, leading to greatly improved electrochemical properties. The effects of Mn content on electrochemical properties of PPG-$LiFe_{1-x}Mn_xPO_4$ were thoroughly studied in this chapter. The existence of Fe-O-Mn interaction significantly reduced the polarization Mn^{2+}/Mn^{3+} reaction, whereas Mn content in PPG-$LiFe_{1-x}Mn_xPO_4$ increased the overall voltage, but also increased the polarizations of the Mn^{2+}/Mn^{3+} reaction. It seems that Mn content had little effects on the Li^+ insertion process with $x \leq 0.75$ after effective carbon coating. PPG-$LiFe_{1-x}Mn_xPO_4$ with $x \leq 0.75$ exhibited very good discharge rate capability and thus high energy/power density. Energy density of the PPG-$LiFe_{1-x}Mn_xPO_4$ is ~12% higher than that of $LiFePO_4$ at a low current density of 0.2C. On the other hand, Mn content drastically affects the Li^+ extraction process of $LiFe_{1-x}Mn_xPO_4$. Fast charge capability of PPG-$LiFe_{1-x}Mn_xPO_4$ evidently decreases with increasing Mn content. With high Mn content, PPG-$LiFe_{0.25}Mn_{0.75}PO_4$ showed an inferior fast charge rate capability. Moreover, high Mn content also resulted in relatively worse cyclic performances. In considering the energy/power density, fast charge capability and cycleability, the PPG-$LiFe_{0.5}Mn_{0.5}PO_4$ may the best candidate among these $LiFe_{1-x}Mn_xPO_4$ materials for large-scale applications in EV/HEVs.

5 High potential tavorite $LiVPO_4F$: a high performance alternative

As indicated in Chapter 4, the fast charge capability of the "4 V" $LiFe_{0.25}Mn_{0.75}PO_4$ is not very encouraging, although the discharge rate capability and power density are very promising for large-scale applications. In this chapter, a high performance "4 V" cathode material tavorite $LiVPO_4F$ has been studied as a potential alternative to the olivine $LiMPO_4$ (M = Fe, Mn etc.). Carbon coated $LiVPO_4F$ exhibits amazing discharge-charge rate capability and good cyclic performance. Furthermore, some essential but still uncertain properties such as conductivities, ionic diffusion coefficients and Li^+ extraction/insertion mechanisms of this tavorite $LiVPO_4F$ material have also been studied for the first time.

5.1 Materials preparation

Carbon free $LiVPO_4F$ was synthesized via a two-step solid-state reaction with hydrogen thermal reduction (HTR). Raw materials of vanadium oxide (V_2O_5, 99%) and ammonium dihydrogen phosphate ($NH_4H_2PO_4$, 99%) were milled for 2 h without any additives. Reduction of V^{5+} to V^{3+} was achieved by heating the powder mixture at 700 ºC in flowing forming gas (5 vol% hydrogen in argon). The pre-calcinated powder was then milled again with 2 mol% excessive lithium fluoride (LiF, 99%) for 15 min. Grey green colored pellets were finally obtained after a second calcination at 700 ºC in argon for 15 min.

$LiVPO_4F$/C composite was synthesized via a two-step solid-state reaction with carbon thermal reduction (CTR). First, raw materials of V_2O_5, $NH_4H_2PO_4$ and acetylene carbon black were ball milled for 2 h using SPEX-8000M high-energy milling machine. Stainless steel jar and balls were used with a small amount of stearic acid as processing control agent to improve the milling efficiency. The mixed powder was calcinated at 700 ºC for 12 hours with flowing argon to obtain precursor of VPO_4/C. Black $LiVPO_4F$/C powder was finally obtained after a second calcination at 700 ºC in flowing argon.

5.2 Characterization

5.2.1 Crystal structure

Fig. 5.1(a) shows the XRD spectra and Rietveld refinement of $LiVPO_4F$/C and $LiVPO_4F$. The two materials have similar diffraction patterns of *P-1* triclinic phase. The excessive LiF added in the milling process compensated for the loss of fluorine and lithium during calcination, which successfully prevented common $Li_3V_2(PO_4)_3$ impurity reported before [123, 124]. Rietveld refinement was carried out using GSAS+EXPGUI [155, 156] to further identify the crystal structure. Starting crystal structure in the refinement was set as isomorph $LiFePO_4F$ based on references [157]. The refined pattern fitted very well with the crystal structure of amblygonite $LiAlPO_4F$ and tavorite $LiFePO_4(OH)$. The refined crystal structure of $LiVPO_4F$/C and $LiVPO_4F$ are almost identical. Refined crystal constants shown in Table 5.1 agree well with previous reports [124, 158]. Fig. 5.1 (b) shows the schematic primitive cell crystal structure of $LiVPO_4F$.

With cell volume of 174.6 $Å^3$, theoretical density of $LiVPO_4F$ is only 2.92 g cm^{-3}, lower than that of $LiFePO_4$ (3.6 g cm^{-3}) and $LiMnPO_4$ (3.4 g cm^{-3}).

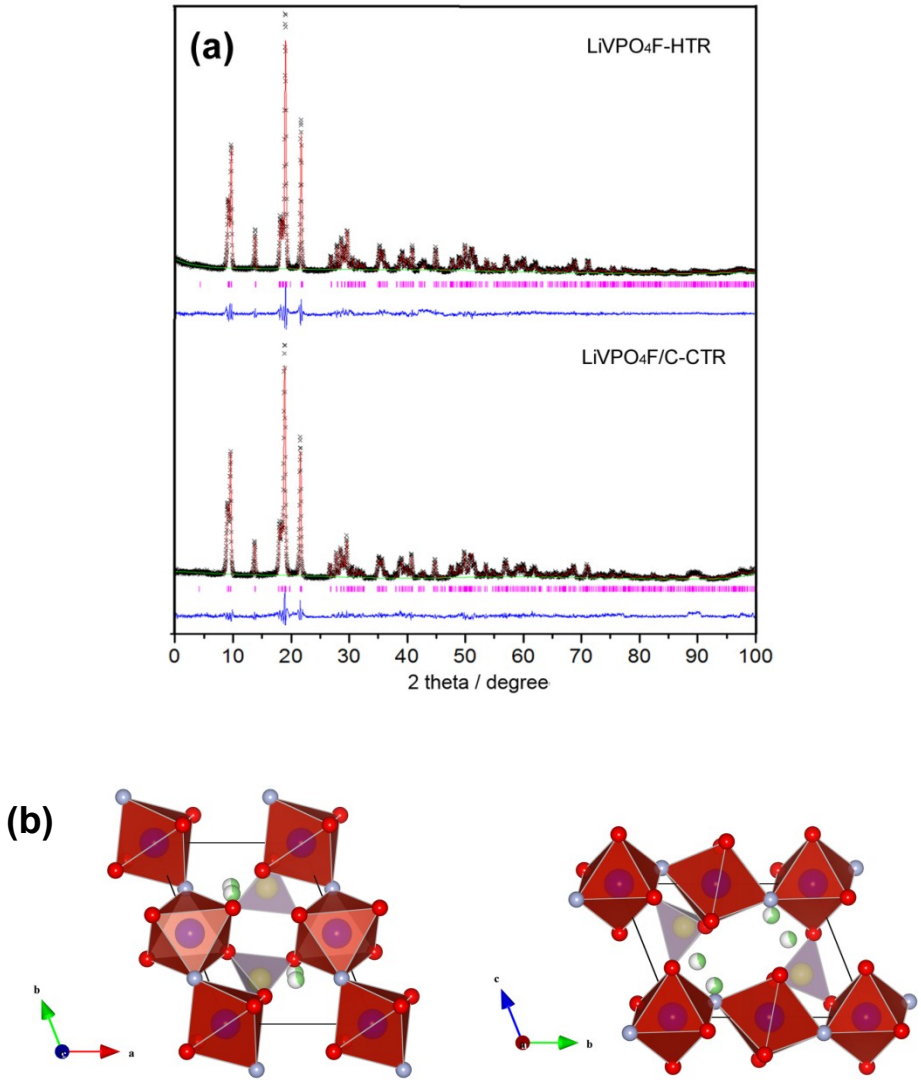

Fig. 5.1 (a) XRD spectra and Rietveld refinement of $LiVPO_4F$, and (b) schematic of crystal structure of $LiVPO_4F$.

In the lattice of tavorite $LiVPO_4F$, VO_4F_2 octahedrons are linked with corner sharing F^- ion in zigzag chains. The zigzag chains of VO_4F_2 octahedron are further cross-linked by PO_4 tetrahedrons, forming a 3-D framework for Li^+ migration. Li^+ ions

locate in severely disordered octahedrons and are split into two sites similar to the case of amblygonite $LiAlPO_4F$. The most likely lithium migration tunnels lie along [001] and [100] with consideration of migration length and tunnel width. Li^+ transport in $LiVPO_4F$ lattice is expected to be easier than that in olivine structured $LiMPO_4$ (M= Fe, Mn, etc.) with only one favorable migration tunnel. Transitional metal V^{3+} ions are separated either by corner sharing electronegative F^- or covalent-bonded PO_4 tetrahedrons, therefore hopping conduction between V-V may be relatively weak, resulting in a poor electronic transport property.

Table 5.1 XRD Rietveld refinement results and atomic parameters of $LiVPO_4F$

$LiVPO_4F$-HTR	a = 5.3115(2) Å	α=107.934(3) °	V=174.62 Å^3	R_{wp} =10.06%
	b = 7.2617(2) Å	β = 98.444(3) °		R_p = 7.58%
	c = 5.1744(2) Å	γ = 107.547(3) °		CHI^2 =3.420
$LiVPO_4F$/C-CTR	a = 5.3104(3) Å	α =107.950(5) °	V=174.56 Å^3	R_{wp} =11.37%
	b = 7.2636(4) Å	β = 98.404(4) °		R_p =8.66%
	c =5.1731(3) Å	γ = 107.573(4) °		CHI^2 =3.748

atom	***x***	***y***	***z***	**Occupancy**	U_{iso}
Li1	0.625(7)	0.301(7)	0.250(9)	0.5	0.019
Li2	0.612(6)	0.211(6)	0.266(7)	0.5	0.019
V1	0	1/2	0	1	0.025(2)
V2	0	0	0	1	0.019(2)
P	0.6495(10)	0.7532(10)	0.3283(11)	1	0.015(1)
O1	0.6655(15)	0.8534(16)	0.1055(21)	1	0.025(3)
O2	0.3613(21)	0.6406(14)	0.3175(19)	1	0.016(2)
O3	0.7985(18)	0.5978(15)	0.2645(17)	1	0.020(3)
O4	0.2407(17)	0.0966(15)	0.3678(21)	1	0.019(3)
F	0.9201(14)	0.2554(14)	0.1159(15)	1	0.012(3)

5.2.2 Micromorphology

Residual carbon content in $LiVPO_4F$/C was determined to be 8.1 wt% by elemental

analysis and further confirmed to be 9 wt% by thermogravimetric analysis. Fig. 5.2 shows the SEM and TEM images of $LiVPO_4F$/C and $LiVPO_4F$. As can be seen, particle size of $LiVPO_4F$/C (~150 mm) is much smaller than that of $LiVPO_4F$ (~400 nm), even though the synthesis processes for both materials were almost identical. Discrete $LiVPO_4F$ particles are also well segregated by extensively dispersed carbon additives, thus reducing serious particle agglomeration of $LiVPO_4F$ as shown in Fig. 5.2 (b). From the high-resolution TEM image, the $LiVPO_4F$ particles were well wrapped by amorphous carbon layer of ~6 nm in thickness. Carbon black additives of $LiVPO_4F$/C successfully impeded the grain growth and coarsening during calcination.

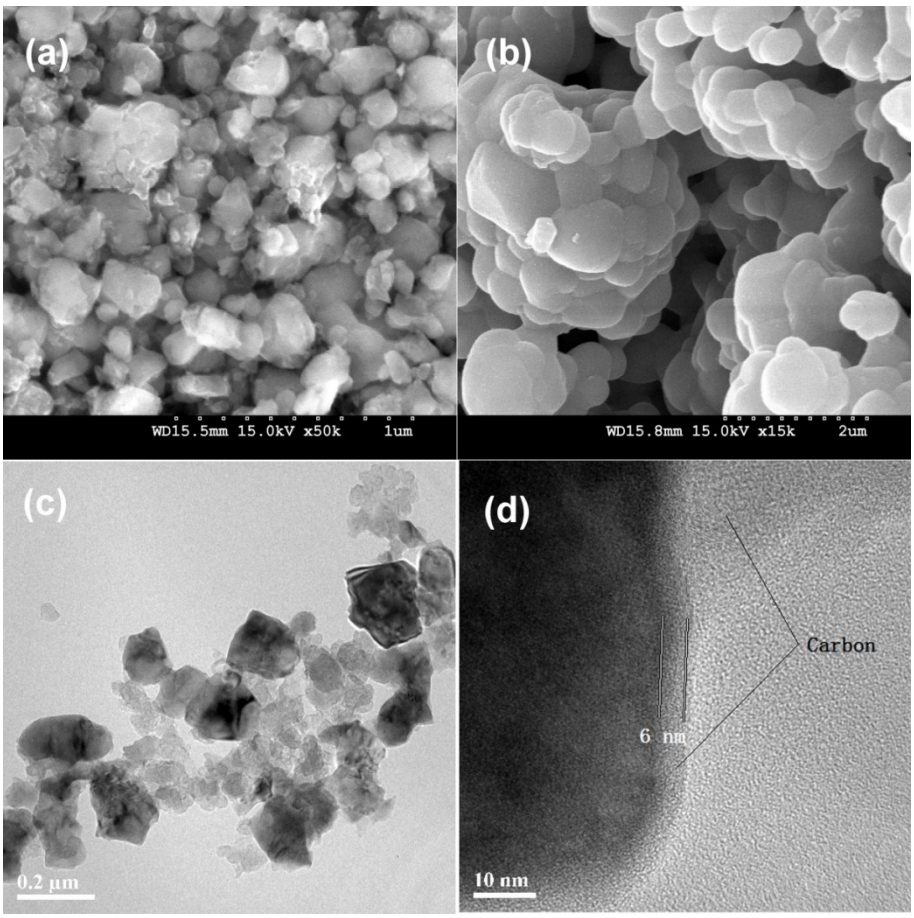

Fig. 5.2 Micro-morphology of LiVPO4F/C and LiVPO4F;

(a) SEM image of LiVPO4F/C, (b) SEM image of LiVPO4F, and (c, d) TEM images of LiVPO4F/C.

5.2.3 Conductivity

The total electrical conductivity of bulk $LiVPO_4F$ was measured using impedance spectroscopy with ionic-blocking disc specimens of Au/$LiVPO_4F$/Au. The measured electrical conductivity denoted as σ_{AC} was contributed from both electronic and ionic transport. As shown in Fig. 5.3(a), σ_{AC} of $LiVPO_4F$ is 8.1×10^{-7} S cm^{-1} at room temperature, which is notably higher than those of isomorph $LiFeSO_4F$ (7.0×10^{-11} S cm^{-1} [119]) and olivine $LiFePO_4$ (1.39×10^{-9} S cm^{-1} [45]). The straight line tail in the low frequency range of the Cole-Cole plot evidently indicates a strong ionic diffusion, similar to the report [119] of isomorph $LiFeSO_4F$. Therefore, the ionic transport should be dominant in tavorite $LiVPO_4F$ lattice at room temperature, in contrast to the electronic dominated mechanism in olivine lattice.

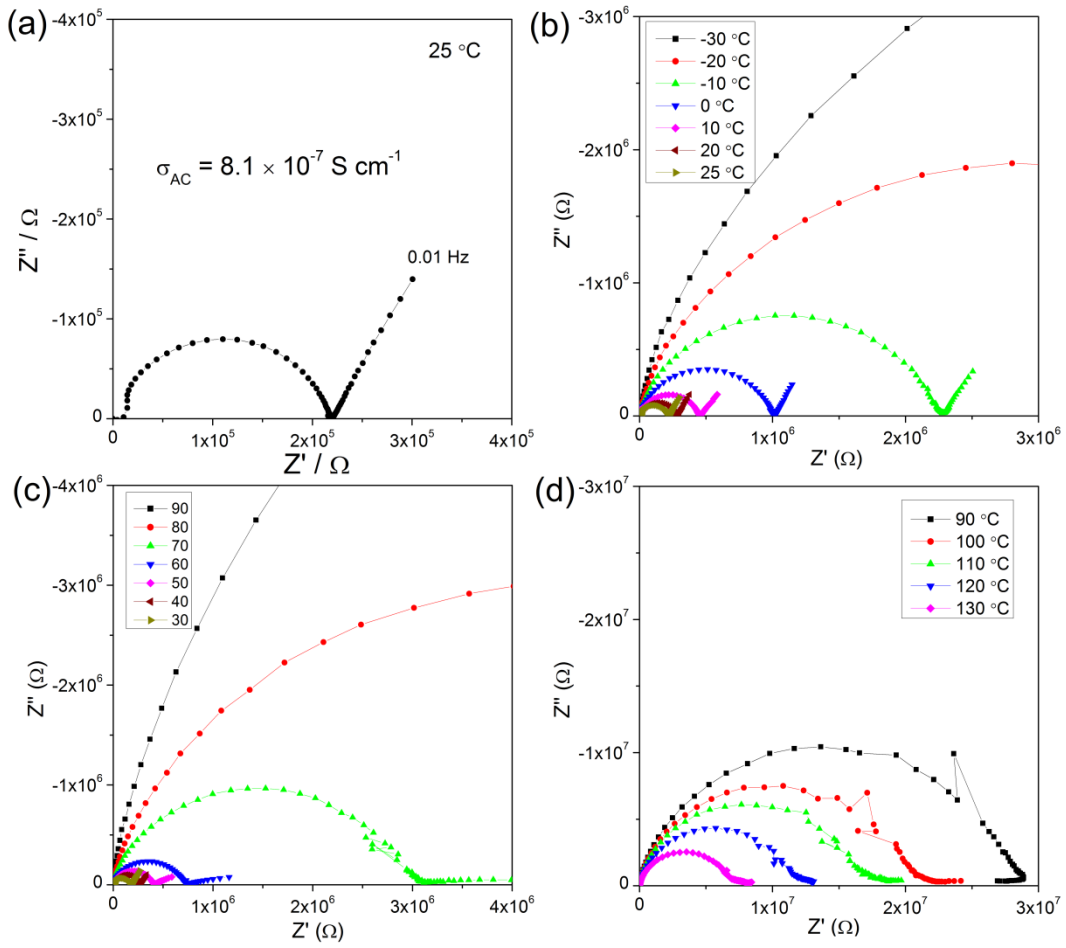

Fig. 5.3 Cole-Cole plots of impedance spectroscopy of Au/$LiVPO_4F$/Au specimen at (a) room temperature (25 ºC), (b) 30-25 ºC, (c) 30-90 ºC and (d) 90-130 ºC.

Fig. 5.3 (b) to (d) show the Cole-Cole plots of impedance spectroscopy recorded at various temperatures from –30-130 °C, while the temperature dependence of σ_{AC} is further summarized in Fig. 5.4. As well known, the conductivity of cathode materials normally increases with temperature following Arrhenius equation: $\sigma \propto \exp(-\Delta E/k_B T)$, where k_B is Boltzmann constant, T is the absolute temperature and ΔE is known as activation energy. σ_{AC} increases with temperature in the ranges of –30-30 ºC and 90-130 ºC, which agrees well with the Arrhenius equation. The

activation energy ΔE for $T > 90$ ºC and $-30 \leq T \leq 30$ ºC can be calculated to be 0.25 eV and 0.23 eV, respectively. However, σ_{AC} of $LiVPO_4F$ exhibits abnormal temperature dependence in the range of 30-90 °C. As can be seen, σ_{AC} declines by more than 2 orders of magnitude and then reaches the bottom at ~90 ºC. Since the ionic conductivity is supposed to be the major part of σ_{AC}, this phenomenon should be more related to the change of ionic transport rather than electronic conductivity. As shown in Fig 5.3(c), the slope of the straight line tail that is driven by ionic diffusion declines gradually in temperature range of 30-90 °C. This is obviously different from the conductivity decrease for T < 25 °C as shown in Fig. 5.3 (b). Furthermore, the diffusion tail finally fades away at 90 ºC, showing an electronic dominant transport behavior. Although the detailed mechanism of this abnormal temperature dependence of electrical conductivity is still not very clear at this moment, we speculate that a second-order phase transition might take place, which may largely alter the distribution of Li^+ in split sites and therefore greatly impairs ionic conduction. Further verifications and deep investigations on this interesting phenomenon are now still ongoing.

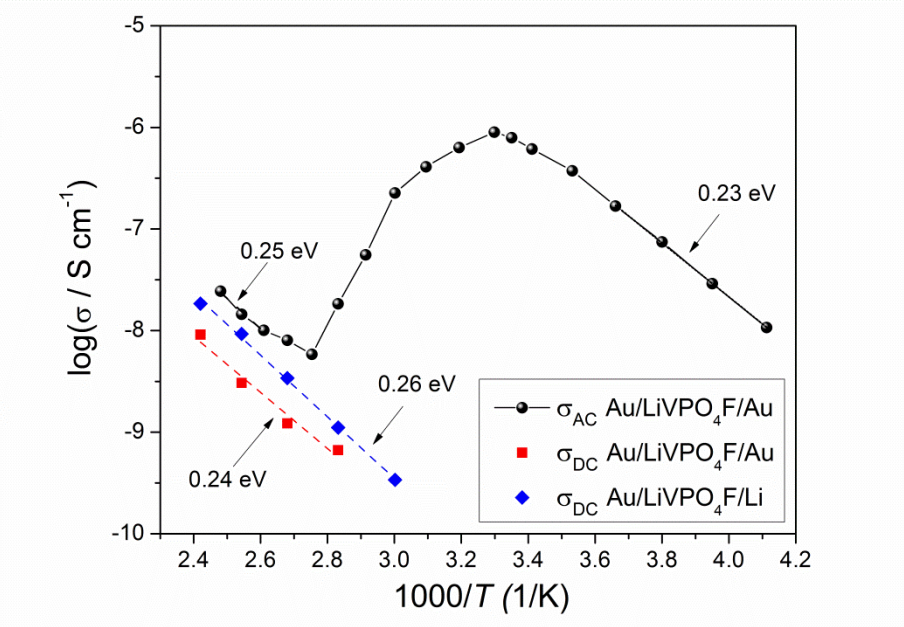

Fig. 5.4 Temperature dependence of the measured σ_{AC} and σ_{DC} of $LiVPO_4F$.

Electronic conductivity σ_{DC} of bulk $LiVPO_4F$ was derived through direct-current (DC) polarization using ionic-blocking disc specimens of Au/$LiVPO_4F$/Au. The electronic conductivity was also measured following Hebb-Wagner (H-W) method [159] using Au/$LiVPO_4F$/Li specimens, as the impedance spectroscopy suggests that the electrons should be minor charge carriers when compared to ions at room temperature. σ_{DC} is very close to σ_{AC} for T > 90 ºC, supporting our deduction that ionic conduction loses its ascendancy for T > 90 ºC. The activation energy for σ_{DC} obtained from ionic-blocking method and the H-W method is 0.24 eV and 0.26 eV respectively, also approximate to that (0.25 eV) obtained from σ_{AC}.

The σ_{DC} results imply an low electronic conductivity of only ~10^{-11} S cm^{-1} at room temperature, considerably lower than that of olivine $LiFePO_4$ (1.78× 10^{-9} S cm^{-1} [45]) and far lower than those of oxides cathode materials such as $LiCoO_2$ (~10^{-3}-10^{-1}

S cm^{-1} [7]) and $LiMn_2O_4$ (~10^{-5}-10^{-4} S cm^{-1} [14]). The conductivity results suggest that tavorite $LiVPO_4F$ should be an electronic insulator but a relatively fast Li^+ ionic conductor at room temperature, in consistence with the crystal structure analysis. This electronic insulating nature will doubtlessly hinder the electrochemical reaction for the pristine $LiVPO_4F$. On the other hand, the $LiVPO_4F$/C composite has a matrix electronic conductivity of 6.5×10^{-2} S cm^{-1} at room temperature, 6 orders higher than that of carbon-free $LiVPO_4F$. Although this value does not reflect the intrinsic electronic conductivity, it still suggests a greatly improved electronic transport of $LiVPO_4F$/C as in practical electrodes.

5.3 Electrochemical Properties

5.3.1 Galvanostatic charge-discharge

Electrochemical performances of $LiVPO_4F$ as cathode material were galvanostatically characterized. Fig 5.5 (a) shows the charge-discharge profile of the first cycle at a low rate of 0.1C (15 mAh g^{-1}). With prolonged constant voltage charge to 0.02C, $LiVPO_4F$ has initial charge capacity of 147 mAh g^{-1} but only 122 mAh g^{-1} reversible discharge capacity. On the contrary, $LiVPO_4F$/C has not only a high initial capacity of 153 mAh g^{-1} (carbon content subtracted), but also high reversible discharge capacity of 142 mAh g^{-1}. The voltage hysteresis between charge and discharge plateaus of $LiVPO_4F$/C is also noticeably narrower than that of carbon-free $LiVPO_4F$, owing to its better electronic transport.

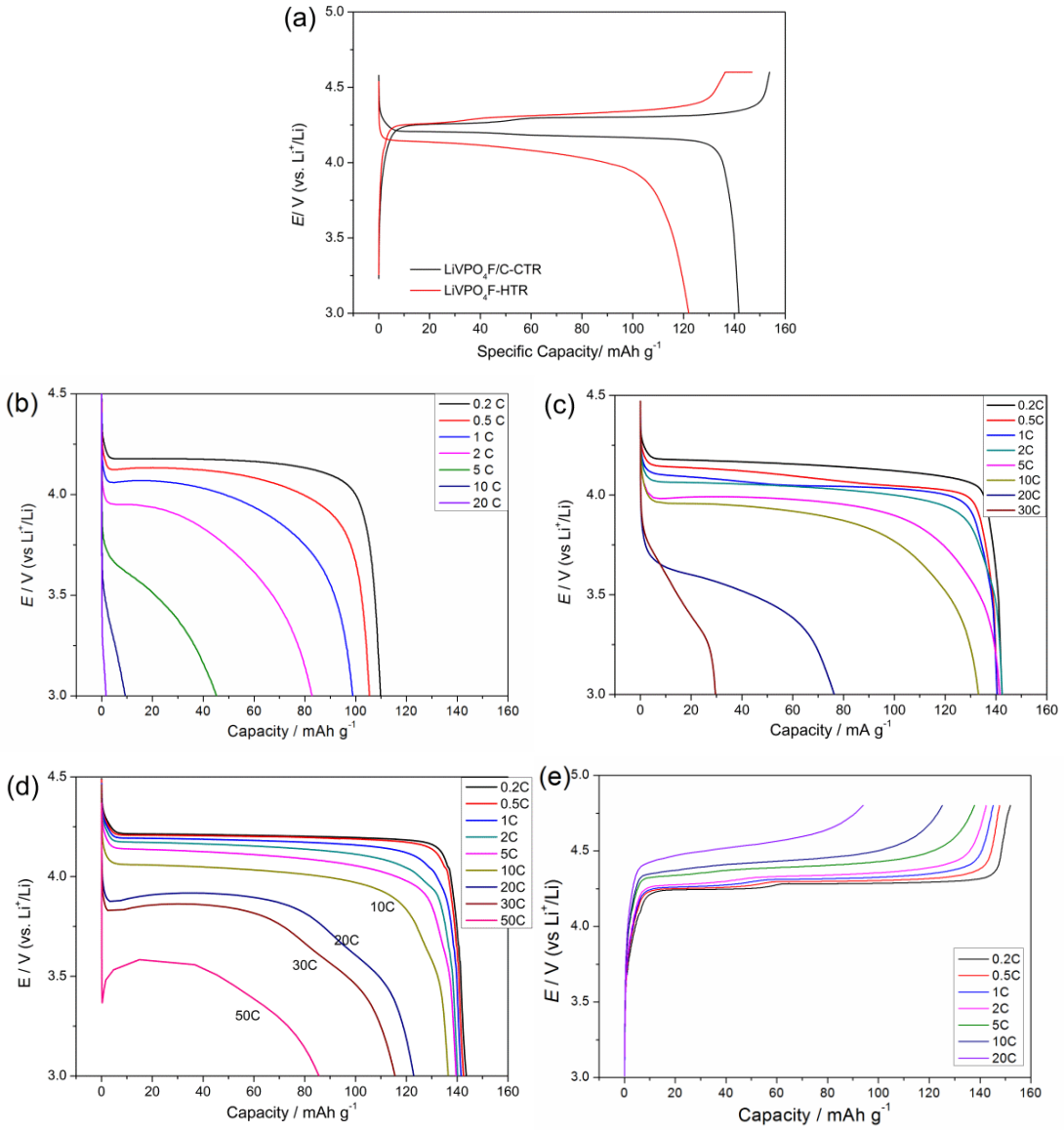

Fig 5.5 (a) Specific capacity, and rate capability of $LiVPO_4F$ and $LiVPO_4F/C$: (b) $LiVPO_4F$, (c, d, e) $LiVPO_4F/C$;

Fig 5.5 (b) and (c) show discharge rate capabilities of $LiVPO_4F$ and $LiVPO_4F/C$. The active material loading density is about 4 mg cm^{-2}. Half-cells were charged to 4.6 V and then directly discharged to 3 V in a constant current (CC) mode. $LiVPO_4F$ can only deliver 110 mAh g^{-1} capacity at a low discharge rate of 0.2C. Only 40% and 8% of its 0.2C specific capacities can be utilized at 5C and 10C, respectively. The low specific capacity and poor rate capabilities are caused by low electronic conductivity, large

particle size (~400 nm) and significant agglomeration. On contrary, $LiVPO_4F$/C delivers a capacity of 141 mAh g^{-1} at 0.2C and amazing high rate performance up to 10C. For example, a capacity of 140 mAh g^{-1} (99% of its 0.2C specific capacity) can be achieved at 5C, while 129 mAh g^{-1} can be delivered at 10C. Apparently, $LiVPO_4F$/C shows much improved rate capabilities due to the largely enhanced electronic transport. Strong polarization arose abruptly above 20C, resulting in low capacities. To explore the ultra-high rate capabilities of $LiVPO_4F$, thin electrodes with low active loading density (~2 mg cm^{-2}) were prepared. As shown in Fig 5.5 (c), thin electrode $LiVPO_4F$/C exhibits exceptionally high rate performances. A discharge capacity of 123 mAh g^{-1}, 85% of its specific capacity, can be achieved at 20 C, while 86 mAh g^{-1} can still be utilized at 50 C. This improvement in high-rate capability is attributed to reduced polarization resistance of electronic and ionic transport in thin electrodes. The results of thin electrode have demonstrated that the $LiVPO_4F$ lattice is capable of ultra-fast Li^+ insertion, while the transport and polarization in electrode are the main obstacles.

In addition to the amazingly high power performance, $LiVPO_4F$/C is also capable of rapid charge, which is a very favorable feature in practical applications. $LiVPO_4F$/C half-cells can be charged to more than 80% state of charge (SOC) at 10C (about 5 min). To characterize its stability upon fast charge, long-term cyclic tests were performed under constant current-constant voltage (CCCV) charge mode. In this CCCV mode, the cells were charged at a constant current of 10 C to 4.5 V followed by constant voltage charge for additional 5 min or 2 min, making the total charge duration to ~10 min and ~6

min respectively. Thereafter, the charged cells were discharged at a relatively slow current rate of 1 C. Fig 5.6 shows the discharge capacity as a function of cycle number in the cyclic tests. For the cell charged at constant voltage for 5 min， discharge capacity increases with cycle number at first and reaches the maximum of ~140 mAh g^{-1} after a few cycles of "activation". After that, the capacity fades very slowly with cycles. After 500 cycles, the half-cell could still deliver a capacity of ~130 mAh g^{-1}, 93% of the maximum capacity. For the cell charged for 2 min at constant voltage, the maximum capacity is ~120 mAh g^{-1}, while ~100 mAh g^{-1} capacity can be retained after 500 cycles. The high potential $LiVPO_4F$ shows very good stability with electrolyte even in fast charge and long-term cycling.

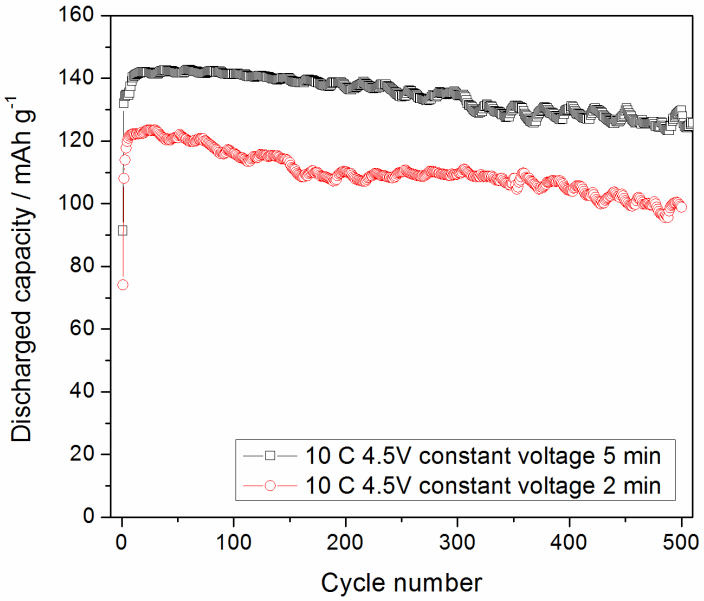

Fig 5.6 Cyclic performance of $LiVPO_4F/C$ at room temperature

As indicated in the conductivity analysis, the ionic conductivity of $LiVPO_4F$ subsides in the temperature range of 30-90 ºC, which may affect battery performances

in practical applications. In addition, the stability of electrolyte with this high potential cathode is also questionable at elevated temperature. To clarify these problems, electrochemical properties of $LiVPO_4F/C$ half-cells at reasonably elevated temperatures (40 and 55 ºC) were characterized and shown in Fig. 5.7. As shown in the Nyquist plots of EIS Fig. 5.7 (a), the charge-transfer resistance reduces with the increasing temperature from 25 ºC to 55 ºC. As shown in the CV profiles of Fig. 5.7 (b), the cathodic and anodic peaks are also much sharper with smaller peak separation at 55 ºC. The specific capacity and discharge capability at 55 ºC are both slightly better than those at 25 ºC. The voltage plateaus at high current rates (5C and 10C) are also noticeably higher owing to the reduced polarization. The enhanced electrochemical properties at elevated temperature can be ascribed to the increased electronic conductivity, boosted electrolyte fluidity/conductivity and enhanced surface activity. In general, the decrease in ionic conductivity has no obvious adverse effects on the electrochemical properties of $LiVPO_4F/C$ in practice.

The cyclic tests were carried out following exactly the same CCCV protocol as at room temperature. The maximum capacity was of 144 mAh g^{-1}, slightly higher than that obtained at room temperature. The capacity fading is more significant at 55 ºC. After 500 cycles, the cell retained a discharge capacity of 101 mAh g^{-1}, corresponding to 70% of the maximum capacity. It is normal the cyclability of the high potential cathodes abates at elevated temperature due to the deteriorated electrolyte degradation.

As a 4V-class cathode, $LiVPO_4F$/C still offers a decent cyclic performance at 55 ºC when compared to $LiMn_2O_4$ and $LiMnPO_4$.

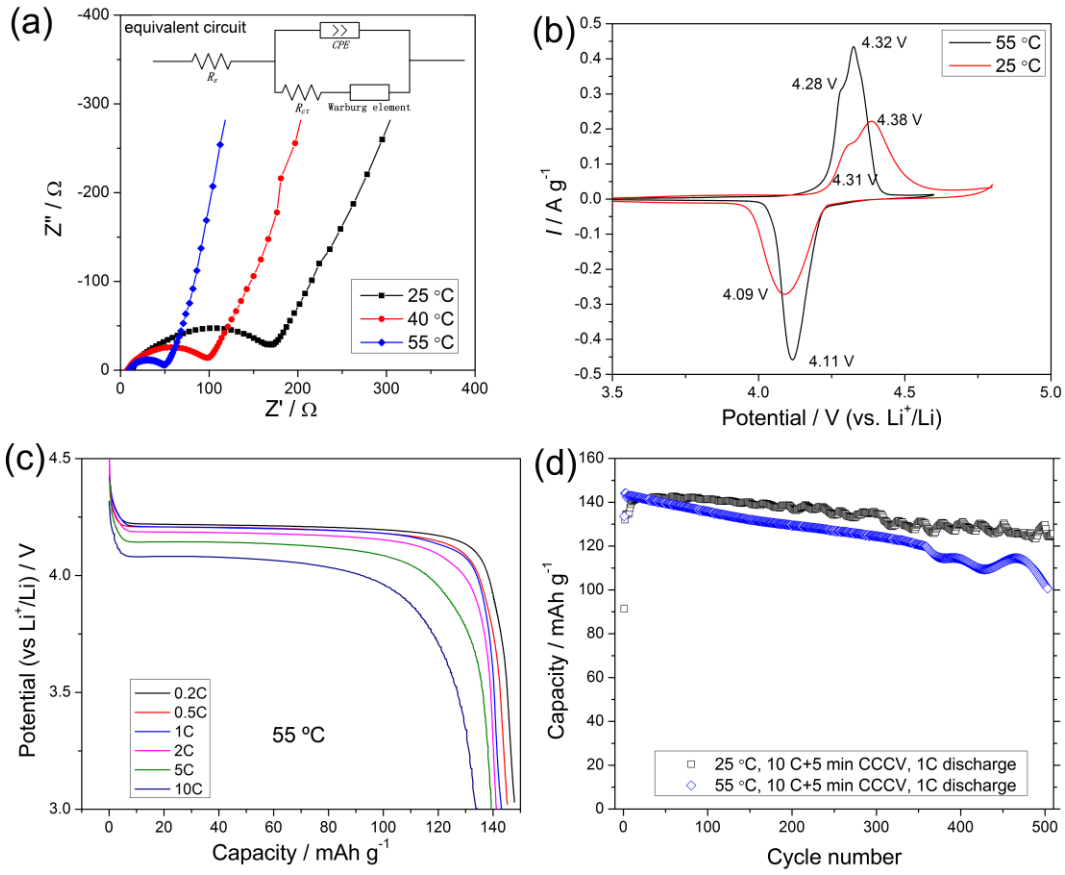

Fig. 5.7 Electrochemical properties of $LiVPO_4F$/C half-cells at elevated temperatures. (a) Nyquist-plot of EIS at 25 ºC, 40 ºC and 55 ºC, (b) cyclic voltammetry at 25 ºC and 55 ºC, (c) discharge rate capabilities at 55 ºC, and (d) cyclic performance at 55 ºC.

5.4 Li^+ extraction/insertion behavior

As shown in Fig. 5.5 (a), the flat discharge plateau evidently reflects a simple biphasic reaction similar to $FePO_4/LiFePO_4$, while the two distinct charge plateaus imply a distinctly different mechanism for Li^+ extraction. This phenomenon has been considered to be caused by the different energy states of split Li^+ sites in $LiVPO_4F$ lattice [121]. The fraction of the first charge plateau in the total charge capacity in this

work is ~0.25 for $LiVPO_4F$ and ~0.4 for $LiVPO_4F/C$, while it is ~0.3 for $LiVPO_4F/C$ synthesized via similar carbon thermal reduction [121, 124]. Furthermore, nanocrystalline $LiVPO_4F$ synthesized via sol-gel method has only one charge plateau [127]. On the other hand, $LiVPO_4F$ synthesized via ion exchanging has two discharge plateaus in addition to the two charge plateaus [126]. These facts suggest that Li^+ exaction/insertion mechanism in tavorite $LiVPO_4F$ depends greatly on the synthesis and processing route, possibly as a result of Li^+ occupancy variation in split sites.

Cyclic voltammetry (CV) and quasi-equilibrium open circuit potential (OCP) indicate the chemical potential differences between the two domains in Li^+ extraction. Fig. 5.8 shows the CV spectra of $LiVPO_4F/C$ and $LiVPO_4F$ measured at 0.2 mV s^{-1}. For $LiVPO_4F/C$, sharp anodic peaks at 4.380 V and 4.309 V correspond to two oxidization reactions with a potential difference of ~70 mV. Only one sharp cathodic peak at 4.084 V was observed in the Li^+ insertion process. In addition, the CV spectra also indicate that the carbon coating in $LiVPO_4F/C$ significantly reduces electrode polarization. The potential hysteresis of $LiVPO_4F/C$ is 296 mV, much lower than that (515 mV) of $LiVPO_4F$.

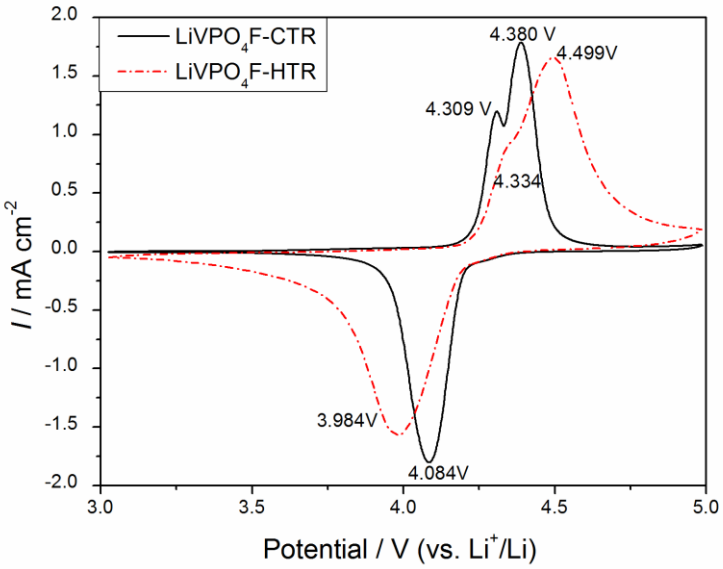

Fig. 5.8 Cyclic voltammetry of $LiVPO_4F$ and $LiVPO_4F/C$

Fig. 5.9 shows the quasi-equilibrium open circuit potential (OCP) of $Li_{1-x}VPO_4F$ obtained from GITT. In Li^+ extraction, OCP of $Li_{1-x}VPO_4F$ electrode remains almost constant at about 4.234 V with x from ~0.1 to ~0.4, and about 4.254 V with x from ~0.4 to ~0.9. This indicates a difference of ~20 mV in OCP between the two domains. Moreover, the OCP profile at x~0.4 in extraction process shows a single-phase behavior, implying that a third phase $Li_\gamma VPO_4F$ (γ~ 0.6 for $LiVPO_4F/C$) is present in addition to lithium-poor VPO_4F and lithium-rich $LiVPO_4F$. Therefore, the Li^+ extraction process may be comprised of two stages of biphasic reactions, $LiVPO_4F/Li_{0.6}VPO_4F$ (reaction A) and $Li_{0.6}VPO4F/VPO_4F$ (reaction B). In Li^+ insertion process, OCP remains constant ~4.225 V, confirming a simple biphasic reaction of $VPO_4F/LiVPO_4F$ (reaction C).

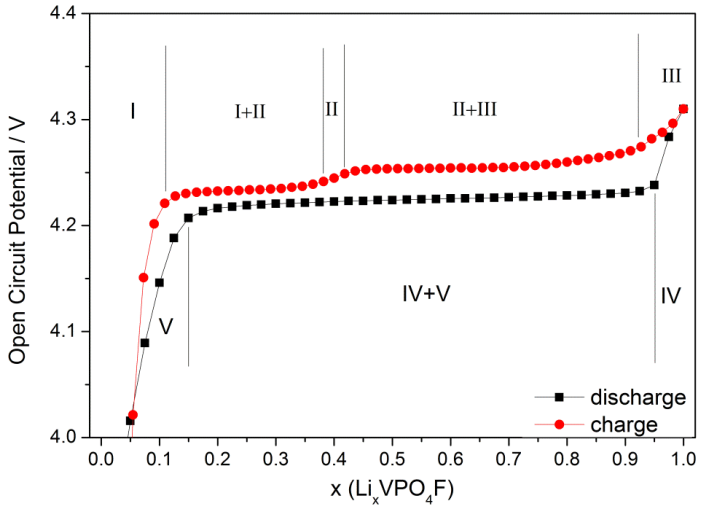

Fig. 5.9 Open circuit potential of $LiVPO_4F$ as a function of state of charge-discharge

Fig. 5.10 shows the *ex-situ* XRD patterns of $Li_{1-x}VPO_4F$ electrodes at different Li^+ extraction and insertion level. Two distinct phases, namely pristine $LiVPO_4F$ and "fully" charged phase VPO_4F can be observed from the XRD spectra. In the first stage of Li^+ extraction when x is smaller than 0.4 in $Li_{1-x}VO_4F$, only reflections from $LiVPO_4F$ were found, implying no change in the crystal structure of $LiVPO_4F$. Reflections from the VPO_4F phase starts to appear from $x > 0.4$ in the second stage of Li^+ extraction, where both $LiVPO_4F$ and VPO_4F coexist. As Li^+ extraction proceeds, intensity of $LiVPO_4F$ reflection reduces gradually accompanied with increase in the intensity of VPO_4F. LiVPO4F phase completely disappeared at a fully charged state with $x\sim 1$. The structural evolution during extraction is a possible reason for the potential differences between the two charge plateaus. Reflections from both VPO_4F and $LiVPO_4F$ were observed during the entire Li^+ insertion process, indicating a simple $VPO_4F/LiVPO_4F$ biphasic reaction. Intensity of VPO_4F reflections decays with Li^+ insertion proceeding until complete transformation to $LiVPO_4F$.

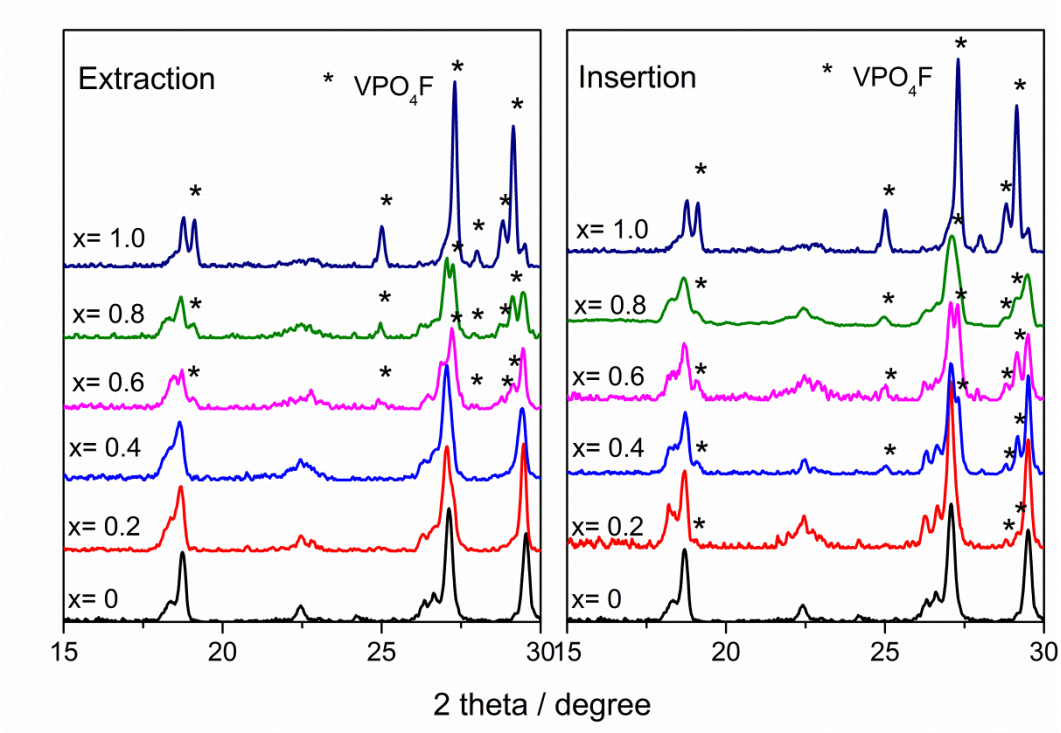

Fig. 5.10 *Ex-situ* XRD of $Li_{1-x}VPO_4F$ electrode in extraction and insertion.

5.5 Li^+ diffusion behavior

Li^+ diffusion coefficients of at different Li^+ extraction/insertion levels of $Li_{1-x}VPO_4F$ were determined using GITT, EIS and CV techniques. In the electrochemical study of diffusion coefficients, it is essential and crucial to accurately estimate the active contact surface area, *S*, between electrode and electrolyte. Herein *S* was determined to be 1.18 m^2 g^{-1} based on Brunauer-Emmett-Teller (BET) measurement. The $LiVPO_4F$/C powder was heated at 500 °C for 10 min to remove the carbon content. The BET surface area was then measured with the leftover $LiVPO_4F$ powder. XRD results confirmed that the leftover $LiVPO_4F$ still kept the structure of tavorite without oxidation.

5.5.1 Galvanostatic intermittent titration technique

GITT was used to evaluate the diffusion coefficient (D_{GITT}) of electrode materials. In each titration step of GITT, a current pulse of 37.5 mA g^{-1} (0.25 C) is applied for 300 s followed by an open circuit relaxation for 90 min. From GITT measurement, diffusion coefficient of lithium ions was calculated based on Equation 5.1 developed by Weppner et al.[160]:

$$D_{\mathrm{Li}} = \frac{4}{\pi}\left(\frac{V_M}{SF}\right)^2 \left(I_0 \frac{\delta E_S/\delta x}{\delta E/\delta t^{1/2}}\right)^2 \; at\; t \ll \tau \qquad \text{Equation 5.1}$$

where V_M is molar volume (5.2346×10^{-5} m^3 mol^{-1}), S is the electrode surface area (1.18 m^2 g^{-1}), F is the Faraday's constant (96,485.3365 C mol^{-1}), I_0 is the pulse current (0.0375 A g^{-1}), $\delta E/\delta x$ is the slope of the equilibrium open circuit potential (OCP) versus lithium content which can be obtained from the differential of the OCP curve shown in Fig. 5.11 (a), and $\delta E/\delta t^{1/2}$ is the slope of initial transient voltage change versus square root of time. Fig. 5.11 (b) shows an example of initial transient voltage change of E vs. $t^{1/2}$ plot recorded for $Li_{0.5}VPO4F$ during insertion process. As can be seen, the transient voltage E exhibits a linear behavior versus square root of time in the first 60 s. The experimental data points can be linearly fitted with a slope of $\delta E/\delta t^{1/2}$= 0.00443 V s^{-1}. Fig. 5.11 (c) shows the lithium ion diffusion coefficients calculated using Equation 5.2 as a function of x in $Li_{1-x}VPO_4F$. Lithium ion diffusion coefficients calculated at different values of x were from ~ 10^{-18} cm^2 s^{-1} to ~ 10^{-12} cm^2 s^{-1} with disordered "W" and "U" shapes for extraction and insertion, respectively.

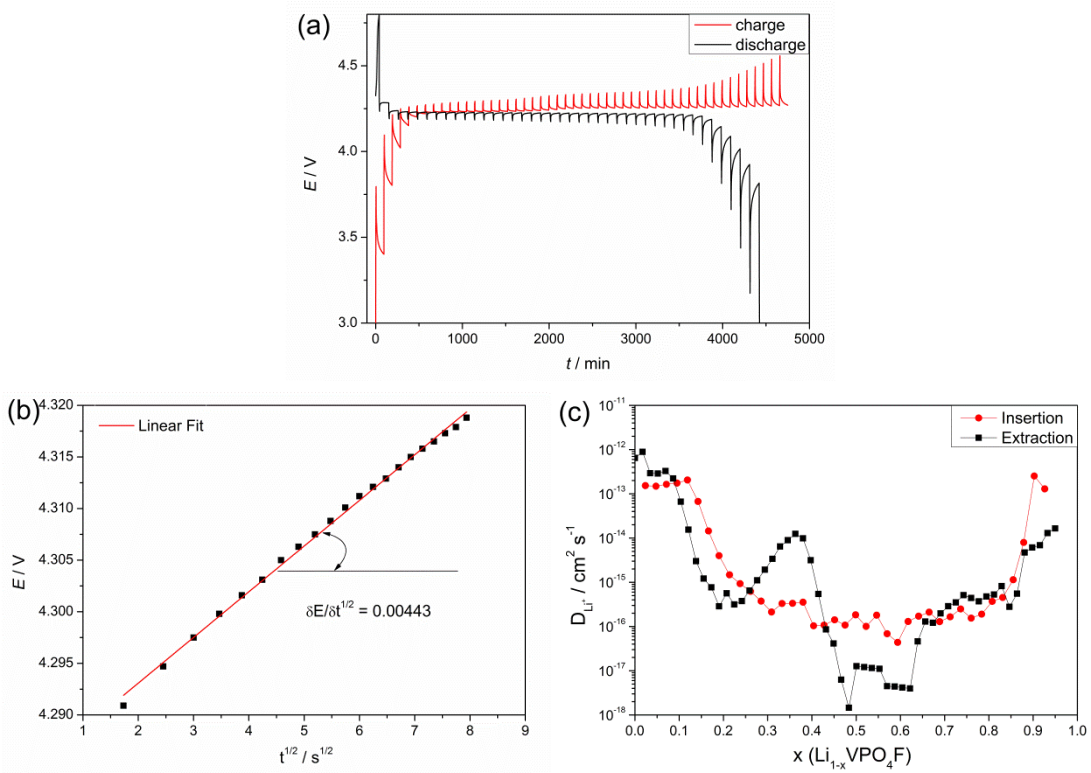

Fig. 5.11 Diffusion coefficient measurement via GITT; (a) GITT profile of $LiVPO_4F$ half-cell, (b) an example of titration curve at x~ 0.5, and (c) DGITT of $Li_{1-x}VPO_4F$ as a function of x

5.5.2 Electrochemical impedance spectroscopy

EIS was also used to study the lithium diffusion behavior of $Li_{1-x}VPO_4F$ at different extraction/insertion level x, with a step of x~ 0.1. EIS was carried out with a 5 mV amplitude vs. open circuit potential within frequency range from 1 MHz to 1 mHz. Prior to EIS tests, the cell was held at open circuit for 4 h to achieve the quasi equilibrium state.

Fig. 5.12 (a) compares the Nyquist plots of $Li_{1-x}VPO_4F$ between extraction and insertion process. At very low frequency, the impedance behavior is mainly driven by diffusion in the bulk electrode material or the so-called Warburg impedance rather than charge transfer at the interfaces. Therefore, the diffusion coefficient can be calculated

using the following equation developed by Ho et al. [161]:

$$D_{Li} = 1/2[\frac{V_M(\delta E/\delta x)}{SFA_W}]^2 \qquad \text{Equation 5.2}$$

where V_M is molar volume, S is the specific electrode surface area, F is the Faraday's constant, $\delta E/\delta x$ is slope of the equilibrium OCP versus lithium content and A_w is known as Warburg factor. A_w can be obtained from the linear relationship of Z_{real} or $-Z_{img}$ versus inverse square root of angular frequency $\omega^{-1/2}$ when $\omega \rightarrow 0$. An example is shown in Fig. 5.12 (b), which reveals a good linear relationship between Z_{real} and $\omega^{-1/2}$ of $Li_{0.5}VPO_4F$ in low frequency range. Li^+ diffusion coefficient of $Li_{1-x}VPO_4F$ with different extraction or insertion level is finally calculated using Equation 5.2. The calculated diffusion coefficient D_{EIS} was found to be in the range from ~10^{-18} to ~10^{-12} $cm^2\ s^{-1}$ with a similar variation as that derived from GITT measurement.

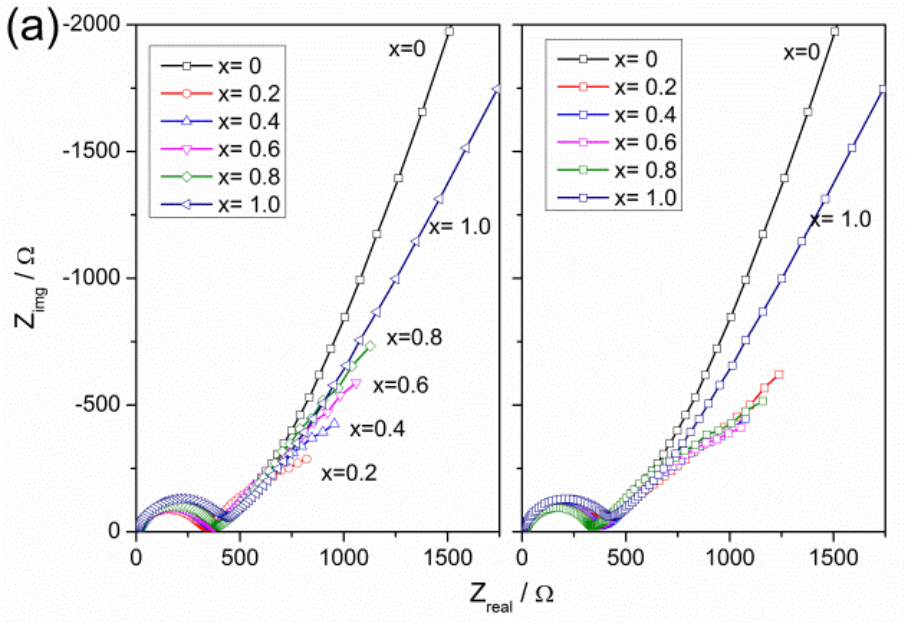

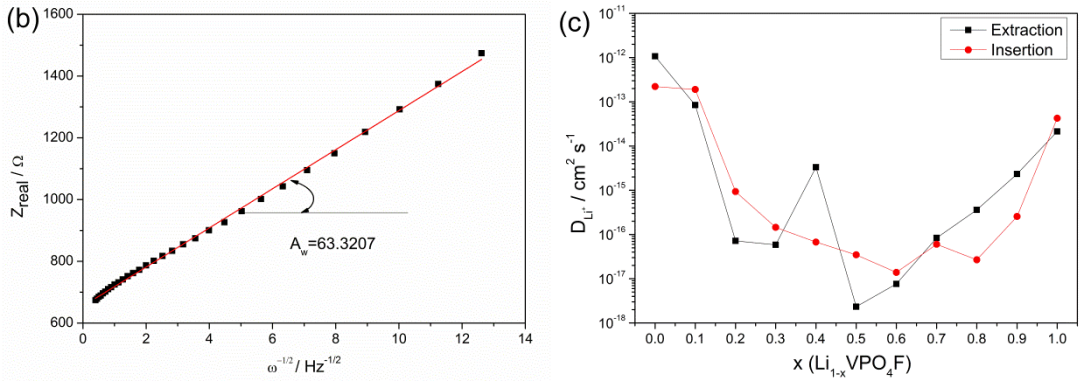

Fig. 5.12 Diffusion coefficient measurement via EIS; (a) Nyquist plots of $Li_{1-x}VPO_4F$/Li half-cell, (b) Z_{real} vs. $\omega^{-1/2}$ at extraction level of x~ 0.5 at low frequency range, and (c) diffusion coefficient of $Li_{1-x}VPO_4F$ calculated via EIS as a function of x

5.5.3 Cyclic voltammetry

Fig. 5.13 shows the CV profiles of $LiVPO_4F$/C with different voltage sweep rates from 0.2 mV s^{-1} to 5 mV s^{-1}. If lithium diffusion within electrode is the limiting factor rather than charge transfer across interfaces, Li^+ diffusion coefficient can be determined by the following equation [162]:

$$i_p = 0.4463\left(\frac{F^3}{RT}\right)^{1/2} n^{3/2} S D^{1/2} C_0^* v^{1/2} \qquad \text{Equation 5.3}$$

where i_p is the peak current of the redox reaction, F is Faraday's constant, R is the molar gas constant (8.314472 m^2 kg s^{-2} K^{-1} mol^{-1}), T is the absolute temperature, n is the number of electrons involved in the electrochemical reaction, S is the electrode surface area, D is Li^+ diffusion coefficient, C_0^* is the initial Li^+ concentration and v is the sweep rate. Initial concentration of lithium ions was calculated to be 1.903×10^4 mol m^{-3} according to refined $LiVPO_4F$ cell volume (174.6 $Å^3$). The inset in Figure 5.11 shows the linear relationships between peak currents and the square root of sweep rates. Hence, the apparent diffusion coefficients corresponding to the three electrochemical

reactions can be calculated to be D_{app}(A) = 5.6×10^{-13} cm^2 s^{-1}, D_{app}(B) = 1.8×10^{-12} cm^2 s^{-1} and D_{app}(C) = 1.3×10^{-12} cm^2 s^{-1}. Diffusion coefficient D_{app}(A) corresponding to reaction A was lower than D_{Li}(B) of reaction B, indicating a relatively inferior diffusion kinetics during reaction A.

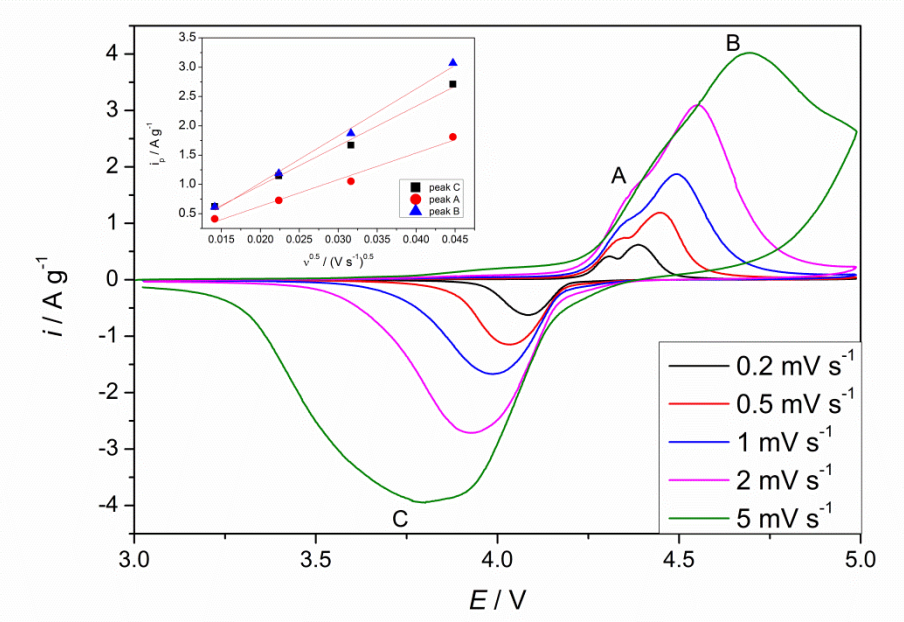

Fig. 5.13 Cyclic voltammetry of $LiVPO_4F$ half-cell with different sweep rates; Inset shows the relationship between peak currents and square root of sweep rates.

5.5.4 Discussion on D_{Li}^+ with phase transformation

As shown above, the diffusion coefficient calculated in biphasic domains are significantly lower by up to 6 orders than those measured in single phase domains. GITT and EIS have been developed based on several idealizations and assumptions with Frumkin isotherm model without consideration of interphase strain-stress, phase boundary movement and interphase mobility in phase transition materials. It is apparent to find that $\delta E/\delta x$ in Equation 5.1 and Equation 5.2 approximates zero in the

biphasic domain where the equilibrium potential OCP is almost constant with *x*. Therefore, diffusion coefficients calculated in biphasic domain are much smaller. This problem has been addressed by some recent reports that attempt to include phase transition kinetics into the calculation [163, 164]. However, diffusion coefficients are still well estimated for each phase in single-phase domains, while the diffusion behavior in biphasic domain can be derived from those in the two phases. Hence, diffusion coefficients calculated in single-phase domain are of important significance.

Fig. 5.14 compares the diffusion coefficients measured using GITT and EIS as a function of quasi-equilibrium OCP. As can be seen, D_{EIS} and D_{GITT} are in very good agreement with each other. The calculated diffusion coefficients are almost constant with *x* in each single-phase domain. D_{Li} of lithium rich $LiVPO_4F$ is in the range of 1.5×10^{-13}- 1.1×10^{-12} cm^2 s^{-1}, while D_{Li} of lithium poor VPO_4F phase is in the range of 2.1×10^{-14}- 2.5×10^{-13} cm^2 s^{-1}. D_{Li} of $Li_{\sim0.6}VPO_4F$ is the lowest (3.3×10^{-15}-1.2×10^{-14} cm^2 s^{-1}) compared to the other two phases. D_{app} (~10^{-12} cm^2 s^{-1}) measured from CV is slightly higher than D_{GITT} and D_{EIS} by less than one order. In general, the diffusion coefficient of $LiVPO_4F$ (10^{-13}-10^{-12} cm^2 s^{-1}, lithium rich phase, this work) is 2 orders higher than that of olivine $LiFePO_4$ (10^{-15}-10^{-14} cm^2 s^{-1}[47]), indicating a facile Li^+ diffusion in tavorite lattice.

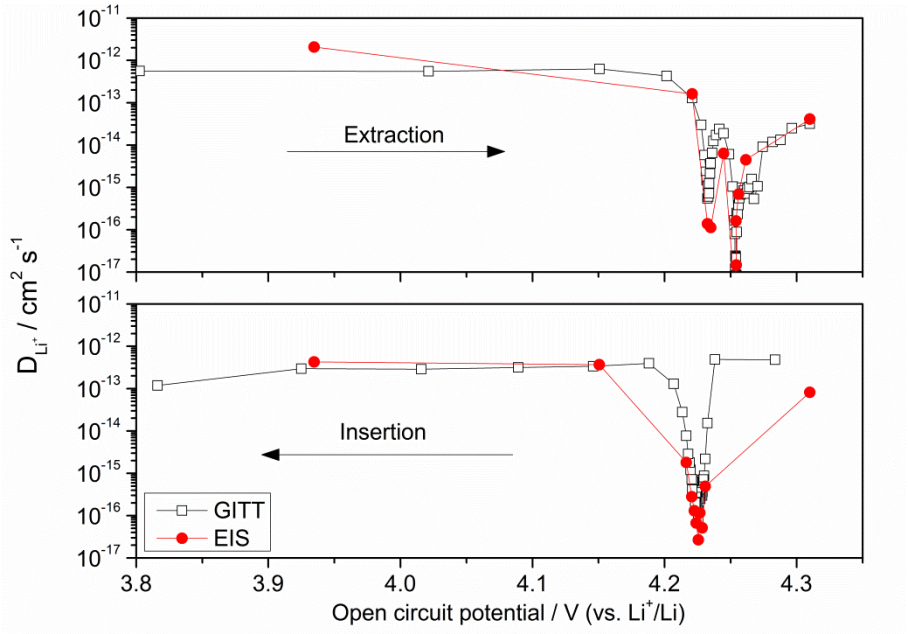

Fig. 5.14 Diffusion coefficient measured via GITT and EIS as a function of open circuit potential

Summary

In summary, high performance $LiVPO_4F$/C has successfully been developed. Some essential electrical and electrochemical properties of this material are revealed in this Chapter. Tavorite lattice seems to be a relatively faster Li^+ ionic conductor when compared to olivine lattice. $LiVPO_4F$ has an electrical conductivity of 8.1×10^{-7} S cm^{-1} at room temperature. Poor electronic transport restricts the electrochemical performance of tavorite $LiVPO_4F$. Electronic conductivity of pristine $LiVPO_4F$ is only 1.5×10^{-8} S cm^{-1}. By coating carbon on the particle surface, electrochemical properties can be dramatically improved. Carbon coated $LiVPO_4F$/C exhibits amazingly high power performance, fast charge capability and very good stability in long-term cycling. Chemical diffusion coefficients at different extraction/insertion levels measured via

different techniques are in good agreement. Li^+ diffusion coefficient of tavorite $LiVPO_4F$ (lithium rich phase) is 10^{-13}-10^{-12} cm^2 s^{-1}, 2 orders higher than that in olivine materials. The intermediate phase $Li_{\sim 0.6}VPO_4F$ in extraction seems to have a relatively inferior Li^+ diffusion property, which may be another limiting factor for thorough Li^+ extraction. These findings in this chapter may greatly contribute to the further research and engineering of the tavorite cathode materials.

6 A novel synthesis route for nanostructured phosphates materials

Technology used in the fabrication of nanostructured phosphate materials strongly affects microstructure and morphology of the as-synthesized materials and hence their electrochemical performance. Porous-structured nanomaterial is of high significance in research of electrode materials in LIBs, because porous structure can facilitate the flow and infiltration of electrolyte. Therefore, a novel solution based synthesis route for producing nanostructured phosphates materials has been developed for the first time in this Chapter.

In a typical sol-gel synthesis route of $LiFePO_4$, citric acid or tartaric acid is normally used as chelating agents and/or carbon source, while phosphate salt or phosphoric acid are used as phosphorous source [96, 106, 148, 165, 166]. In this processing, phosphonate chelating agents which can also serve as in-situ phosphorous and carbon source simultaneously were adopted. Phosphonic groups have more desirable reactivity and chelating properties than those obtained with Lewis functional groups like carboxylate ($RCOO^-$) and amine (R_2N) groups in citric acid and EDTA. With amazing chelating abilities, phosphonate chelating agents have been widely used in medicine, industry and water treatment, as drug delivery agent, scaling inhibitor, detergents, settling retarder and anti-corrosion agents [167]. Furthermore, phosphonates chelating agents have crucial advantages as in-situ phosphorous and carbon source in synthesis of phosphates materials. There are actually very few works regarding their

applications in the synthesis of phosphate cathode materials, especially as chelating agents in sol-gel synthesis. Bauer et al. used $Fe[RPO_3]\cdot H_2O$ (*R* = methyl or phenyl group) to synthesize carbon rich $LiFePO_4$ via a traditional solid-state reaction [168]. Wang et al. prepared $LiFePO_4$/C composite via a complexion and pyrolysis route with HEDP ($CH_3C(OH)(H_2PO_3)_2$) [169]. Hill et al. fabricated porous and carbon rich $LiFePO_4$/C by applying SiO_2 template to a novel single molecular precursor with etidronic acid as chelating agents [170]. The present work has synthesized nanosize LiFePO4/C composites with a porous or hollow sphere architecture using a simple and template free sol-gel route.

6.1 Material Preparation

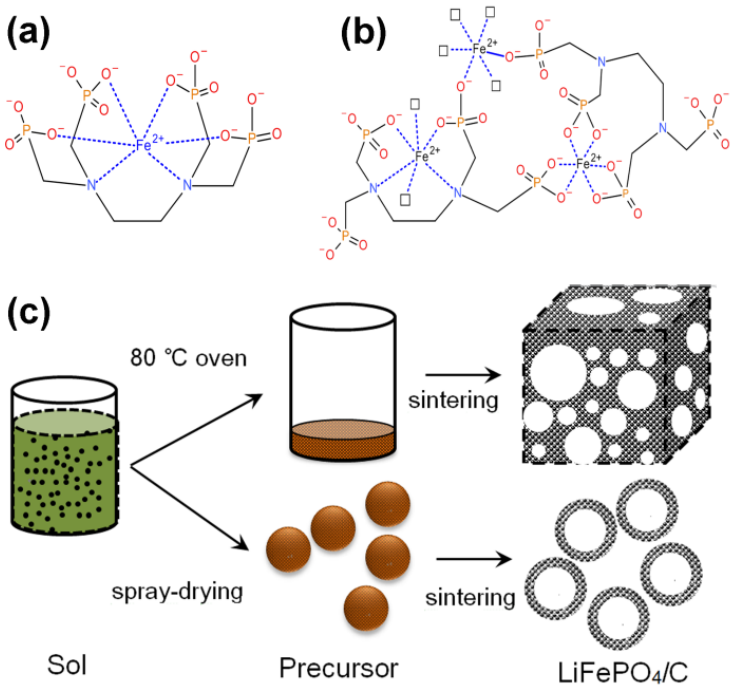

Fig. 6.1 Schematic of synthesis approach of porous and hollow spherical $LiFePO_4$; (a) proposed Fe-EDTMP 1:1 complex, (b) proposed polymeric reticulation complex of Fe-EDTMP, and (c) synthesis routes of porous $LiFePO_4$/C and hollow spherical $LiFePO_4$/C.

Among various types of phosphonate chelating agents, ethylenediaminetetra (methylene phosphonic acid) (EDTMP, $C_6H_{20}O_{12}N_2P_4$), a phosphonate analog of ethylenediaminetetraacetic acid (EDTA), was selected in this work due to several advantages. Firstly, EDTMP can chelate with many metal ions including alkaline earth metal ions and divalent transitional metal ions, thus enabling effectively synthesize many types of phosphate cathode materials. Secondly, as multidentate ligands with 4 phosphonic groups and 2 amine (R_2N) groups in a single molecular, stability of metal-EDTMP complex is considerably higher than other common phosphonate chelating agents [171, 172]; Thirdly, EDTMP may chelate metal ions to form polymer reticulation complex as a multi-ligand chelating agent, which is desirable for secondary architectural tailoring of the final products.

As illustrated in Fig. 6.1, porous $LiFePO_4$/C composites with secondary architectures were synthesized via template free sol-gel routes with EDTMP as chelating agent as well as in-situ phosphorous and carbon sources. Spray-drying was conducted in order to tailor micrometre sized sphere secondary particles. In a typical process, Iron (II) acetate was slowly dropped into 80 ºC aqueous solution of LiOH and EDTMP with rigid stirring. Dark green transparent sol was obtained with molar ratio of Li: Fe: P= 1: 1: 1. Ammonia solution was added to maintain an alkalescency environment. PH value is critical to dissolubility of Fe^{2+} and EDTMP. If PH < 5, protonation of phosphonic groups will inhibit complexion of Fe^{2+} and EDTMP and induce grey green precipitates of protonized EDTMP [171]. On the other hand, if PH exceeds 9.6, $Fe(OH)_2$ precipitates

will be more favourable than the Fe-EDTMP complexes. Ammonia itself may also contribute to the coordination of Fe^{2+}, since it is a coordination agent with relatively weaker effects. Fe-EDTMP complexes could be diversiform due to the multidentate nature of EDTMP. The simplest 1:1 Fe-EDTMP complex is shown in Fig. 6.1 (a). A complex polymer reticulation network may also be formed as proposed in Fig. 6.1 (b), especially upon gelling. All the elements will be thoroughly and uniformly distributed within the network in atomic level. Furthermore, the *in-situ* carbonization of EDTMP will form carbon matrix and restrict $LiFePO_4$ crystalline growth. No additional carbon source was introduced other than EDTMP. As shown in Fig. 6.1 (c), the stable sol was dried via a conventional sol-gel way or spray-drying. Porous $LiFePO_4$ and hollow spherical $LiFePO_4$ were finally obtained by pyrolysis of precursors in inert atmosphere.

6.2 Characterization

6.2.1 Crystal structure

Fig. 6.3 shows the X-ray diffraction (XRD) patterns of porous $LiFePO_4$, hollow $LiFePO_4$ and the precursor. According to XRD analysis, no crystalline phases can be found in the precursors, in line with the highly disordered xerogel structure proposed above. Both porous $LiFePO_4$ and hollow $LiFePO_4$ show a single olivine crystal structure with all reflections attributed to $LiFePO_4$ (*Pnma*, JCPDS 40-1499). Results from elemental analysis results show a molar ratio of Li: Fe: P = 0.985: 1: 1 in the final products, in good agreement with the designed composition. It is clear that all the

phosphonate groups (RPO_3^{2-}) in EDTMP have been completely transformed into phosphate (PO_4^{3-}) with the C-P bonds ruptured upon pyrolysis. Carbon contents in porous $LiFePO_4$/C and hollow spherical $LiFePO_4$/C were estimated by TGA to be 6.8 wt% and 7.1 wt%, respectively. Mean crystallite sizes of porous $LiFePO_4$/C and hollow spherical $LiFePO_4$/C were estimated to be 26 nm and 35 nm using Scherrer equation (Eq. 2.1). Hollow spherical $LiFePO_4$/C has a noticeably smaller crystallite size, since the spray-drying process significantly reduces the gelling duration and thus impede the particle growth upon gelling.

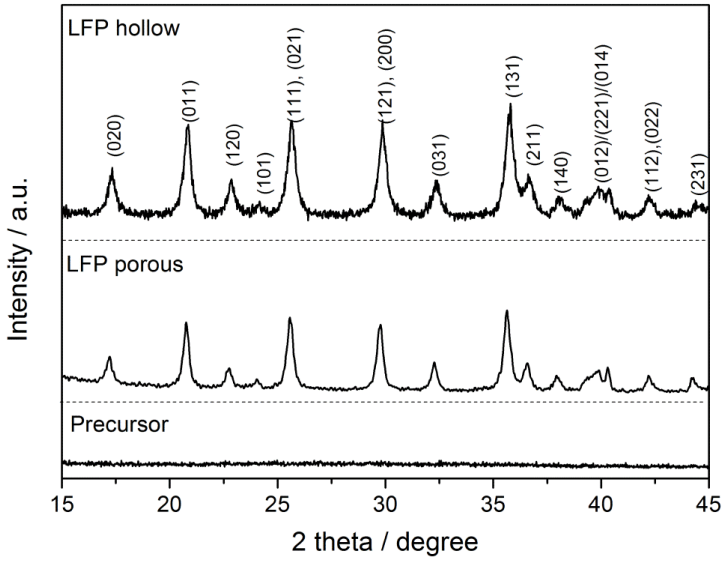

Fig. 6.2 XRD spectra of precursor, porous and hollow sphere $LiFePO_4$

6.2.2 Micromorphology

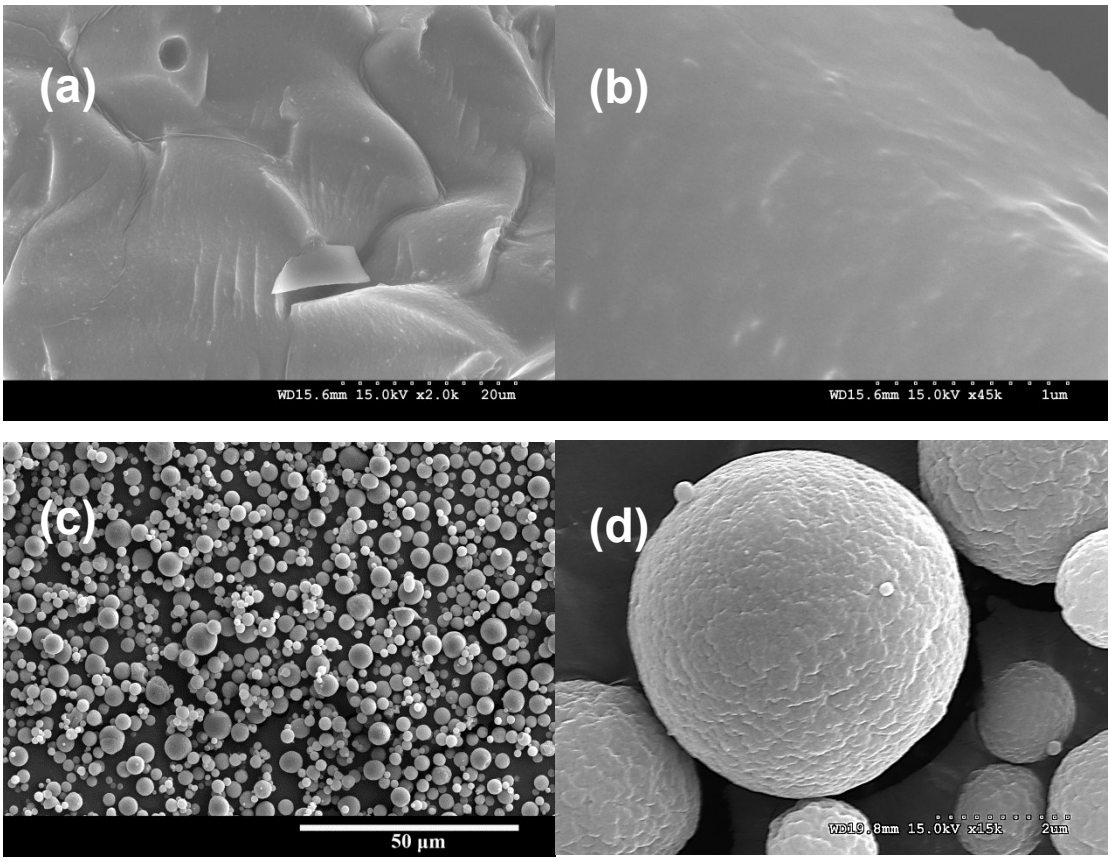

Fig. 6.3 Micromorphology of precursors to (a), (b) porous $LiFePO_4/C$ and (c), (d) hollow spherical $LiFePO_4/C$

SEM images of the precursors to porous $LiFePO_4/C$ and hollow spherical $LiFePO_4/C$ are shown in Fig. 6.3. The precursor to porous $LiFePO_4/C$ shows a typical uniform morphology of xerogel, without precipitate particles or ordered secondary structure. As for the sol-gel-spray-drying route, the precursor is comprised of discrete dense spherical particles of 1-5 μm in diameter.

Fig. 6.4 shows SEM images of porous $LiFePO_4/C$ and hollow spherical $LiFePO_4/C$. Low magnification SEM image reveals the highly porous network architecture in porous $LiFePO_4/C$. Dimensions of pores vary from tens of nano-meters

to several micro-meters with a random distribution. The micro-pores were interconnected by the nano-pores, forming 3d tunnels. In high magnification SEM image, it can be seen that the porous network consisted of nano-sized primary particles of ~30 nm in diameter. This spherical morphology was well maintained after sintering, whereas solid particles turned into hollow structured due to gas release upon pyrolysis. Nano-sized pores on the shell connect the inner hollow space with outside, which benefits electrolyte flowing and wetting. Fig. 6.4 (e) shows the cross section of the shell of a damaged hollow sphere particle. As can be seen, nano-particles of 20-30 nm in diameter comprise the ~180 nm thick shell, in good agreement with the SEM observations.

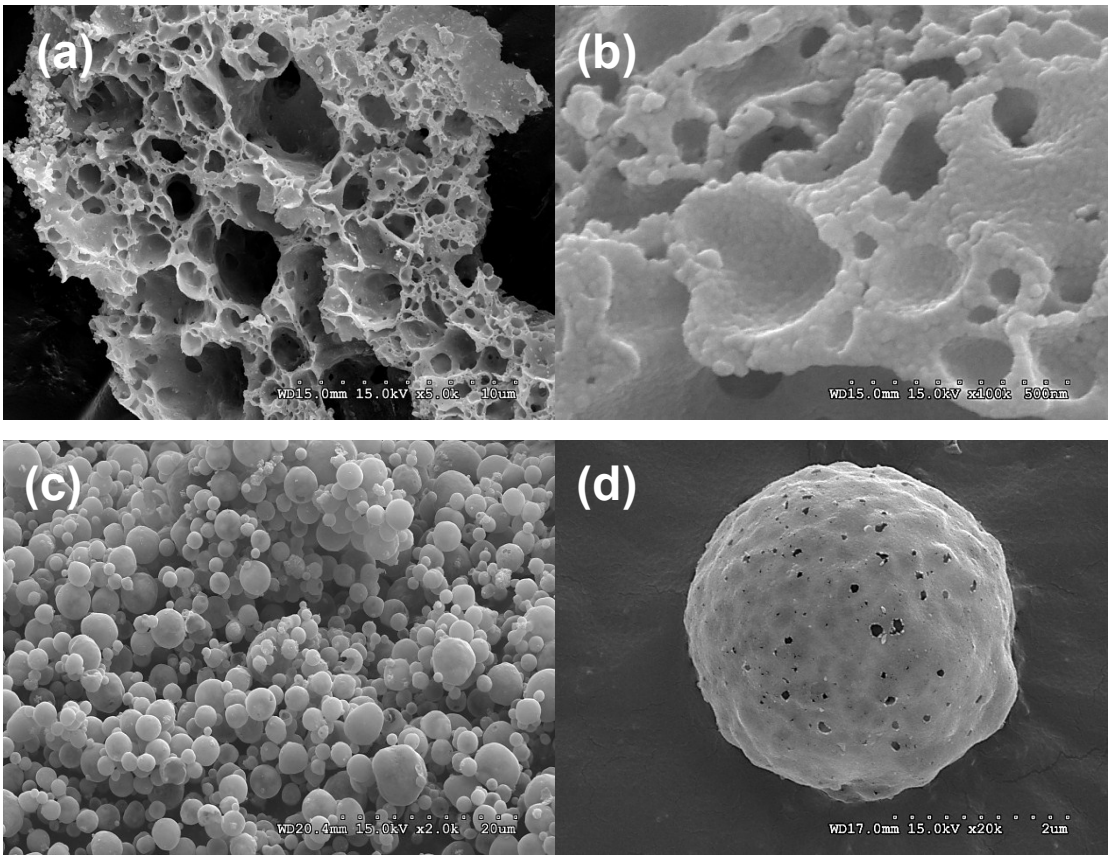

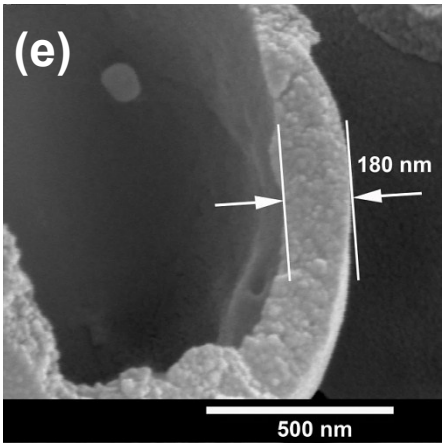

Fig. 6.4 SEM images of porous $LiFePO_4$/C and hollow spherical $LiFePO_4$/C; (a, b) porous $LiFePO_4$/C frameworks; (c, d) secondary particles of hollow spherical $LiFePO_4$/C; (e) a damaged secondary particle of hollow spherical $LiFePO_4$/C

Fig. 6.5 shows the TEM images of porous $LiFePO_4$/C and hollow spherical $LiFePO_4$/C. As can be seen in Fig. 6.5 (a), $LiFePO_4$ crystallite of ~35 nm was well wrapped up by thick amorphous carbon in porous $LiFePO_4$/C. The hollow spherical micromorphology was also revealed by TEM image as shown in Fig. 6.5 (b). Fig. 6.5 (c) and (d) shows core shell structured $LiFePO_4$/C nanoparticles as fine as ~10 nm on the shell of hollow spherical $LiFePO_4$/C, in consistent with SEM observations. High-resolution TEM image in Fig. 6.3 (d) reveals the carbon coating morphology. As can be seen, $LiFePO_4$ crystallite ~15 nm in diameter is coated by an amorphous carbon layer ~2 nm thin.

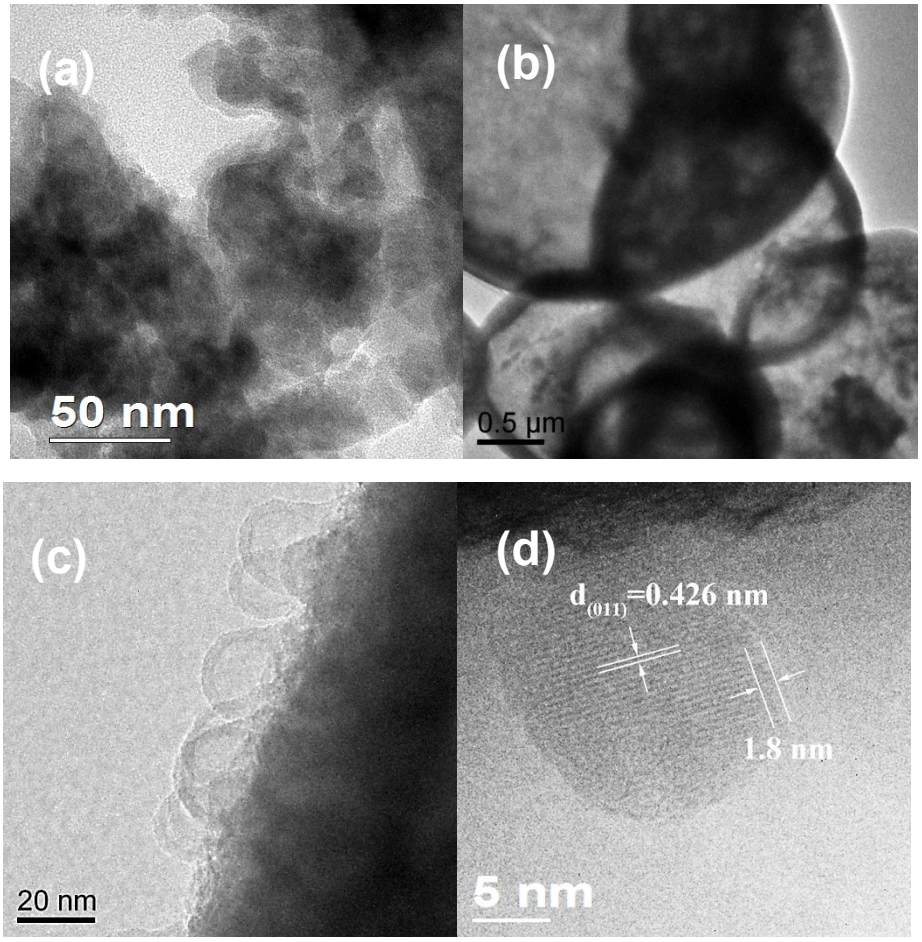

Fig. 6.5 TEM images of porous and hollow sphere $LiFePO_4$
(a) porous $LiFePO_4$, (b, c, d) hollow sphere $LiFePO_4$

6.2.3 Raman spectra

Fig. 6.6 shows the Raman spectra of pristine $LiFePO_4$ and hollow spherical $LiFePO_4$/C synthesized with EDTMP. The D-band at 1355 cm^{-1} and G-band at 1577 cm^{-1} confirm that the carbon coating should be in amorphous form. Ratio of I_D/I_G of hollow sphere $LiFePO_4$/C synthesized with EDTMP is 0.97. The relatively high I_D/I_G ratio indicates the highly disorder carbon, therefore the electronic conductivity of the carbon resulted from EDTMP is expected to be relatively lower than that of $LiFePO_4$-PPG as described in Chapter 4.

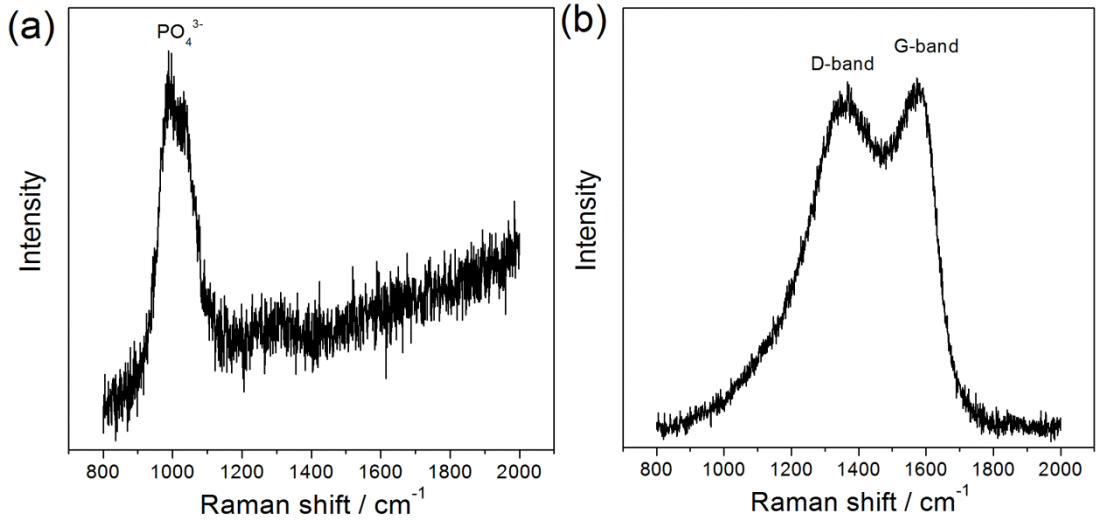

Fig. 6.6 Raman spectra of (a) pristine $LiFePO_4$ and (b) hollow spherical $LiFePO_4$/C

6.3 Electrochemical properties

As stated above, both $LiFePO_4$/C composites have favourable charge and mass transport features with nanoscale crystalline size, thin layer carbon coating and 3d porous frameworks. To characterize and compare electrochemical performances of these two types of composites, discharge rate capabilities and cyclic test were carried out on half-cells with metallic lithium as counter electrode. Fig. 6.7 compares the discharge rate capability of porous and hollow $LiFePO_4$. At low current density of 0.1C, hollow spherical $LiFePO_4$/C can deliver a discharge capacity of 153 mAh g^{-1}, higher than that (139 mAh g^{-1}) of porous $LiFePO_4$. It should be mentioned here that the specific capacity calculation here did not substrate the carbon content, thus a specific capacity of 167 $mAhg^{-1}$ for active $LiFePO_4$, very close to the theoretical capacity of $LiFePO_4$ (170 mAh g^{-1}), can be utilized for hollow spherical $LiFePO_4$/C. At high discharge rates, hollow spherical $LiFePO_4$/C also shows higher discharge capacities and better retention relative

to specific capacity at 0.1 C. For example, porous $LiFePO_4$/C can only deliver 54 mAh g^{-1} at 20 C and 37 mAh g^{-1} at 30 C, while hollow spherical $LiFePO_4$/C can deliver 90 mAh g^{-1} at 20 C and 74 mAh g^{-1} at 30 C. Clearly, hollow spherical $LiFePO_4$/C has a superior electrochemical performance compared to porous $LiFePO_4$/C. This can be ascribed to the smaller crystallite size and more uniform carbon coating. Moreover, the micrometre-sized spherical particles are more favourable for the uniformity and compactness in the electrodes.

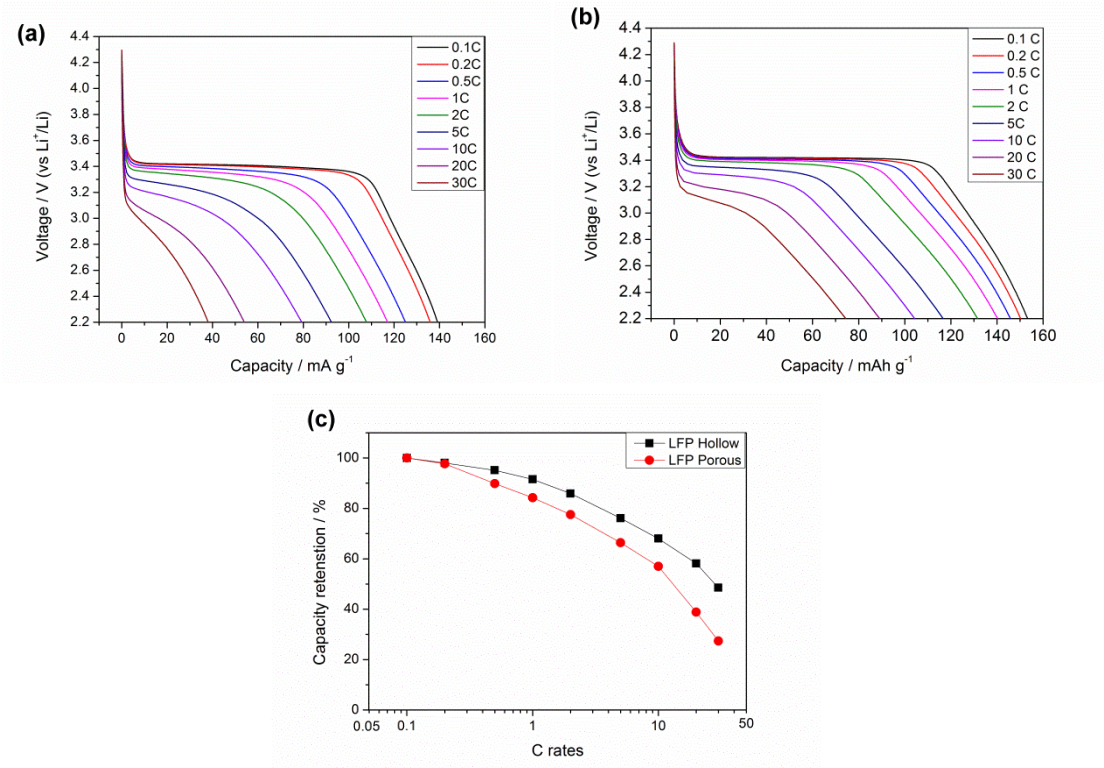

Fig. 6.7 Electrochemical performances of $LiFePO_4$/C composites; (a, b) discharge rate capabilities of porous $LiFePO_4$ and hollow $LiFePO_4$ (c) high discharge rate retention compared to practical capacity at 0.1 C

Fig. 6.8 shows the cyclic performance of hollow spherical $LiFePO_4$/C cycled at 1 C. After 200 cycles and a duration of 16 days, a capacity of 135.4 mAh g^{-1}, or 98.1 % of the initial capacity, could still be retained. The half-cell tested also maintained very high

columbic efficiencies during cycling with a mean value of 99.96%. In spite of the high porosity and high electrode/electrolyte contact area, hollow spherical $LiFePO_4$/C exhibits an excellent stability with the electrolyte during the cyclic tests.

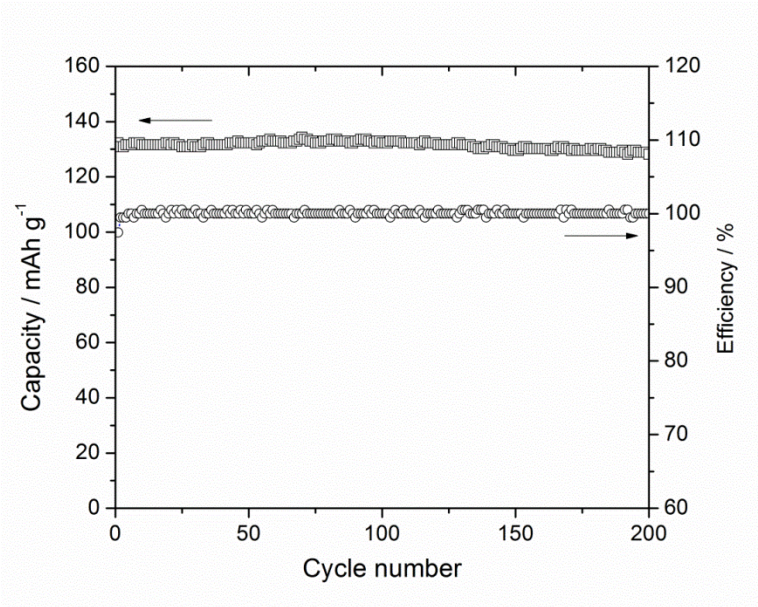

Fig. 6.8 Cyclic performance of hollow spherical $LiFePO_4$/C at 1C

6.4 Summary

In summary, a novel and facile template free sol-gel method in fabrication of nano-sized phosphate materials has been demonstrated. Phosphonate chelating agents that also served as in-situ phosphorous and carbon sources were adopted instead of traditional Lewis group chelating agents and inorganic phosphorous agents. As an example, two types of $LiFePO_4$/C composites with porous or hollow spherical secondary architectures were synthesized and characterized using EDTMP in this chapter., $LiFePO_4$/C synthesized with assistance from spray-drying exhibit a hollow

spherical morphology of a 1-5 μm in diameter with shells of ~200 nm in thickness. The shell of the micrometre-sized hollow spherical particles was constructed by $LiFePO_4$/C core-shell nanoparticles of 20-30 nm. Amorphous carbon was uniformly coated on the nanoparticles of $LiFePO_4$ with a thickness of ~2nm. The hollow spherical $LiFePO_4$/C exhibited superior rate capabilities and excellent cyclic performance. In addition, this synthesis approach can be easily adopted for other phosphate materials with benefits of very fine crystallites of < 30 nm, uniform carbon coating and micrometre hollow spherical secondary architectures.

7 Building safe and high rate full-cell

Phosphate cathode materials such as $LiFePO_4$, $LiFe_xMn_{1-x}PO_4$ and $LiVPO_4F$ have been successfully developed with both high performance and unique safety features. It becomes natural to find a proper safe anode material to couple with them. Graphite carbon has been used as anode since LIB was first commercialized in 1991. However, flammability of lithiated graphite and metallic lithium plating upon fast charge are severe risks in large scale multi-cell systems [128]. Hence, many efforts have been devoted to develop alternatives such as TiO_2/Li_xTiO_y, tin and silicon. It is still challenging to reversibly utilize the theoretical capacity of TiO_2. Li^+ insertion in bulk TiO_2 is hindered by wide band gap in nature and poor Li^+ transport. Nano-sizing is therefore necessary to improve Li^+ insertion behavior by shortening diffusion distances and enlarging electrode/electrolyte contact area [173, 174]. In previous studies, nano-size TiO_2 was commonly synthesized via hydrolysis or hydrothermal reaction [173-179]. In this work, nanocrystalline anatase TiO_2 was synthesized via mechanochemical reaction, which is a rapid, facile and economical process [180-184]. It has been successfully used to synthesize nanostructure rutile TiO_2 reinforced Sn [185]. This chapter reports its first application of synthesis of pure anatase TiO_2 as active anode material.

7.1 Material preparation

Mechanochemical reaction between titanium chloride ($TiCl_4$) and ammonium bicarbonate (NH_4HCO_3) was induced by high-energy milling in an inert atmosphere. In a typical process, liquid $TiCl_4$ (99%, Sigma-Aldrich) and NH_4HCO_3 (99%, Merck) were sealed in a stainless steel milling jar inside an argon glove box (MBraun; H_2O, O_2: <0.1 ppm). Then, high-energy ball milling was carried out for 15 min using SPEX-8000M. Finally, the as-milled powders were annealed at 400 °C, 500 °C, 600 °C and 700 °C for 1 h in air and flowing argon, respectively. The TiO_2 materials synthesized were denoted by their annealing conditions for short.

7.2 Characterization

7.2.1 Crystal structure

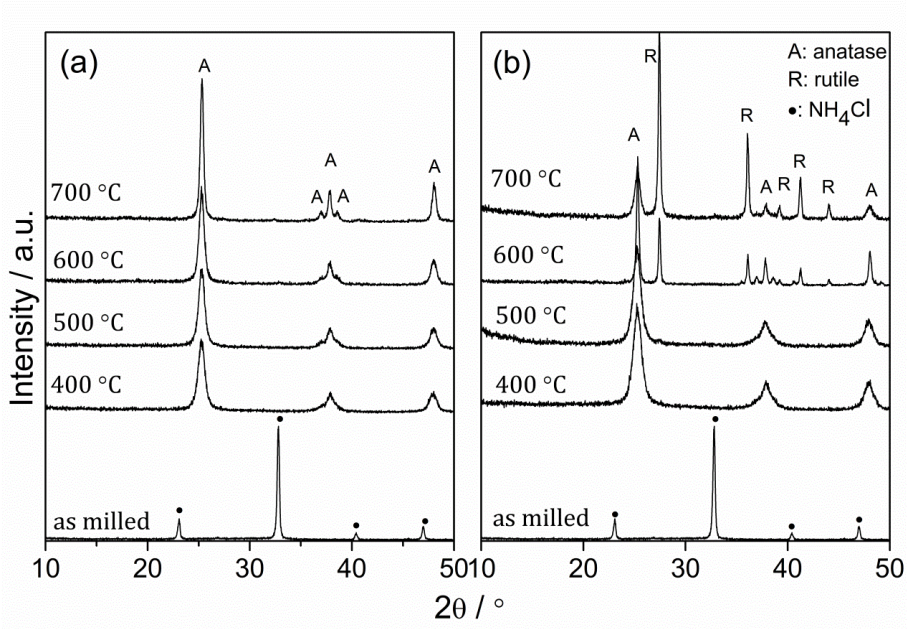

Fig. 7.1 XRD patterns of the milled precursor and TiO_2 annealed (a) in air and (b) in Ar.

Fig. 7.1 shows the XRD patterns of the materials investigated. After milling, NH_4Cl is the only detectable phase in the as-milled powders, while the TiO_2 could be in an amorphous form. Therefore, the overall mechanochemical reaction upon ball milling can be expressed as:

$TiCl_4 + 4NH_4HCO_3 \rightarrow TiO_2$ (amorphous) + $4NH_4Cl$ (solid) + $2H_2O$ (liquid and/or gas) + $4CO_2$ (gas)

After annealing, diffraction peaks from NH_4Cl vanish, whereas depending on annealing temperature crystalized anatase and rutile become the only remaining phases. Crystal structures of the annealed TiO_2 vary with annealing atmosphere. For TiO_2 annealed in air, single-phase anatase was obtained starting from 400 °C to 700 °C. On the other hand, for TiO_2 annealed in argon, single-phase anatase was obtained at 400 °C and 500 °C, while rutile started to emerge at 600 °C and became the main phase at 700 °C. Anatase-rutile phase transition temperature is clearly below 600 °C in a non-oxidizing atmosphere.

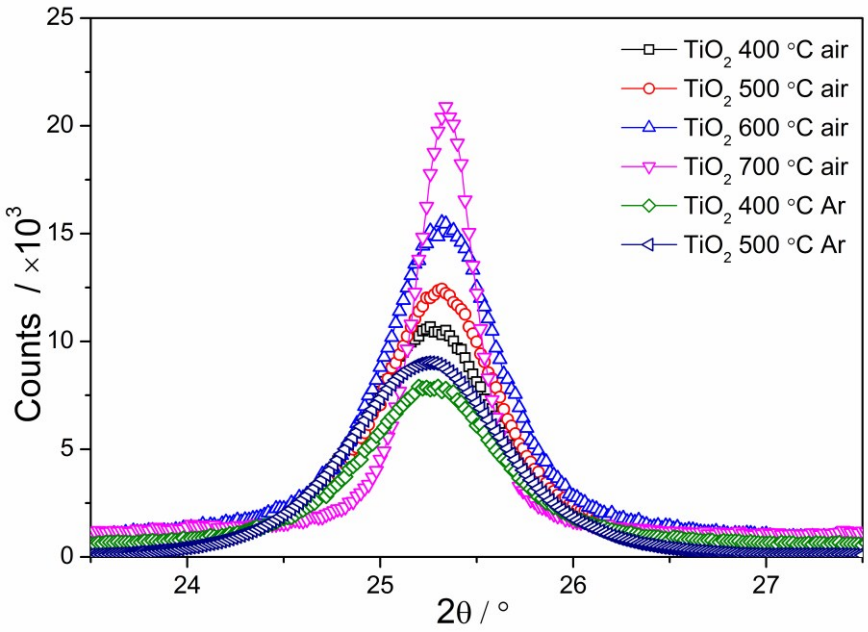

Fig. 7.2 High counts XRD patterns of anatase (101) peak.

The average crystallite size was estimated from XRD peak broadening by application of Scherrer equation [186, 187]. Fig. 7.2 shows the high counts XRD pattern of single-phase anatase TiO_2 collected between 23° and 28° (2θ). The full-width at half maximum (FWHM) of the anatase (101) peak at 25.3° was measured. $K_{\alpha 2}$ contributions were subtracted with the aid from software, while instrumental broadening were corrected based on diffraction data of standard silicon powders (325 mesh). Table 7.1 summarizes the FWHM and calculated average crystallite sizes of TiO_2 annealed under different conditions. Average crystallite size increases gradually from about 11 nm to about 31 nm with increasing annealing temperature from 400 °C to 700 °C. The annealing atmosphere seems to have little effect on crystallite size. For example, the average crystallite size of $TiO_{2\ 400\ °C,\ air}$ is 11.7 nm, almost identical to that (11.2 nm) of $TiO_{2\ 400\ °C,\ Ar}$. Crystallite sizes of TiO_2 annealed in argon above 600 °C were directly observed using SEM due to existence of large particles.

Table 7.1 Structure and crystallite size of TiO_2 prepared via mechanochemical reaction

Sample	Structure	FWHM (°)	FWHM-B_0 (°)	Crystallite size (nm)
400 °C air	anatase	0.79296	0.68696	11.7
500 °C air	anatase	0.72158	0.61558	13.0
600 °C air	anatase	0.60801	0.50201	16.0
700 °C air	anatase	0.36447	0.25847	31.0
400 °C Ar	anatase	0.82291	0.71691	11.2
500 °C Ar	anatase	0.72571	0.61971	12.9
600 °C Ar	anatase+ rutile	N.A	N.A	~100 (rutile, SEM)
700 °C Ar	anatase+ rutile	N.A	N.A	~200 (rutile, SEM)

7.2.2 Thermal analysis

Thermal analysis was carried out to investigate reactions of the as-milled powders upon annealing. Fig. 7.3 shows the simultaneous TGA and DTG results of the as-milled powders. Two stages of reactions can be identified from the TGA and DTG curves. In the first stage from room temperature to about 210 °C, TGA shows a gradual weight loss of 6.9% in total, which may be caused by dehydration. Sources of the three small exothermic peaks at 56 °C, 109 °C and 207 °C are not clear but may probably be associated with dissociation and dehydration. In the second stage between about 210 °C and 310 °C, a sharp weight loss of about 67.0% could be observed, which may be ascribed to decomposition of NH_4Cl. DTG also shows a very strong exothermic peak at

292 °C for this reaction. Above 310 °C, neither noticeable weight loss nor thermal peaks can be detected, indicating that the ammonium salts and hydrates have been completely eliminated, in line with XRD observation.

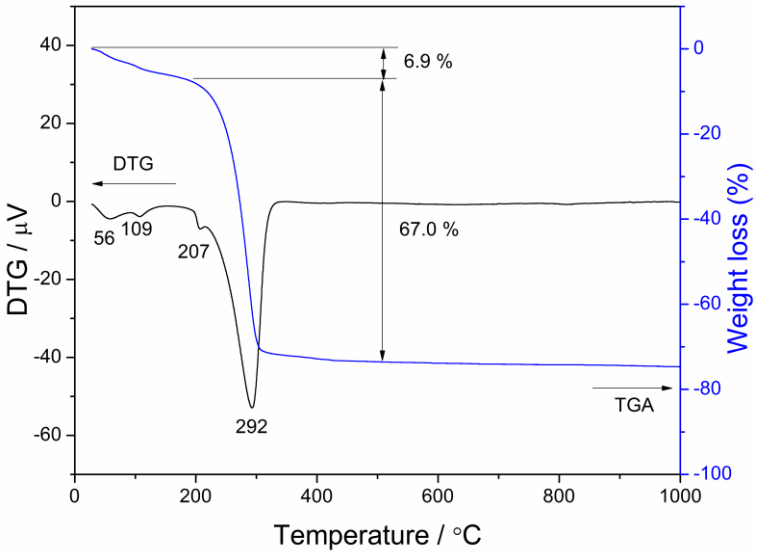

Fig. 7.3 TGA and DTG curves of the as-milled powders.

7.2.3 Morphology and conductivity

The color of TiO_2 powder was pure white when it was annealed in air but changed to light yellow green when annealed in argon. This is probably the result of defects generated upon annealing in argon. In a non-oxidizing annealing atmosphere, oxygen vacancies can be generated at high temperature and Ti^{4+} would be partially reduced to Ti^{3+} (3d) defect states [188] through the defect reaction:

$$Nil \xrightarrow[Low oxygen\ pressure]{} \left(Ti^{3+}\right)'_{Ti} + \frac{3}{2}O_O^x + \frac{1}{2}V_O^{\cdot\cdot} + \frac{1}{4}O_2(gas)$$

As a result of more electron–hole recombination sites, electronic conductivity for TiO_2 crystallite annealed in argon was likely elevated [189]. DC polarization tests were

carried out on compacted powders to measure electronic conductivity of TiO_2 powders annealed at 400 °C. The results indeed confirmed that the electronic conductivity of $TiO_{2\ 400\ °C,\ Ar}$ is 2.41×10^{-8} S cm^{-1}, about two-orders higher than that of $TiO_{2\ 400\ °C,\ air}$ (2.59×10^{-10} S cm^{-1}).

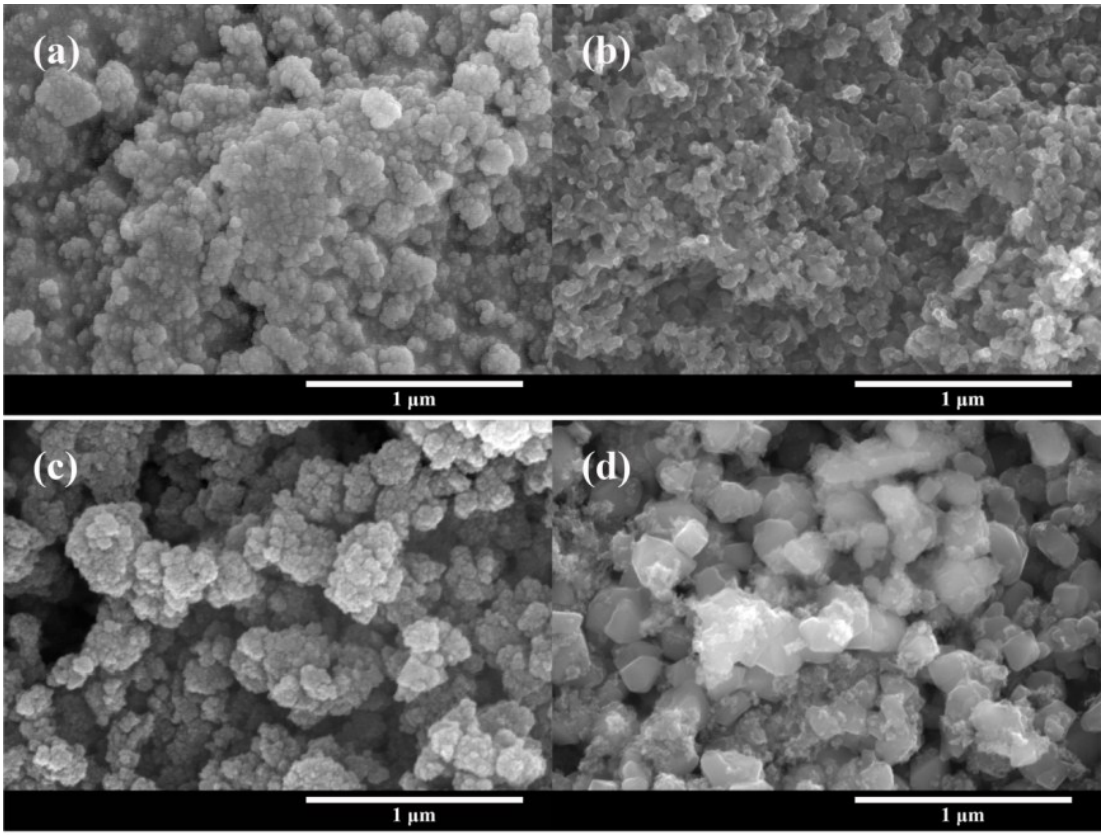

Fig. 7.4 SEM images of TiO2 synthesized via mechanochemical milling
(a) $TiO_{2\ 400°C\ air}$, (b) $TiO_{2\ 700°C\ air}$, (c) $TiO_{2\ 400°C\ Ar}$ and (d) $TiO_{2\ 700°C\ Ar}$.

Micromorphology of the TiO_2 synthesized was observed using SEM and TEM. SEM images, shown in Fig. 7.4, indicate that typical TiO_2 secondary particles are about 100-500 nm in size consisting of very fine nano-crystallites. The mix-phase $TiO_{2\ 700\ °C,\ Ar}$ shows distinctly uneven particle size distribution with small anatase crystallites of only ~30 nm and rutile particle of ~200 nm. TEM images of $TiO_{2\ 400\ °C,\ Ar}$ shown in Fig. 7.5 (a)

and (b) reveal the crystallite size of as fine as ~10 nm, while the secondary particles are in the size of several hundreds of nanometers. Selected area electron diffraction (SAED) pattern in Fig. 7.5 (c) appears as concentric circles, which can be ascribed to anatase structure. The crystallite sizes observed by SEM and TEM are both consistent with the average crystallite size derived from Scherrer equation.

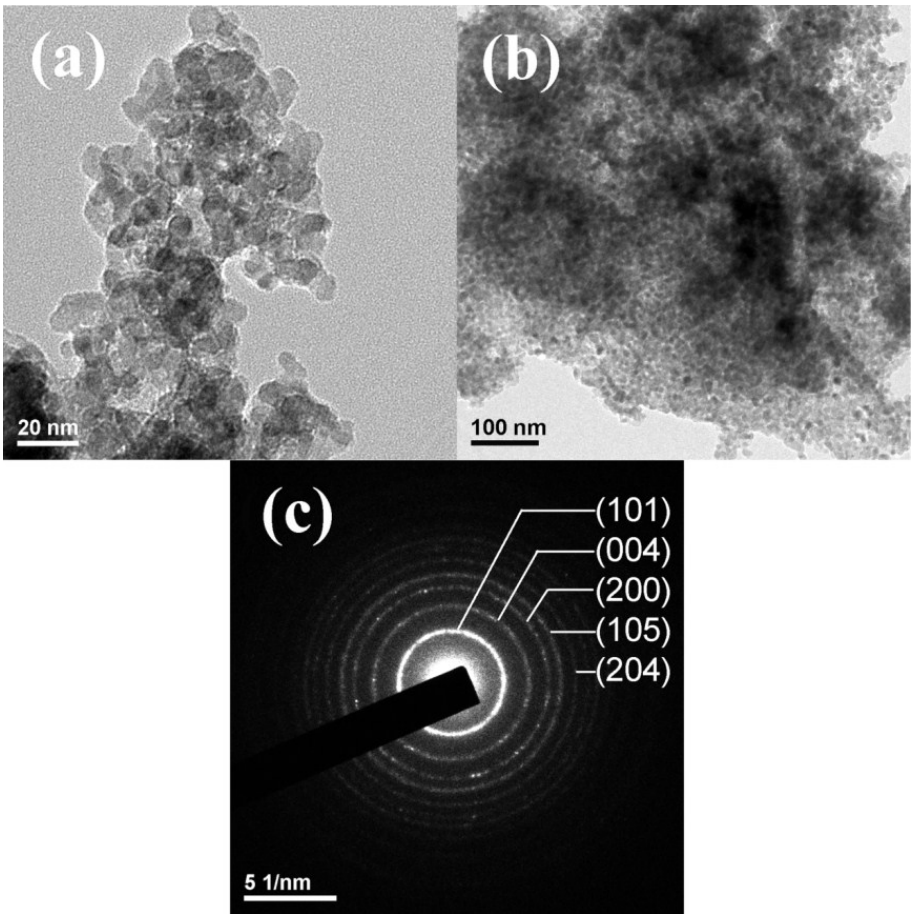

Fig. 7.5 TEM images and SEAM pattern of $TiO_{2\ 400\ ^{\circ}C\ Ar}$. (a) and (b) TEM images, (c) SAED pattern.

7.3 Electrochemical properties

Li^+ insertion and extraction of TiO_2 can be generally expressed as $TiO_2 + xLi^+ + xe^-$ $\leftrightarrow Li_xTiO_2$. In a typical biphasic reaction for anatase, Li^+ poor anatase $Li_\varepsilon TiO_2$ (*I41*/*amd*)

phase and lithium titanate phase $Li_{0.5}TiO_2$ (*Imma*) coexist in a single particle. The number of electron exchange per formula, *x*, can only reach 0.5-0.6 in microcrystalline anatase, while further reaction of Li^+ with formation of Li_1TiO_2 (*I*41/*amd*) phase can be achieved in nanometer-sized anatase, which has recently been demonstrated by chemical lithiation of 6 nm anatase [190].

7.3.1 Cyclic voltammetry

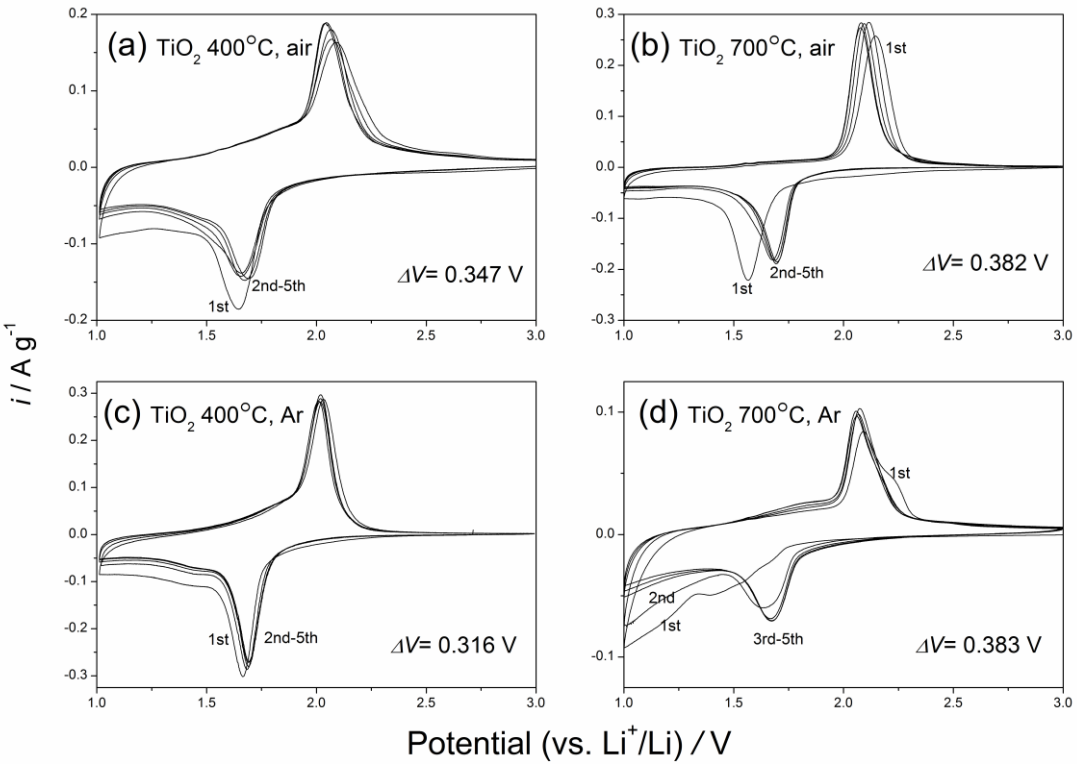

Fig. 7.6 Cyclic voltammograms curves of TiO_2 with a scan rate of 0.1 mV s^{-1}. (a) $TiO_{2\ 400\ °C\ air}$, (b) $TiO_{2\ 700\ °C\ air}$, (c) $TiO_{2\ 400\ °C\ Ar}$ and (d) $TiO_{2\ 700\ °C\ Ar}$.

Fig. 7.6 shows the CV plots of TiO_2 annealed at different conditions. The CV tests were carried out on fresh cells for 5 cycles with a scan rate of 0.1 mV s^{-1}. $TiO_{2\ 700\ °C,\ air}$ (about 31 nm) shows sharp characteristic peaks of anatase at about 1.69V / 2.08V. Compared to the well crystalized $TiO_{2\ 700\ °C,\ air}$, anatase $TiO_{2\ 400\ °C,\ air}$ and $TiO_{2\ 400\ °C,\ Ar}$

(about 11 nm) show broadened peaks, indicating broadened energy distribution of Li^+ insertion/extraction in these nano-size anatase crystallites. Mix-phase $TiO_{2\ 700°C,\ Ar}$ shows additional peaks of rutile at about 1.40V / 2.22V in the first cycle, which unfortunately are irreversible in the following cycles. The peak currents of $TiO_{2\ 700\ °C,\ Ar}$ are also considerably lower than those of other anatase TiO_2 materials, showing poor Li^+ accommodation properties. The potential hysteresis, i.e. peak separation (ΔV) between main cathodic and anodic peaks, was also measured for the final cycle. ΔV of $TiO_{2\ 400\ °C,\ air}$ is smaller than that of $TiO_{2\ 700\ °C,\ air}$ by ~35 mV. Particle size effects was the main cause for this hysteresis difference. Moreover, $TiO_{2\ 400\ °C,\ Ar}$ has an even smaller ΔV than similar size $TiO_{2\ 400\ °C,\ air}$ by ~30 mV, probably benefited from its higher electronic conductivity.

7.3.2 Specific capacity

Galvanostatic discharge-charge cycling at a low current density of 30 mA g^{-1} was carried out to investigate the Li^+ accommodation properties and specific capacities of TiO_2. Fig. 7.7 shows the initial discharge-charge profiles of representative TiO_2 materials. All single-phase anatase TiO_2 can deliver reversible capacities higher than 200 mAh g^{-1}. On the other hand, mix-phase $TiO_{2\ 700\ °C,\ Ar}$ only delivers a reversible capacity of 95 mAh g^{-1} corresponding to only 0.28 mol of Li^+ insertion (x ~0.28), encumbered by the electrochemically inactive rutile phase. $TiO_{2\ 400\ °C,\ Ar}$ has the highest first discharge capacity up to 326 mAh g^{-1} (x ~0.97), close to the theoretical value of 335 mAh g^{-1}. Its first cycle coulombic efficiency is 74.9%, while about 230 mAh g^{-1} (x ~0.69)

can be stably retained after 5 cycles. This Li^+ accommodation property is comparable with those of porous and nanotube TiO_2 synthesized via other techniques [175, 191, 192]. It is interesting to note that single-phase anatase annealed in argon can host more Li^+ than those annealed in air. For example, $TiO_{2\ 400\ °C,\ Ar}$ has noticeably higher initial discharge capacity and reversible capacity than $TiO_{2\ 400\ °C,\ air}$.

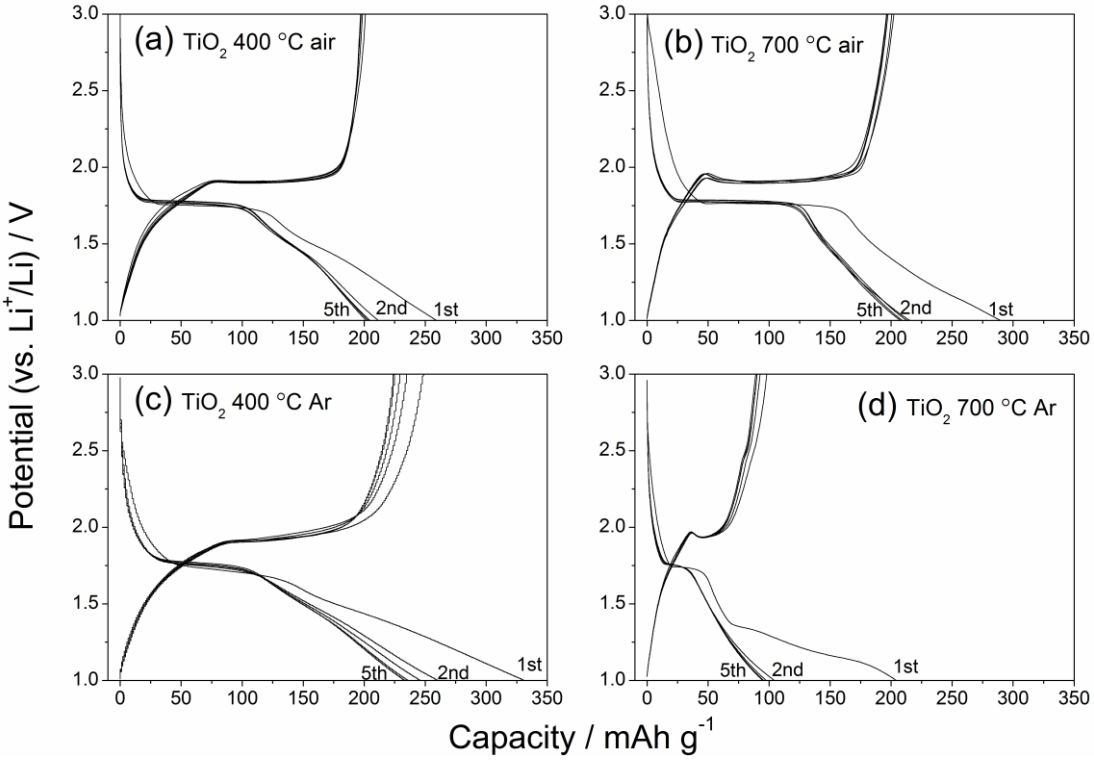

Fig. 7.7 Initial discharge-charge profiles of TiO_2 at current density of 30 mA g^{-1} (a) $TiO_{2\ 400\ °C\ air}$, (b) $TiO_{2\ 700\ °C\ air}$, (c) $TiO_{2\ 400\ °C\ Ar}$ and (d) $TiO_{2\ 700\ °C\ Ar}$.

7.3.3 Rate capability and cycleability

Fig. 7.8 compares the rate capabilities of TiO_2 annealed under different conditions. 1C is defined as 200 mAh g^{-1} in this work, since most of the materials have a specific capacity of about 200 mAh g^{-1}. For the same annealing atmosphere, the rate capability of TiO_2 is mainly associated with the crystallite size. With the finest crystallite sizes of 11

nm $TiO_{2\ 400\ °C,\ Ar}$ and $TiO_{2\ 400\ °C,\ air}$ exhibit the best rate capabilities among all the materials investigated. High current density performance of $TiO_{2\ 400\ °C,\ air}$ is far better than that of $TiO_{2\ 700\ °C,\ air}$, even though its initial capacity is lower than that of $TiO_{2\ 700\ °C,\ air}$ (also seen in Fig. 6). At a high current density of 5C (1 A g^{-1}), only 33 mAh g^{-1} can be achieved for $TiO_{2\ 700\ °C,\ air}$ compared to 115 mAh g^{-1} for $TiO_{2\ 400\ °C,\ air}$. Overall, $TiO_{2\ 400\ °C,\ Ar}$ has better rate capability, slightly better than that of $TiO_{2\ 400\ °C,\ air}$ owing to higher electronic conductivity and higher specific capacity. As expected, $TiO_{2\ 700\ °C,\ air}$ shows shallow rate performance due to large and inactive rutile particles.

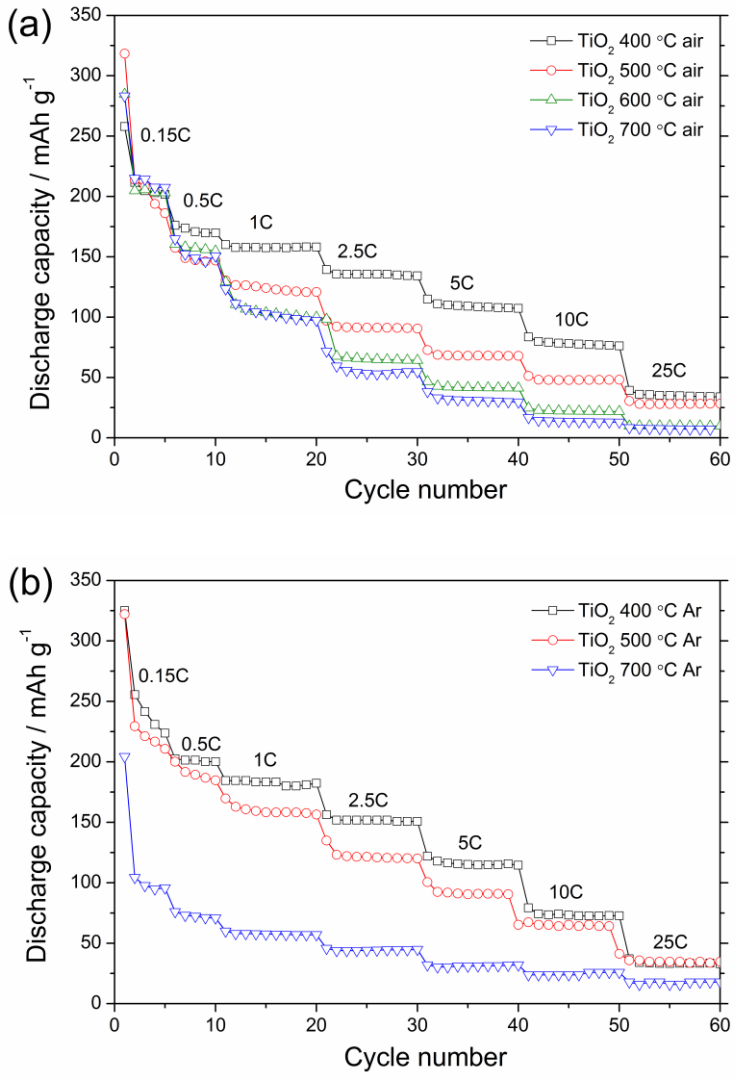

Fig. 7.8 Discharge-charge cyclic tests of TiO_2 at various current densities (a) TiO_2 annealed in air and (b) TiO_2 annealed in argon. 1C is defined as 200 mAh g^{-1}.

Reducing crystallite size can evidently improve the kinetics of Li^+ insertion/extraction in anatase [174, 190, 193, 194]. As shown in Fig. 7.7 (b), despite a very small current density of 0.15C (0.03 A g^{-1}), notable polarizations arose at the beginning of the charge plateau of the 35 nm $TiO_{2\ 700\ °C,\ air}$, indicating strain induced energy barrier. Such polarizations cannot be found in the 11 nm $TiO_{2\ 400\ °C,\ air}$ and $TiO_{2\ 400\ °C,\ Ar}$. $TiO_{2\ 400\ °C,\ air}$ and $TiO_{2\ 400\ °C,\ Ar}$ also gained more capacity from slope solid solution domain in the charge-discharge profiles at the expense of biphasic plateau domain, as compared to $TiO_{2\ 700\ °C,\ air}$. Hence, other than improving charge and mass transport, nanocrystalline can also decrease phase transformation strain and enhance solid solution [190, 193].

Fig. 7.8 also indicates the nanocrystalline TiO_2 synthesized via mechanochemical reactions has good cyclic performances at various current densities. Long-term cyclic tests were conducted on $TiO_{2\ 400\ °C,\ Ar}$ half-cells to further challenge its stability. As shown in Fig. 7.9, nanocrystalline $TiO_{2\ 400\ °C,\ Ar}$ exhibits excellent long-term capacity retention at both 1C and 5C. After 200 cycles at 1C (0.2 A g^{-1}), a capacity of 163 mAh g^{-1} can be retained from the initial 172 mAh g^{-1}. For the following 500 cycles at 5C (1 A g^{-1}), the capacity fading is negligible. Such a long cycle life of nanocrystalline TiO_2 has rarely been reported before.

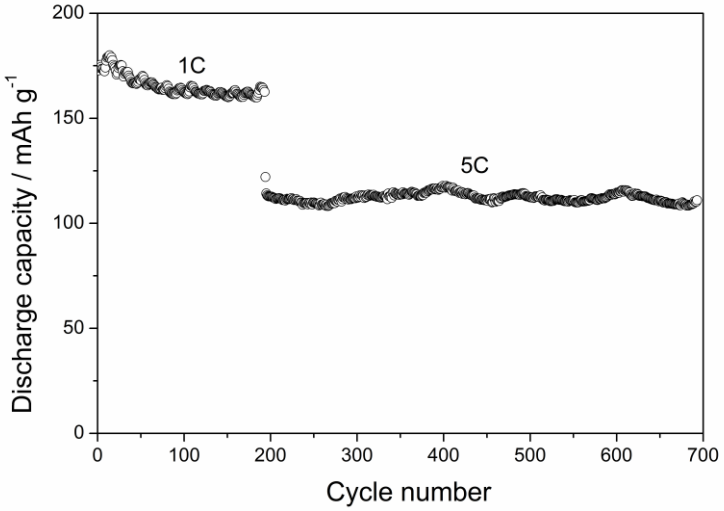

Fig. 7.9 Long-term cyclic performances of $TiO_{2\ 400\ °C\ Ar}$

7.3.4 $LiFePO_4/TiO_2$ and $LiVPO_4F/TiO_2$ full-cells

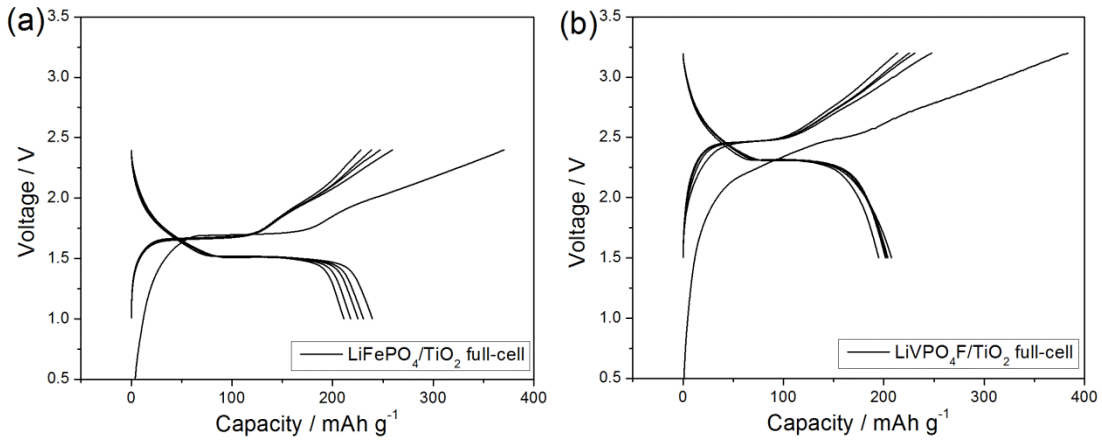

Fig. 7.10 Charge-discharge curves of (a) $LiFePO_4/TiO_2$ and (b) $LiVPO_4F/TiO_2$ full-cells at 30 mA g^{-1}.

The full-cell performance of TiO_2 is further demonstrated using phosphate cathode as counter electrode instead of metallic lithium. Carbon coated $LiFePO_4$ developed in Chapter 4 and $LiVPO_4F$ developed in Chapter 6 were selected for their superb electrochemical performances. Due to the irreversible lithiation of TiO_2 in the first cycle, excessive amount of cathode material was used to provide enough lithium in the full-cells. Fig. 7.10 shows the voltage profiles of $LiFePO_4/TiO_2$ and

$LiVPO_4F/TiO_2$ full-cells charge/discharged at 30 mA g^{-1}. The $LiFePO_4/TiO_2$ full-cell shows an operation voltage of ~1.5 V, while the $LiVPO_4F/TiO_2$ full-cell shows a higher operation voltage of ~2.3 V because of the higher potential of $LiVPO_4F$ (4.2 V vs. Li^+/Li) than that of $LiFePO_4$ (3.4 V vs. Li^+/Li). The cycleability and reversibility of the $LiFePO_4/TiO_2$ and $LiVPO_4F/TiO_2$ full-cells may not be as good as those of half-cells due to the technical difficulties in the laboratory full-cell assembly (geometry area mismatch and electrode thickness non-uniformity).

7.4 Summary

Anatase TiO_2 has been synthesized via mechanochemical reaction which is a rapid and facile process. Effects of annealing temperature and atmosphere on crystal structure, crystallite size, electronic conductivity and electrochemical properties are thoroughly investigated. Annealing of mechanochemically milled precursor in non-oxidizing atmosphere creates oxygen deficiency and hence elevates electronic conductivity, benefitting Li^+ insertion/extraction in anatase. Reduction in particle size of TiO_2 can significantly improve rate capability. TiO_2 annealed at 400 °C in argon has the smallest crystallite size of only ~11 nm and the best electrochemical performance in this work. It can host almost 1 Li^+ per formula in its first discharge, delivering a reversible capacity of about 230 mAh g^{-1}. It also exhibits excellent long-term cycleability for over 700 cycles. The $LiFePO_4/TiO_2$ and $LiVPO_4F/TiO_2$ full-cells have been demonstrated with operation voltages of ~1.5 V and 2.3 V, respectively.

8 Conclusions and Recommendations

8.1 Conclusions

1 Electronic and ionic conductivity, particle size and micromorphology are essential to the high rate performances of phosphate cathode materials. Generally, facile electronic/ionic transport and small particle size will lead to high rate performances. Electronic conductivity of phosphate cathode materials can be improved either by trace supervalent cation doping or conductive carbon coating.

2 The RuO_2 trace doping dramatically raised the electronic conductivity by up to 6 orders over the pristine $LiFePO_4$. Electronically conductive $Li_{1-4x}Ru_xFePO_4$ (x= 0.005, 0.01 and 0.02) exhibited amazingly high power performance and fast charge capability. $Li_{1-4x}Ru_xFePO_4$ also exhibited excellent long-term cyclic performance for over 1000 cycles at high current density of 20C. The maximum solubility of Ru dopant in olivine $LiFePO_4$ lattice is probably limited to 2 mol%. However, RuO_2 trace doping showed very limited effects on $LiMnPO_4$ and $LiCoPO_4$, both of the same olivine structure with $LiFePO_4$.

3 Effective carbon coating can significantly improve the electrochemical properties of olivine cathode materials. $LiFe_{1-x}Mn_xPO_4$/C core-shell composites were successfully developed via a facile one-step liquid polymer-assisted mechanical activation. The polymer-assisted mechanical activation evidently reduced the particle size and provides uniform amorphous carbon coating. With assistance of

PPG, the as synthesized $LiMn_{0.75}Fe_{0.25}PO_4$/C nanoparticles were approximately 60 nm in diameter with a thin carbon coating of 1-2 nm. The existence of Fe-O-Mn interaction significantly reduced the polarization Mn^{2+}/Mn^{3+} reaction in olivine lattice. $LiFe_{1-x}Mn_xPO_4$/C synthesized with assistance of PPG had uniform particle size and carbon coating, and thus impressive electrochemical properties. Energy density of PPG-$LiFe_{1-x}Mn_xPO_4$ was 12% higher than that of $LiFePO_4$ at 0.2C. However, high Mn content in $LiFe_{1-x}Mn_xPO_4$ led to large polarizations of the Mn^{2+}/Mn^{3+} reaction, inferior fast charge capability and relatively poor cyclic performances. An optimum Mn content x for PPG-$LiFe_{1-x}Mn_xPO_4$ should be 0.5 with comprehensive considerations.

4 Tavorite lattice has a relatively faster Li^+ ionic conductor when compared to olivine lattice. Unlike olivine $LiMPO_4$, Tavorite $LiVPO_4F$ is a relatively fast ionic conductor with an ionic conductivity up to 8×10^{-7} S cm^{-1}. Diffusion coefficient of tavorite $LiVPO_4F$ (lithium rich phase) is ~10^{-13} cm^2 s^{-1}, 2 orders higher than that in olivine materials. On the other hand, electronic conductivity of $LiVPO_4F$ is only 10^{-8} S cm^{-1}, which should be the main limiting factor for high rate performance. Carbon coated $LiVPO_4F$/C of ~150 nm in diameter exhibited amazingly high power performance, fast charge capability and very good stability in long-term cycling. $LiVPO_4F$/C has a higher overall potential and a higher gravimetric power density than olivine $LiFePO_4$ and $LiFe_{1-x}Mn_xPO_4$. It can be a high performance alternative to olivine $LiFePO_4$ and $LiFe_{1-x}Mn_xPO_4$.

5 A novel and facile template free sol-gel method in fabrication of nano-sized phosphate materials has been demonstrated. Phosphonate chelating agents, which also served as in-situ phosphorous and carbon sources, were used instead of traditional Lewis group chelating agents and inorganic phosphorous sources. This synthesis approach can be easily adopted for many phosphates materials with benefits of very fine crystallites <30 nm, uniform carbon coating and hollow sphere secondary architectures.

6 Nanocrystalline anatase TiO_2 can be synthesized via a rapid and facile mechanochemical reaction. Annealing of mechanochemically milled precursor in non-oxidizing atmosphere creates oxygen deficiency and hence elevates electronic conductivity, benefitting Li^+ insertion/extraction in anatase. Reduction in particle size of TiO_2 can significantly improve rate capability. TiO_2 annealed at 400 °C in argon has the smallest crystallite size of only ~11 nm. It can host almost 1 Li^+ per formula in its first discharge, delivering a reversible capacity of about 230 mAh g^{-1}. It also exhibits excellent long-term cycleability for over 700 cycles.

8.2 Limitations and recommendations

1 The M1 site occupancy of Li and Ru in $Li_{1-4x}Ru_xFePO_4$ cannot be determined in this work due to the limitations of laboratory X-ray diffraction to light lithium atoms. Neutron diffraction is recommended to finally determine the M1 site occupancy of Li and Ru. High-resolution scanning tunnelling electron microscope

may also be recommended to directly observe the defect cluster and Li-Fe anti defect after RuO_2 trace doping.

2 The band structure after 4d transitional metal doping on olivine $LiMPO_4$ can be investigated through ab-initio simulation. Other supervalent cathions with free unpaired 4d electrons, such as Nb^{3+}(*4d2*), Nb^{4+}(*4d1*) and Rh^{3+}(*4d6*) may be doped in the lattice of $LiFePO_4$ and even $LiMnPO_4$ for further investigations.

3 The occupancy and exact position of Li in $LiVPO_4F$ need to be identified through high quality powder diffraction results of neutron diffraction and/or Synchrony diffraction. The abnormal and rare non-Arrhenius behaviour of electrical conductivity is recommended for further study. The author suspects that there may be a phase transition related to the rearrangement of Li^+ over the temperature range of 25-80 ºC.

4 Effects of molecular weight of the liquid form polymer on the carbon coating and electrochemical properties of PPG-$LiFe_{1-x}Mn_xPO_4$/C are recommended for further research.

5 Although mechanochemical milling can produce large amount of TiO_2 compared to other techniques, the rate performance of the TiO_2 in this work still fall short on high rate performance. Carbon coating along with polymer-assisted mechanical activation developed in Chapter 4 may be a very promising approach to overcome this problem.

6 Although the porous and hollow spherical $LiFePO_4$ synthesized with EDTMP

already demonstrated good rate capabilities, the author believe the performances should be even better considering the uniformly fine particle size through further refinement of processing. Nanostructured $LiMnPO_4$, $LiFe_{1-x}Mn_xPO_4$ and $LiCoPO_4$ can also be easily synthesized via this method. Moreover, many other phosphonate compounds can be adopted in the synthesis routes to tailor the morphology, carbon coating and electrochemical properties.

References

[1] T. Nagaura, K. Tozawa, Progress in Batteries & Solar Cells, 9 (1990) 209.

[2] M.S. Whittingham, Chemical Reviews, 104 (2004) 4271-4301.

[3] M.S. Whittingham, Journal of the Electrochemical Society, 123 (1976) 315-320.

[4] K. Mizushima, P.C. Jones, P.J. Wiseman, J.B. Goodenough, Materials Research Bulletin, 15 (1980) 783-789.

[5] J.B. Goodenough, Electrochemical cell with new fast ion conductors, in, US, 1980.

[6] H. Sato, D. Takahashi, T. Nishina, I. Uchida, Journal of Power Sources, 68 (1997) 540-544.

[7] Y. Takahashi, Y. Gotoh, J. Akimoto, S. Mizuta, K. Tokiwa, T. Watanabe, Journal of Solid State Chemistry, 164 (2002) 1-4.

[8] T. Ohzuku, A. Ueda, Solid State Ionics, 69 (1994) 201-211.

[9] K. Momma, F. Izumi, Journal of Applied Crystallography, 44 (2011) 1272-1276.

[10] N. Yabuuchi, T. Ohzuku, Journal of Power Sources, 119–121 (2003) 171-174.

[11] M.M. Thackeray, W.I.F. David, P.G. Bruce, J.B. Goodenough, Materials Research Bulletin, 18 (1983) 461-472.

[12] M.M. Thackeray, P.J. Johnson, L.A. de Picciotto, P.G. Bruce, J.B. Goodenough, Materials Research Bulletin, 19 (1984) 179-187.

[13] F. Cao, J. Prakash, Electrochimica Acta, 47 (2002) 1607-1613.

[14] M. Nishizawa, T. Ise, H. Koshika, T. Itoh, I. Uchida, Chemistry of Materials, 12 (2000) 1367-1371.

[15] G. Amatucci, J.M. Tarascon, Journal of the Electrochemical Society, 149 (2002) K31-K46.

[16] R.J. Gummow, A. Dekock, M.M. Thackeray, Solid State Ionics, 69 (1994) 59-67.

[17] R. Chromik, F. Beck, Electrochimica Acta, 45 (2000) 2175-2185.

[18] S.T. Myung, S. Komaba, N. Kumagai, Journal of the Electrochemical Society, 148 (2001) A482-A489.

[19] A.D. Robertson, S.H. Lu, W.F. Averill, W.F. Howard, Journal of the Electrochemical Society, 144 (1997) 3500-3505.

[20] Y.-K. Sun, Y.-S. Jeon, H.J. Leeb, Electrochemical and Solid-State Letters, 3 (2000) 7-9.

[21] S.H. Park, K.S. Park, Y.K. Sun, K.S. Nahm, Journal of the Electrochemical Society, 147 (2000) 2116-2121.

[22] F. Le Cras, D. Bloch, M. Anne, P. Strobel, Solid State Ionics, 89 (1996) 203-213.

[23] D. Song, H. Ikuta, T. Uchida, M. Wakihara, Solid State Ionics, 117 (1999) 151-156.

[24] Y. Ein-Eli, W.F. Howard Jr, S.H. Lu, S. Mukerjee, J. McBreen, J.T. Vaughey, M.M. Thackeray, Journal of the Electrochemical Society, 145 (1998) 1238-1244.

[25] H. Shigemura, H. Sakaebe, H. Kageyama, H. Kobayashi, A.R. West, R. Kanno, S. Morimoto, S. Nasu, M. Tabuchi, Journal of the Electrochemical Society, 148 (2001) A730-A736.

[26] H. Kawai, M. Nagata, M. Tabuchi, H. Tukamoto, A.R. West, Chemistry of Materials, 10 (1998) 3266-3268.

[27] H. Kawai, M. Nagata, H. Kageyama, H. Tukamoto, A.R. West, Electrochimica Acta, 45 (1999) 315-327.

[28] C. Sigala, D. Guyomard, A. Verbaere, Y. Piffard, M. Tournoux, Solid State Ionics, 81 (1995) 167-170.

[29] K. Amine, H. Tukamoto, H. Yasuda, Y. Fujita, Journal of Power Sources, 68 (1997) 604-608.

[30] J.B. Goodenough, Y. Kim, Chemistry of Materials, 22 (2010) 587-603.

[31] A. Kraytsberg, Y. Ein-Eli, Advanced Energy Materials, (2012).

[32] A.M. Kannan, A. Manthiram, Electrochemical and Solid-State Letters, 5 (2002) A167-A169.

[33] S.-W. Lee, K.-S. Kim, H.-S. Moon, H.-J. Kim, B.-W. Cho, W.-I. Cho, J.-B. Ju, J.-W. Park, Journal of Power Sources, 126 (2004) 150-155.

[34] M.M. Thackeray, C.S. Johnson, J.S. Kim, K.C. Lauzze, J.T. Vaughey, N. Dietz, D. Abraham, S.A. Hackney, W. Zeltner, M.A. Anderson, Electrochemistry Communications, 5 (2003) 752-758.

[35] Y.K. Sun, K.J. Hong, J. Prakash, K. Amine, Electrochemistry Communications, 4 (2002) 344-348.

[36] K.S. Nanjundaswamy, A.K. Padhi, J.B. Goodenough, S. Okada, H. Ohtsuka, H. Arai, J. Yamaki, Solid State Ionics, 92 (1996) 1-10.

[37] A. Manthiram, J.B. Goodenough, Journal of Power Sources, 26 (1989) 403-408.

[38] A. Manthiram, J.B. Goodenough, Journal of Solid State Chemistry, 71 (1987) 349-360.

[39] A.K. Padhi, V. Manivannan, J.B. Goodenough, Journal of the Electrochemical Society, 145 (1998) 1518-1520.

[40] A.K. Padhi, K.S. Nanjundaswamy, C. Masquelier, J.B. Goodenough, Journal of the Electrochemical Society, 144 (1997) 2581-2586.

[41] A.K. Padhi, W.B. Archibald, K.S. Nanjundaswamy, J.B. Goodenough, Journal of Solid State Chemistry, 128 (1997) 267-272.

[42] C. Masquelier, A.K. Padhi, K.S. Nanjundaswamy, J.B. Goodenough, Journal of Solid State Chemistry, 135 (1998) 228-234.

[43] A.K. Padhi, K.S. Nanjundaswamy, J.B. Goodenough, Journal of the Electrochemical Society, 144 (1997) 1188-1194.

[44] A. Yamada, S.C. Chung, K. Hinokuma, Journal of the Electrochemical Society, 148 (2001) A224-A229.

[45] C. Delacourt, L. Laffont, R. Bouchet, C. Wurm, J.B. Leriche, M. Morcrette, J.M. Tarascon, C. Masquelier, Journal of the Electrochemical Society, 152 (2005) A913-A921.

[46] S.Y. Chung, J.T. Bloking, Y.M. Chiang, Nature Materials, 1 (2002) 123-128.

[47] P.P. Prosini, M. Lisi, D. Zane, M. Pasquali, Solid State Ionics, 148 (2002) 45-51.

[48] A. Yamada, Y. Kudo, K.Y. Liu, Journal of the Electrochemical Society, 148 (2001) A747-A754.

[49] A. Yamada, Y. Kudo, K.Y. Liu, Journal of the Electrochemical Society, 148 (2001) A1153-A1158.

[50] S.K. Martha, B. Markovsky, J. Grinblat, Y. Gofer, O. Haik, E. Zinigrad, D. Aurbach, T. Drezen, D. Wang, G. Deghenghi, I. Exnar, Journal of the Electrochemical Society, 156 (2009) A541-A552.

[51] S.-M. Oh, S.-W. Oh, C.-S. Yoon, B. Scrosati, K. Amine, Y.-K. Sun, Advanced Functional Materials, 20 (2010) 3260-3265.

[52] S.-M. Oh, S.W. Oh, S.-T. Myung, S.-M. Lee, Y.-K. Sun, Journal of Alloys and Compounds, 506 (2010) 372-376.

[53] Z. Bakenov, I. Taniguchi, Electrochemistry Communications, 12 (2010) 75-78.

[54] J.-K. Kim, C.-R. Shin, J.-H. Ahn, A. Matic, P. Jacobsson, Electrochemistry Communications, 13 (2011) 1105-1108.

[55] D. Rangappa, K. Sone, Y. Zhou, T. Kudo, I. Honma, Journal of Materials Chemistry, 21 (2011) 15813-15818.

[56] P. Barpanda, K. Djellab, N. Recham, M. Armand, J.M. Tarascon, Journal of Materials Chemistry, 21 (2011) 10143-10152.

[57] M. Pivko, M. Bele, E. Tchernychova, N.Z. Logar, R. Dominko, M. Gaberscek, Chemistry of Materials, 24 (2012) 1041-1047.

[58] N.H. Kwon, K.M. Fromm, Electrochimica Acta, 69 (2012) 38-44.

[59] S.K. Martha, J. Grinblat, O. Haik, E. Zinigrad, T. Drezen, J.H. Miners, I. Exnar, A. Kay, B. Markovsky, D. Aurbach, Angewandte Chemie International Edition, 48 (2009) 8559-8563.

[60] Y.-K. Sun, S.-M. Oh, H.-K. Park, B. Scrosati, Advanced Materials, 23 (2011)

5050-5054.

[61] S.-M. Oh, S.-T. Myung, J.B. Park, B. Scrosati, K. Amine, Y.-K. Sun, Angewandte Chemie International Edition, 124 (2012) 1889-1892.

[62] H. Wang, Y. Yang, Y. Liang, L.-F. Cui, H. Sanchez Casalongue, Y. Li, G. Hong, Y. Cui, H. Dai, Angewandte Chemie International Edition, 50 (2011) 7364-7368.

[63] T. Nedoseykina, M.G. Kim, S.-A. Park, H.-S. Kim, S.-B. Kim, J. Cho, Y. Lee, Electrochimica Acta, 55 (2010) 8876-8882.

[64] S.-M. Oh, S.-T. Myung, Y.S. Choi, K.H. Oh, Y.-K. Sun, Journal of Materials Chemistry, 21 (2011) 19368-19374.

[65] R. von Hagen, H. Lorrmann, K.C. Moller, S. Mathur, Advanced Energy Materials, 2 (2012) 553-559.

[66] M. Zhao, G. Huang, B. Zhang, F. Wang, X. Song, Journal of Power Sources, 211 (2012) 202-207.

[67] K.-W. Nam, W.-S. Yoon, K. Zaghib, K. Yoon Chung, X.-Q. Yang, Electrochemistry Communications, 11 (2009) 2023-2026.

[68] J.R. Ying, M. Lei, C.Y. Jiang, C.R. Wan, X.M. He, J.J. Li, L. Wang, J.G. Ren, Journal of Power Sources, 158 (2006) 543-549.

[69] C. Delacourt, C. Wurm, L. Laffont, J.B. Leriche, C. Masquelier, Solid State Ionics,

177 (2006) 333-341.

[70] S.Q. Shi, L.J. Liu, C.Y. Ouyang, D.S. Wang, Z.X. Wang, L.Q. Chen, X.J. Huang, Physical Review B, 68 (2003).

[71] N. Meethong, Y.H. Kao, S.A. Speakman, Y.M. Chiang, Advanced Functional Materials, 19 (2009) 1060-1070.

[72] M. Wagemaker, B.L. Ellis, D. Luetzenkirchen-Hecht, F.M. Mulder, L.F. Nazar, Chemistry of Materials, 20 (2008) 6313-6315.

[73] C.A.J. Fisher, V.M.H. Prieto, M.S. Islam, Chemistry of Materials, 20 (2008) 5907-5915.

[74] S.Y. Chung, S.Y. Choi, T. Yamamoto, Y. Ikuhara, Angewandte Chemie-International Edition, 48 (2009) 543-546.

[75] R. Amin, P. Balaya, J. Maier, Electrochemical and Solid State Letters, 10 (2007) A13-A16.

[76] R. Amin, C.T. Lin, J.B. Peng, K. Weichert, T. Acarturk, U. Starke, J. Maier, Advanced Functional Materials, 19 (2009) 1697-1704.

[77] N. Meethong, H.Y.S. Huang, S.A. Speakman, W.C. Carter, Y.M. Chiang, Advanced Functional Materials, 17 (2007) 1115-1123.

[78] Z.-R. Chang, H.-J. Lv, H. Tang, X.-Z. Yuan, H. Wang, Journal of Alloys and

Compounds, 501 (2010) 14-17.

[79] D. Arumugam, G. Paruthimal Kalaignan, P. Manisankar, Journal of Solid State Electrochemistry, 13 (2009) 301-307.

[80] Z. Liu, X. Zhang, L. Hong, Journal of Applied Electrochemistry, 39 (2009) 2433-2438.

[81] H. Liu, Q. Cao, L.J. Fu, C. Li, Y.P. Wu, H.Q. Wu, Electrochemistry Communications, 8 (2006) 1553-1557.

[82] H. Huang, S.C. Yin, L.F. Nazar, Electrochemical and Solid State Letters, 4 (2001) A170-A172.

[83] R. Dominko, M. Bele, M. Gaberscek, M. Remskar, D. Hanzel, S. Pejovnik, J. Jamnik, Journal of the Electrochemical Society, 152 (2005) A607-A610.

[84] Y.G. Wang, Y.R. Wang, E.J. Hosono, K.X. Wang, H.S. Zhou, Angewandte Chemie-International Edition, 47 (2008) 7461-7465.

[85] X.L. Wu, L.Y. Jiang, F.F. Cao, Y.G. Guo, L.J. Wan, Advanced Materials, 21 (2009) 2710.

[86] Y. Zhou, J. Wang, Y. Hu, R. O'Hayre, Z. Shao, Chemical Communications, 46 (2010) 7151-7153.

[87] Z.L. Liu, S.W. Tay, L.A. Hong, J.Y. Lee, Journal of Solid State Electrochemistry, 15

(2011) 205-209.

[88] C.H. Mi, Y. Cao, X.G. Zhang, X.B. Zhao, H.L. Li, Powder Technology, 181 (2008) 301-306.

[89] K.S. Park, J.T. Son, H.T. Chung, S.J. Kim, C.H. Lee, K.T. Kang, H.G. Kim, Solid State Communications, 129 (2004) 311-314.

[90] R. Trócoli, J. Morales, S. Franger, J. Santos-Peña, Electrochimica Acta, 61 (2012) 57-63.

[91] Y.H. Huang, K.S. Park, J.B. Goodenough, Journal of the Electrochemical Society, 153 (2006) A2282-A2286.

[92] Y.H. Huang, J.B. Goodenough, Chemistry of Materials, 20 (2008) 7237-7241.

[93] J. Yang, J. Wang, D. Wang, X. Li, D. Geng, G. Liang, M. Gauthier, R. Li, X. Sun, Journal of Power Sources, 208 (2012) 340-344.

[94] Y. Tang, F. Huang, H. Bi, Z. Liu, D. Wan, Journal of Power Sources, 203 (2012) 130-134.

[95] K.S. Park, S.B. Schougaard, J.B. Goodenough, Advanced Materials, 19 (2007) 848.

[96] D. Jugovic, D. Uskokovic, Journal of Power Sources, 190 (2009) 538-544.

[97] Y.H. Rho, L.F. Nazar, L. Perry, D. Ryan, Journal of the Electrochemical Society, 154 (2007) A283-A289.

[98] A.A. Salah, A. Mauger, C.M. Julien, F. Gendron, Materials Science and Engineering B-Solid State Materials for Advanced Technology, 129 (2006) 232-244.

[99] S.S. Zhang, J.L. Allen, K. Xu, T.R. Jow, Journal of Power Sources, 147 (2005) 234-240.

[100] H.P. Liu, Z.X. Wang, X.H. Li, H.J. Guo, W.J. Peng, Y.H. Zhang, Q.Y. Hu, Proc. Meeting of the International-Battery-Material-Association, Shenzhen, PEOPLES R CHINA, Nov 16-20, 2007.

[101] L. Wang, G.C. Liang, X.Q. Ou, X.K. Zhi, J.P. Zhang, J.Y. Cui, Proc. 14th International Meeting on Lithium Batteries, Tianjin, PEOPLES R CHINA, Jun 22-28, 2008.

[102] C.W. Kim, M.H. Lee, W.T. Jeong, K.S. Lee, Proc. 12th International Meeting on Lithium Batteries, Nara, JAPAN, Jun 27-Jul 02, 2004.

[103] C.W. Kim, J.S. Park, K.S. Lee, Proc. 2nd International Conference on Polymet Batteries and Fuel Cells, Las Vegas, NV, Jun 12-17, 2005.

[104] S.J. Kwon, C.W. Kim, W.T. Jeong, K.S. Lee, Journal of Power Sources, 137 (2004) 93-99.

[105] S.A. Needham, A. Calka, G.X. Wang, A. Mosbah, H.K. Liu, Electrochemistry Communications, 8 (2006) 434-438.

[106] J.S. Yang, J.J. Xu, Electrochemical and Solid State Letters, 7 (2004) A515-A518.

[107] Y.Q. Hu, M.M. Doeff, R. Kostecki, R. Finones, Journal of the Electrochemical Society, 151 (2004) A1279-A1285.

[108] R. Dominko, M. Bele, J.M. Goupil, M. Gaberscek, D. Hanzel, I. Arcon, J. Jamnik, Chemistry of Materials, 19 (2007) 2960-2969.

[109] B. Ellis, W.H. Kan, W.R.M. Makahnouk, L.F. Nazar, Journal of Materials Chemistry, 17 (2007) 3248-3254.

[110] C.A.J. Fisher, M.S. Islam, Journal of Materials Chemistry, 18 (2008) 1209-1215.

[111] S.F. Yang, P.Y. Zavalij, M.S. Whittingham, Electrochemistry Communications, 3 (2001) 505-508.

[112] S.F. Yang, Y.N. Song, P.Y. Zavalij, M.S. Whittingham, Proc. Joint Meeting of the International-Society-for-Electrochemistry/Electrochemical-Society, San Franciscco, California, Sep 04, 2001.

[113] J.J. Chen, M.S. Whittingham, Electrochemistry Communications, 8 (2006) 855-858.

[114] K.S. Park, J.T. Son, H.T. Chung, S.J. Kim, C.H. Lee, H.G. Kim, Electrochemistry Communications, 5 (2003) 839-842.

[115] G. Arnold, J. Garche, R. Hemmer, S. Strobele, C. Vogler, A. Wohlfahrt-Mehrens,

Proc. 11th International Meeting on Lithium Batteries, Monterey, California, Jun 24-28, 2002.

[116] Z.H. Li, D.M. Zhang, F.X. Yang, Journal of Materials Science, 44 (2009) 2435-2443.

[117] S.T. Myung, S. Komaba, N. Hirosaki, H. Yashiro, N. Kumagai, Electrochimica Acta, 49 (2004) 4213-4222.

[118] J.M. Tarascon, N. Recham, M. Armand, J.N. Chotard, P. Barpanda, W. Walker, L. Dupont, Chemistry of Materials, 22 (2010) 724-739.

[119] N. Recham, J.N. Chotard, L. Dupont, C. Delacourt, W. Walker, M. Armand, J.M. Tarascon, Nature Materials, 9 (2010) 68-74.

[120] P. Barpanda, N. Recham, J.N. Chotard, K. Djellab, W. Walker, M. Armand, J.M. Tarascon, Journal of Materials Chemistry, 20 (2010) 1659-1668.

[121] J. Barker, M.Y. Saidi, J.L. Swoyer, Journal of the Electrochemical Society, 150 (2003) A1394-A1398.

[122] R.K.B. Gover, P. Burns, A. Bryan, M.Y. Saidi, J.L. Swoyer, J. Barker, Solid State Ionics, 177 (2006) 2635-2638.

[123] F. Zhou, X. Zhao, J.R. Dahn, Electrochemistry Communications, 11 (2009) 589-591.

[124] M.V. Reddy, G.V. Subba Rao, B.V.R. Chowdari, Journal of Power Sources, 195 (2010) 5768-5774.

[125] J. Barker, R.K.B. Gover, P. Burns, A. Bryan, M.Y. Saidi, J.L. Swoyer, Journal of the Electrochemical Society, 152 (2005) A1776-A1779.

[126] J. Barker, M.Y. Saidi, J.L. Swoyer, Journal of the Electrochemical Society, 151 (2004) A1670-A1677.

[127] Y.Z. Li, Z. Zhou, X.P. Gao, J. Yan, Journal of Power Sources, 160 (2006) 633-637.

[128] M.C. Smart, B.V. Ratnakumar, Journal of the Electrochemical Society, 158 (2011) A379-A389.

[129] W. Wang, M.K. Datta, P.N. Kumta, Journal of Materials Chemistry, 17 (2007) 3229-3237.

[130] T. Ohzuku, T. Kodama, T. Hirai, Journal of Power Sources, 14 (1985) 153-166.

[131] A.C. Ferrari, Solid State Communications, 143 (2007) 47-57.

[132] A.C. Ferrari, J. Robertson, Physical Review B, 61 (2000) 14095-14107.

[133] A.C. Ferrari, J. Robertson, Physical Review B, 64 (2001) 075414.

[134] G. Ting-Kuo Fey, T.-L. Lu, F.-Y. Wu, W.-H. Li, Journal of Solid State Electrochemistry, 12 (2008) 825-833.

[135] D. Li, Y. Huang, N. Sharma, Z. Chen, D. Jia, Z. Guo, Physical Chemistry Chemical Physics, 14 (2012) 3634-3639.

[136] D.G. Zhuang, X.B. Zhao, J. Xie, J. Tu, T.J. Zhu, G.S. Cao, Acta Physico-Chimica Sinica, 22 (2006) 840-844.

[137] G.X. Wang, S. Bewlay, S.A. Needham, H.K. Liu, R.S. Liu, V.A. Drozd, J.F. Lee, J.M. Chen, Journal of the Electrochemical Society, 153 (2006) A25-A31.

[138] H. Schafer, G. Schneidereit, W. Gerhardt, ZEITSCHRIFT FUR ANORGANISCHE UND ALLGEMEINE CHEMIE, 319 (1963) 372.

[139] J. Riga, C. Tenret-Noël, J.J. Pireaux, R. Caudano, J.J. Verbist, Y. Gobillon, Physica Scripta, 16 (1977) 351.

[140] H. Wang, H. Xia, M.O. Lai, L. Lu, Electrochemistry Communications, 11 (2009) 1539-1542.

[141] N. Nicoloso, A. LeCorre-Frisch, J. Maier, R.J. Brook, Solid State Ionics, 75 (1995) 211-216.

[142] J.W. Long, K.E. Swider, C.I. Merzbacher, D.R. Rolison, Langmuir, 15 (1999) 780-785.

[143] R. Pflieger, M. Malki, Y. Guari, J. Larionova, A. Grandjean, Journal of the American Ceramic Society, 92 (2009) 1560-1566.

[144] Y.S. Hu, Y.G. Guo, R. Dominko, M. Gaberscek, J. Jamnik, J. Maier, Advanced Materials, 19 (2007) 1963.

[145] C.-C. Hu, K.-H. Chang, M.-C. Lin, Y.-T. Wu, Nano Letters, 6 (2006) 2690-2695.

[146] R. Shannon, Acta Crystallographica Section A: Crystal Physics, Diffraction, Theoretical and General Crystallography, 32 (1976) 751-767.

[147] M.S. Islam, D.J. Driscoll, C.A.J. Fisher, P.R. Slater, Chemistry of Materials, 17 (2005) 5085-5092.

[148] F. Yu, J.-J. Zhang, Y.-F. Yang, G.-Z. Song, Journal of Materials Chemistry, 19 (2009) 9121-9125.

[149] R. Dedryvère, M. Maccario, L. Croguennec, F. Le Cras, C. Delmas, D. Gonbeau, Chemistry of Materials, 20 (2008) 7164-7170.

[150] S.M. Oh, S.W. Oh, C.S. Yoon, B. Scrosati, K. Amine, Y.K. Sun, Advanced Functional Materials, 20 (2010) 3260-3265.

[151] J.C. Arrebola, A. Caballero, M. Cruz, L. Hernán, J. Morales, E.R. Castellón, Advanced Functional Materials, 16 (2006) 1904-1912.

[152] K. Zaghib, M. Trudeau, A. Guerfi, J. Trottier, A. Mauger, R. Veillette, C.M. Julien, Journal of Power Sources, 204 (2012) 177-181.

[153] X. Lou, Y. Zhang, Journal of Materials Chemistry, 21 (2011) 4156-4160.

[154] R. Baddour-Hadjean, J.-P. Pereira-Ramos, Chemical Reviews, 110 (2009) 1278-1319.

[155] R.B.V.D. A.C. Larson, Los Alamos National Laboratory Report LAUR, (1994) 86-748.

[156] B.H. Toby, Journal of Applied Crystallography, 34 (2001) 210-213.

[157] T.N. Ramesh, K.T. Lee, B.L. Ellis, L.F. Nazar, Electrochemical and Solid-State Letters, 13 (2010) A43-A47.

[158] J. Barker, R.K.B. Gover, P. Burns, A. Bryan, M.Y. Saidi, J.L. Swoyer, Journal of Power Sources, 146 (2005) 516-520.

[159] M.H. Hebb, J. Chem. Phys., 20 (1952) 185.

[160] W. Weppner, R.A. Huggins, Journal of the Electrochemical Society, 124 (1977) 1569-1578.

[161] C. Ho, I.D. Raistrick, R.A. Huggins, Journal of the Electrochemical Society, 127 (1980) 343-350.

[162] A.J. Bard, L.R. Faulkner, Electrochemical Methods: Fundamentals and Applications, in, Wiley, 2000.

[163] Y. Zhu, C. Wang, Journal of Physical Chemistry C, 114 (2010) 2830-2841.

[164] M.D. Levi, D. Aurbach, Journal of Solid State Electrochemistry, 11 (2007)

1031-1042.

[165] K.F. Hsu, S.Y. Tsay, B.J. Hwang, Journal of Materials Chemistry, 14 (2004) 2690-2695.

[166] X.J. Zhu, Y.X. Liu, L.M. Geng, L.B. Chen, Journal of Power Sources, 184 (2008) 578-582.

[167] A.N. Serafini, S.J. Houston, I. Resche, D.P. Quick, F.M. Grund, P.J. Ell, A. Bertrand, F.R. Ahmann, E. Orihuela, R.H. Reid, R.A. Lerski, B.D. Collier, J.H. McKillop, G.L. Purnell, A.P. Pecking, F.D. Thomas, K.A. Harrison, Journal of Clinical Oncology, 16 (1998) 1574-1581.

[168] E.M. Bauer, C. Bellitto, G. Righini, M. Pasquali, A. Dell'Era, P.P. Prosini, Journal of Power Sources, 146 (2005) 544-549.

[169] B. Wang, Y. Qiu, L. Yang, Electrochemistry Communications, 8 (2006) 1801-1805.

[170] M.R. Hill, G.J. Wilson, L. Bourgeois, A.G. Pandolfo, Energy & Environmental Science, 4 (2011) 965-972.

[171] F.K. Kalman, R. Kiraly, E. Brucher, European Journal of Inorganic Chemistry, (2008) 4719-4727.

[172] N. Bernd, Water Research, 37 (2003) 2533-2546.

[173] D. Deng, M.G. Kim, J.Y. Lee, J. Cho, Energy & Environmental Science, 2 (2009) 818-837.

[174] Z.G. Yang, D. Choi, S. Kerisit, K.M. Rosso, D.H. Wang, J. Zhang, G. Graff, J. Liu, Journal of Power Sources, 192 (2009) 588-598.

[175] J.W. Xu, C.H. Ha, B. Cao, W.F. Zhang, Electrochimica Acta, 52 (2007) 8044-8047.

[176] J. Li, Z. Tang, Z. Zhang, Electrochemical and Solid-State Letters, 8 (2005) A316-A319.

[177] J. Kim, J. Cho, Journal of the Electrochemical Society, 154 (2007) A542-A546.

[178] Y.S. Hu, L. Kienle, Y.G. Guo, J. Maier, Advanced Materials, 18 (2006) 1421.

[179] M. Takagi, Y. Murota, M. Tajima, T. Asao, M. Saito, A. Tasaka, M. Inaba, ECS Transacations, 33 (2011) 57-66.

[180] M. Salari, M. Renee, S.P.H. Marashi, S.H. Aboutalebi, Powder Technology, 192 (2009) 54-57.

[181] P. Billik, G. Plesch, Scripta Materialia, 56 (2007) 979-982.

[182] J. Lu, Z.Z. Fang, Journal of the American Ceramic Society, 89 (2006) 842-847.

[183] C. Suryanarayana, Progress in Materials Science, 46 (2001) 1-184.

[184] S.L. James, C.J. Adams, C. Bolm, D. Braga, P. Collier, T. Friscic, F. Grepioni, K.D.M. Harris, G. Hyett, W. Jones, A. Krebs, J. Mack, L. Maini, A.G. Orpen, I.P. Parkin, W.C. Shearouse, J.W. Steed, D.C. Waddell, Chemical Society Reviews, 41 (2012) 413-447.

[185] C.-M. Park, W.-S. Chang, H. Jung, J.-H. Kim, H.-J. Sohn, Electrochemistry Communications, 11 (2009) 2165-2168.

[186] G.J. Wilson, A.S. Matijasevich, D.R.G. Mitchell, J.C. Schulz, G.D. Will, Langmuir, 22 (2006) 2016-2027.

[187] C.J. Doss, R. Zallen, Physical Review B, 48 (1993) 15626-15637.

[188] R. Sanjines, H. Tang, H. Berger, F. Gozzo, G. Margaritondo, F. Levy, Journal of Applied Physics, 75 (1994) 2945-2951.

[189] A. Ghicov, H. Tsuchiya, J.M. Macak, P. Schmuki, physica status solidi (a), 203 (2006) R28-R30.

[190] M. Wagemaker, W.J.H. Borghols, F.M. Mulder, Journal of the American Chemical Society, 129 (2007) 4323-4327.

[191] H.-E. Wang, H. Cheng, C. Liu, X. Chen, Q. Jiang, Z. Lu, Y.Y. Li, C.Y. Chung, W. Zhang, J.A. Zapien, L. Martinu, I. Bello, Journal of Power Sources, 196 (2011) 6394-6399.

[192] S.K. Das, S. Darmakolla, A.J. Bhattacharyya, Journal of Materials Chemistry, 20 (2010) 1600-1606.

[193] G. Sudant, E. Baudrin, D. Larcher, J.-M. Tarascon, Journal of Materials Chemistry, 15 (2005) 1263-1269.

[194] M.V. Reddy, R. Jose, T.H. Teng, B.V.R. Chowdari, S. Ramakrishna, Electrochimica Acta, 55 (2010) 3109-3117.

Patents and Journal Papers

L. Lu, P.F. Xiao, MO Lai, J.F. Ni, US Patent, $LiMPO_4$-based compositions of matter for cathodes for high-performance Li batteries, PCT/SG2011/000010, 2011

L. Lu, M.O. Lai, P.F. Xiao, US Patent, Nano-Structured Phosphates with Secondary Architectures Synthesized via Sol-gel Method, US Provisional Patent Application No. 61/614,650, 2012

L. Lu, M.O. Lai, P.F. Xiao, US Patent, A Method for Synthesis of Phosphate-Based Materials, US Provisional Patent Application No. 61/714,285, 2012

P.F. Xiao, M.O. Lai, L. Lu, Electrochemical Properties of nanocrysatlline TiO_2 synthesized via mechanochemical milling, Electrochimica Acta, 2012

P.F. Xiao, B. Ding, M.O. Lai, L Lu, High rate performance $LiMn_{1-x}Fe_xPO_4$ synthesized via facile polymer-assisted mechanical activation, submitted

P.F. Xiao, M.O. Lai, L Lu, PF Xiao, MO Lai, L Lu, Transport and electrochemical study of tavorite $LiVPO_4F$, submitted

P.F. Xiao, M.O. Lai, L. Lu, Hollow microspherical $LiFePO_4$/C synthesized from a novel multidentate phosphonate complexing agent, submmited